Physics – Uspekhi **50** (5) 455 – 488 (2007) © 2007 Uspekhi Fizicheskikh Nauk, Russian Academy of Sciences

REVIEWS OF TOPICAL PROBLEMS PACS numbers: **36.40. – c**, 52.80. Sm, 61.46.Bc

Magnetron plasma and nanotechnology

P V Kashtanov, B M Smirnov, R Hippler

DOI: 10.1070/PU2007v050n05ABEH006138

Contents

1. **Introduction** 455
2. **Study of magnetron discharge** 456
   2.1 Principles of magnetron discharge; 2.2 Scheme of magnetron discharge; 2.3 Experimental aspects of a magnetron discharge
3. **Processes in a magnetron plasma involving metal atoms** 466
   3.1 Emission of fast metal atoms by cathode bombardment with ions; 3.2 Nucleation processes in a buffer gas involving metal atoms; 3.3 Processes near a cathode involving fast sputtered atoms; 3.4 Cluster generation in a magnetron plasma; 3.5 Heat processes in a magnetron plasma
4. **Transport of clusters in a gas flow** 476
   4.1 Flow of a buffer gas through the magnetron chamber; 4.2 Equilibrium of a buffer gas flow and cluster drift; 4.3 Attachment of clusters to walls; 4.4 Charging and evolution of charged clusters in a secondary plasma; 4.5 Passing a gas flow with clusters through an orifice
5. **Cluster deposition and cluster structures** 482
   5.1 Cluster beams for the fabrication of films and materials; 5.2 Cluster deposition on surfaces; 5.3 Magnetron covering of dust particles with film
6. **Conclusions** 486
   References 486

Abstract. **Magnetron plasma processes involving metal atoms and clusters are reviewed. The formation of metal atoms near the cathode and their nucleation in a buffer gas flow are discussed. The flow of a buffer gas with metal clusters through a magnetron chamber disturbs the equilibrium between the buffer gas flow and clusters near the exit orifice and is accompanied by cluster attachment to the chamber walls. Cluster charging far off the cathode, the disturbance of equilibrium between the buffer gas flow and cluster drift, and the attachment of charged clusters to the chamber walls — the factors determining the output parameters of the cluster beam escaping the magnetron chamber — are analyzed. Cluster deposition on a solid surface and on dusty plasma particles is considered.**

1. Introduction

A concept of the magnetron discharge (MD) was suggested by F M Penning seventy years ago [1]. Subsequently, this scheme was modified [2 – 5], improving the use of magnetron discharge for applications. The specifics of a magnetron discharge are such that electrons are magnetized and therefore they are locked in a cathode region, while the Larmor radius for ions is large compared to the dimensions of the cathode region; therefore, electrons do not participate in the maintenance of this gas discharge near the cathode, and the discharge current is supported by the emission of electrons from the cathode surface under the action of ion bombardment. This requires a high energy of ions for cathode bombardment, amounting to a few hundred of electron-volts near the cathode. As a result of the cathode bombardment, fast metal atoms are formed along with the secondary electrons. Hence, due to effective cathode erosion, magnetron discharge finds various applications [7 – 12] where sputtered atoms are used for the preparation of films, coverings of microelectronics elements, and manufacturing new materials [13 – 18]. The effective generation of fast metal atoms is stimulating interest in magnetron discharge and leading to its study.

According to its regime, magnetron discharge can be compared with glow discharge [19, 20]. In both cases, discharge is supported by ion collisions with the cathode, and the cathode drop in glow discharge is comparable to the voltage of magnetron discharge, which is a few hundred volts. But the buffer gas pressure in glow discharge is higher than that in magnetron discharge, and this provides an ion kinetic energy near the cathode in magnetron discharge approximately one order of magnitude higher than that in glow discharge. This leads to a decrease in the secondary electron yield in the glow discharge that is compensated by ionization processes in the cathode region of the glow discharge with the participation of electrons and buffer gas atoms. In magnetron

P V Kashtanov, B M Smirnov Institute for High Temperatures, Russian Academy of Sciences,
ul. Izhorskaya 13/19, 127412 Moscow, Russian Federation
Tel./Fax (7-499) 190 42 44
E-mail: kashtan@maryno.net
R Hippler Institute of Physics, University of Greifswald,
17487 Greifswald, Germany
E-mail: hippler@physik.uni-greifswald.de

Received 8 June 2006, revised 13 November 2006
Uspekhi Fizicheskikh Nauk **177** (5) 473 – 510 (2007)
Translated by B M Smirnov; edited by A Radzig

discharge, electrons are locked in the magnetic field region and do not partake in ionization processes near the cathode. Because of the need to maintain the balance between the electrons being produced and ions which leave the discharge, the probability of sputtering the secondary electron (taking into account subsequent ionization) is close to one.

Thus, an ion is subjected to collisions in the cathode region of glow discharge, its energy decreases resulting in a decline in probability of the secondary electron generation. This scattering is compensated for by ionization processes with the participation of the buffer gas electrons and atoms, and a discharge glowing is sustained through their proceeding.. In magnetron discharge, the trapped electrons are of minor importance in sustaining the discharge because the total probability of secondary electron generation in the processes of ion scattering from the cathode is close to unity. Evidently, interaction between fast ions and the cathode leads not only to the generation of secondary electrons, but also to the emission of fast metal atoms from the cathode, which is of importance for the processes under consideration.

In a simple scheme of applying magnetron discharge, a target is placed near the cathode and is then covered by cathode atoms, so that sputtered atoms come directly towards the target with a partial scattering on buffer gas atoms. Such a scheme is the most widespread for magnetron discharge, when cathode atoms are used for covering a target with metal atoms. Below, we consider a more complex version of magnetron discharge, where sputtered metal atoms are transformed into clusters near the cathode [27 – 29]. These nucleation processes proceed in a buffer gas flow, and this regime of magnetron discharge is accompanied by various processes involving ions, electrons, atoms, and clusters. The analysis of these processes and possible applications of the clusters being formed to fabricating nanostructures and nanomaterials is the goal of this review.

2. Study of magnetron discharge

2.1 Principles of magnetron discharge

A general concept of standard magnetron discharge is given in Fig. 1 [6]. Two cylindrical permanent magnets create a magnetic field above the cathode with the maximum of the magnetic field strength between the magnets. Electrons are trapped by the magnetic field and are located in a region of maximum magnetic field strength, i.e., the Larmor radius of the electrons is small. This field does not act on ions. Ions bombard the cathode and produce secondary electrons which ionize buffer gas atoms. Then, if an electric field is created perpendicular to the cathode, electrons will drift in the direction perpendicular to these fields. Indeed, the Newton equation for the electron velocity $\mathbf{v_e}$ has the from

$$m_e \frac{d\mathbf{v_e}}{dt} = e\mathbf{E} + \frac{e}{c}[\mathbf{v_e H}], \qquad (2.1)$$

where m_e is the electron mass, and $\mathbf{E}$ and $\mathbf{H}$ are the electric and magnetic field strengths, respectively. From this it follows that in the stationary regime an electron drifts in the direction that is perpendicular to the electric and magnetic fields, i.e., it is found in a torus depicted in Fig. 2a [6]. If we ignore the interaction of a probe electron with surrounding electrons and ions, the electron drift velocity in this cross section is given by

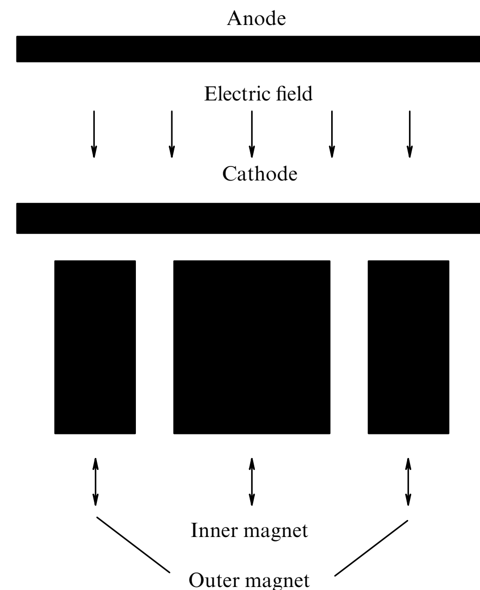

Figure 1. A general scheme of magnetron discharge.

$$v_e = c\frac{E}{H}. \qquad (2.2)$$

Of course, this conclusion is valid not only for the stationary case but for any case when electron circulation time inside the torus is less than the typical time of field variation. Note that the magnetic field strength decreases upon removal from the cathode, and a region of a strong magnetic field occupies a small discharge part near the cathode (Fig. 2b) [21]. We give below a simplified description of magnetron discharge that allows us to understand its nature.

One can extract three basic regions of magnetic discharge, namely, the region of ion acceleration, the region of a heightened magnetic field near the cathode with a high electron number density, where captured electrons are located, and the region between the 'trap' zone and walls, where slow ions are formed as a result of atomic ionization by electron impact. Note that the energy consumed for the production of one electron – ion pair as a result of buffer gas atom ionization by electron impact exceeds by several times the atomic ionization potential. Therefore, the voltage in the third region with reproduction of ions is a few dozen volts and is lower by one order of magnitude than the voltage in the cathode region where secondary electrons are produced. Thus, the largest part of the voltage drop relates to the cathode region. A simple empirical formula that connects the total discharge voltage U and the voltage of the cathode region that is equal to the final kinetic energy of ions E_i is written as [22]

$$E_i = 0.73\, U.$$

In addition, one can expand the region of ion formation by electron impact, and the number of ions being formed per secondary electron exceeds one significantly. A region that resembles the positive column occurs ahead of the anode region, and the numbers of electrons and ions formed in ionization processes and attaching to walls are equal in this region. In this way, a heightened discharge voltage (compared to glow discharge) provides self-sustained discharge.

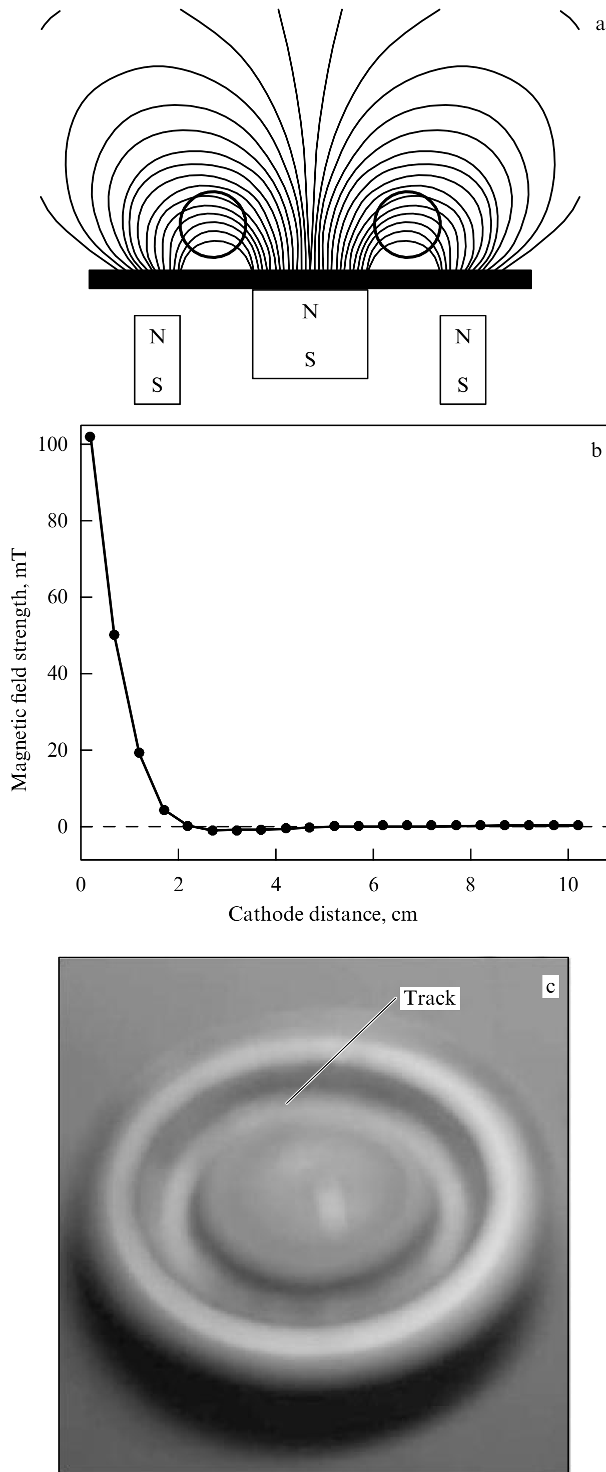

Figure 2. (a) Magnetic lines of force in magnetron discharge [6]. The region is marked where electrons are trapped by the field in the magnetron discharge and move along rings. (b) The distribution of the magnetic field strength upon removing the maximum magnetic field from the region in the direction perpendicular to the cathode [21]. (c) Character of cathode erosion in magnetron discharge [6].

The cathode region of magnetron discharge represents a gap between the capture region and cathode, and its width is small compared to the ion mean free path. Ions are accelerated in this region and bombard the cathode. Note that switching off the magnetic field would lead to a decrease in the discharge voltage, in accord with the character of

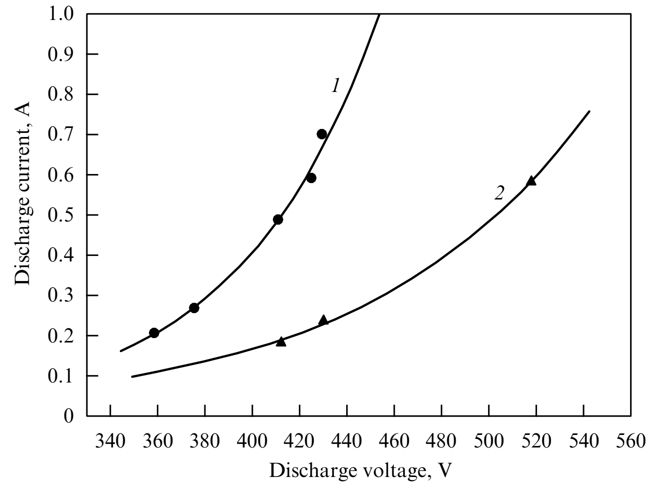

Figure 3. The current – voltage characteristic of magnetron discharge with argon as a buffer gas at a pressure of 5 mTorr for Al (*1*) and Cu (*2*) cathodes [127].

processes in this region. Assuming all the gap potential to be used for enhancing the impact ion energy, the gap thickness is small compared to the mean free path of ions in a buffer gas. In addition, the voltage of the noncompensated ion charge in this region is less than the cathode voltage.

Let us analyze the gap parameters from the standpoint of a noncompensated positive charge due to ions, which creates an additional voltage in the gap, and this potential increases the total discharge voltage. We use the Child – Langmuir law or three-halves-power law [23, 24] that connects the saturation current density i, the gap voltage U, and the gap thickness l, having the form

$$i = \frac{2}{9\pi}\sqrt{\frac{e}{2m_{\mathrm{i}}}}\,\frac{U^{3/2}}{l^2}\,, \tag{2.3}$$

where m_{i} is the ion mass. For typical values of the current density $i \sim 10$ mA cm^{-2} and the voltage $U \sim 300$ V we obtain the critical gap size $l \sim 0.2$ mm in the case of argon. Taking the gap dimension to be less than this value, the gap voltage is independent of the discharge current density. Note that such conditions correspond to high electric field strengths in a gap in the range of $E = 10^4 - 10^5$ V cm^{-1}.

Thus, based on the first approximation to the above simple scheme for the cathode region of magnetron discharge, where ions are accelerated, we obtain the important result that the cathode region is narrow. Then the discharge voltage is determined mostly by the voltage of the cathode gap and its value follows from the condition of reproduction of electrons. Ignoring the influence of the space charge in this region, we obtain a discharge voltage U independent of the discharge current I. In reality, this corresponds to a sharp dependence of the discharge electric current I on the discharge voltage U that is usually approximated as [26]

$$I = kU^n\,,$$

and generally $n > 5$. As a demonstration of this fact, Fig. 3 depicts the current – voltage characteristics for magnetron discharge in argon with Al and Cu cathodes.

Most of the discharge voltage relates to a gap near the cathode where ions are accelerated and bombard the cathode.

The dimension of this region is determined by an ion charge due to the ion current and does not exceed that following from formula (2.3). In addition, this dimension is small compared to the mean free path of ions in a buffer gas. This fact requires a low pressure of buffer gas. In the next discharge region of a high magnetic field strength, electrons are trapped by the magnetic field, and due to the high space charge of these electrons the thermal ions are drawn into this region and compensate the electron charge. As a result, this region is characterized by a large concentration of charged particles and, hence, by a high plasma conductivity.

This discharge region is a source of ions which bombard the cathode. The character of penetration of the discharge current through a region of captured electrons, which is a torus in shape, influences the profile of cathode erosion in magnetron discharge (Fig. 2c). The depth of the potential well formed by a field that is parallel to the cathode surface is given by the formula $\Delta U = \mu H$, where the magnetic moment μ of captured electrons is equal to

$$\mu = \frac{JS}{c} .$$

Here, $J = ev_e/2\pi r$ is the electric current for an individual electron, and v_e is its drift velocity according to formula (2.2), r is the torus radius in accordance with the geometry of the magnetic field, and $S = \pi r^2$ is the area of the circle enclosed by the electron trajectory. As a result, we have on the basis of formula (2.2) that

$$\Delta U = \mu H = \frac{eEr}{2} . \tag{2.4}$$

From this it follows that the depth of the potential well for a captured electron is independent of the magnetic field strength and is determined by the electric field strength. On average, the electric field strength for this discharge with the exclusion of a small region near the cathode amounts to ~ 10 V cm^{-1}. The electric field strength in the region of captured electrons is less than this value due to the high conductivity of this region. Under real conditions, in the region of captured electrons $E > 0.1$ V cm^{-1}, the potential well depth is significantly larger than the thermal electron energy, and therefore electrons are captured in this region.

The electron drift velocity in crossed electric and magnetic fields is, according to formula (2.2), given by

$$v_e = \frac{E}{H} = \frac{eE}{m_e \omega_H} . \tag{2.5}$$

Under typical conditions ($H \sim 100$ G, the Larmor frequency $\omega_H \sim 2 \times 10^9$ Hz, $E \sim 0.1$ V cm^{-1}), we have $v_e \sim 10^5$ cm s^{-1} — that is, the electron drift velocity is small compared to the thermal electron velocity equal to $\sim 10^7$ cm s^{-1}. Thus, the Larmor radius for captured electrons is less than the trajectory radius by one to three orders of magnitude. Hence, the motion of captured electrons along the circular trajectories inside the potential well with reflection from the walls has a random character.

2.2 Scheme of magnetron discharge

Magnetron discharge is used widely for covering a target with a metal that is sputtered from the cathode. In the simplest scheme, a target is placed not far from the cathode, and sputtering atoms attach to the target, forming a thin film on its surface. As the vapor and gas pressure in the magnetron discharge increase, new processes occur and the lifetime of the magnetron plasma increases. The long lifetime of the atoms leads to their joining in clusters, and a sputtered cathode material is now used in the form of clusters rather than individual atoms. We will consider below such a scheme developed by Haberland et al. [27–34], where sputtering atoms are converted into clusters. The possibility of running nucleation processes requires a high number density of metal atoms in the nucleation region and temperatures that are not very high, which allows atoms to form chemical bonds. Experience shows that these conditions may be fulfilled in reality, and Fig. 4 gives a typical scheme of the magnetron chamber [35] where this takes place. We now consider the general peculiarities of this scheme.

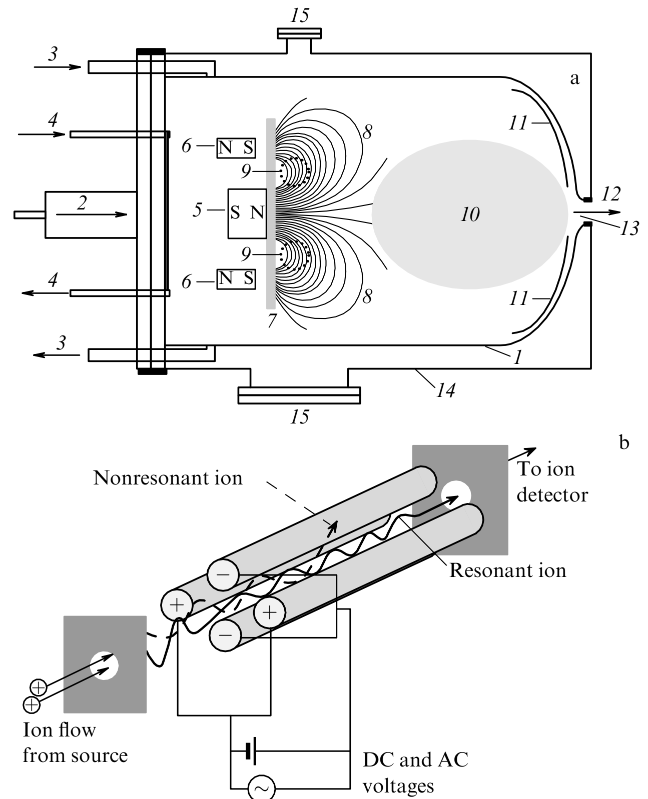

Figure 4. (a) Scheme of a magnetron (aggregation) chamber: *1* — magnetron (aggregation) chamber, *2* — flow of a buffer gas, *3* — liquid nitrogen for cooling the chamber, *4* — water for magnetron cooling, *5* — internal cylindrical magnet, *6* — external ring magnet, *7* — cathode, *8* — magnetic lines of force, *9* — ring of captured electrons (racetrack), *10* — secondary plasma, *11* — electrode for secondary plasma, *12* — flow of buffer gas with clusters, *13* — orifice, *14* — envelope, *15* — pumping. (b) Schematics of the quadrupole mass filter [6, 143].

Nucleation processes require a high number density of metal atoms that is fulfilled at discharge currents that are not small and temperatures that are not high in the nucleation region. Therefore, the cathode and walls are cooled both by water and by liquid nitrogen. Next, in order to provide fast nucleation, it is necessary to increase the buffer gas pressure as much as possible. A typical pressure of the buffer gas in contemporary magnetron chambers is on the order of 10^{-4} atm.

One more peculiarity of this scheme is that a buffer gas flows through the magnetron chamber. The flow velocity is small compared to the speed of sound for a buffer gas and, correspondingly, to a typical thermal velocity of metal or buffer gas atoms. Therefore, pumping does not influence the

propagation of metal atoms through the magnetron chamber, being determined by their diffusion and attachment to clusters. On the contrary, the flow velocity is of importance for clusters because the cluster diffusion coefficient D_n in a buffer gas is relatively small. The flow velocity u determines the dimension of the nucleation region Δx that is estimated as

$$\Delta x \sim \frac{D_n}{u} \, .$$

2.3 Experimental aspects of a magnetron discharge

Principal information about processes in the aggregation regime of magnetron discharge follows from experimental studies. In turn, the experimental research is based on a complex diagnostic technique that is used in contemporary experiments. Because each device used for measuring certain parameters of a magnetron plasma and clusters is of importance for the experiment, we describe separately the experimental equipment for such measurements, along with their concepts and possibilities.

2.3.1 Magnetron chamber. The basis of research under consideration is the magnetron chamber. Since magnetron discharge is burnt at low gas pressure, this pressure is created in the chamber where the working gas is argon or helium that is located inside the liquid nitrogen-cooled aggregation tube, and a variable diaphragm opens the vacuum chamber. An NC200 nanocluster source that was produced by Oxford Applied Research is based on a concept developed by Haberland et al. [27–34]. Magnetron sputtering results from the discharge of a direct current using a metal cathode that is subsequently a material for clusters. Cluster size can be varied by adjusting several parameters, such as power supplied to the magnetron, the aperture size of the variable diaphragm, the rate of rare gas flow, the sort of buffer gas used, the distance between magnets and the variable diaphragm (aggregation tube length), and the temperature inside the aggregation tube. A schematic view of the magnetron chamber is shown in Fig. 4.

As a demonstration of magnetron chamber parameters, we give a description of this equipment that is used at the Institute of Physics of Greifswald University. Three gas inlets using VCR fittings are provided to the magnetron chamber. The middle VCR fitting is for a buffer gas (Ar) which is supplied directly over the target through a ring of holes inside the magnetron cover, the other two gas inlets being used to introduce gases into the aggregation zone. Liquid nitrogen is used for cooling down the aggregation tube, and cold water supply for cooling the magnetron. The target inside the magnetron is backed up by a planar magnet assembly (a system of ring magnets) in a balanced mode, with the inner magnet placed a bit upwards with respect to the outer magnet (see Figs 1, 2a). This arrangement provides a better field line confinement around the target racetrack and thus reduces electron loss and provides a high sputtering yield. But this arrangement has a drawback: the target material gets sputtered mainly in the racetrack region, which causes a significant lose of the target material.

The separation between the magnetron target and the variable orifice can be adjusted using a linear motion-drive mounted on a precision ball-screw mechanism. In this aggregation tube, the formation of clusters from sputtered atoms takes place. Varying the length of this tube changes the residence time of sputtered atoms and clusters and this time influences the typical cluster size. The aggregation tube is cooled by liquid nitrogen at the temperature of nitrogen melting (77.4 K).

The cathode has a disk shape of diameter 5.08 cm with maximum thickness of 5 mm, and is surrounded by a target holder which is the anode. When a sufficient DC voltage is applied, a self-sustained discharge is burnt, and argon ions sputter on the target material. Along with the formation of secondary electrons, cathode processes include emission of secondary ions and neutral atoms, emission of radiation, ion reflection, sputter cascades, and chemical cathode reactions. Ring magnets under the cathode of the magnetron system create the maximum magnetic field between magnets, which is directed parallel to the cathode and is reached near the cathode. Since the discharge electric field is directed perpendicular to the cathode, the crossed electric and magnetic fields cause electron drift along circles which are parallel to the cathode. As a result, a spatial region with a heightened electron number density appears. Slow ions are captured in this region which is characterized by a heightened plasma conductivity. Therefore, the discharge current goes to a greater or lesser extent through this region that creates a specific circular racetrack at the cathode [36, 37]. Just this cathode part is characterized by a heightened erosion, and Fig. 2c exhibits the target racetrack in a conventional balanced mode of magnetron discharge [6].

Having formed inside the aggregation tube, clusters move in a buffer gas flow towards the variable exit diaphragm that serves as the exit to the deposition chamber. Moreover, the diaphragm is responsible for maintaining a respectable pressure gradient between the magnetron chamber and the chamber outside. The aperture size of the diaphragm can be changed externally using a rotary drive. The deposition rate, as well as the pressure inside the aggregation region, can be controlled to a great extent by adjusting the aperture of the diaphragm. The deposition rate is recorded by using a quartz crystal oscillator.

The deposition chamber, where clusters in a beam of a buffer gas are deposited on a substrate, consists of an extracting and focusing units and a substrate holder separated by a shutter. When charged clusters move in a beam, the QMF200 quadrupole mass filter is used to analyze and filter charged clusters. The NC200 nanocluster source can produce both positively and negatively charged clusters. To govern charged clusters, an extracting and focusing unit is installed inside the deposition chamber, allowing one to separate the clusters according to their charges. The extraction and focusing unit includes a set of electric elements which are arranged at regular distances. The extracting element separates the clusters according to its polarity. The two sets of cylinders arranged behind the extracting element help more or less in focusing the beam (termed the focusing elements). Two horizontal deflection plates at the exit of the unit serve as an effective deflector for the cluster beam. In total, the unit acts like an accelerating unit for clusters according to their polarity. By applying the voltage of different polarities to the extracting element (denoted by EV) and focusing element (denoted by FV), when the deflection plates are grounded, one can measure the cluster ion current at the substrate due to the clusters deposited. The current is measured with substrate voltage (SV), both a positive one (collecting negative clusters) and a negative one (collecting positive clusters).

The effective charge separation of the clusters can also be done by applying appropriate deflection voltages. But the

output voltage vanishes more rapidly when a repulsive deflection voltage is applied (i.e., for negative clusters a positive deflection voltage on either the upper or lower deflection plate, while the other is grounded) than when an attractive deflection voltage is used. A metallic shutter between the extraction unit and the substrate holder is used. The substrate (silicon or quartz) is mounted on a metal holder supported by three metal rods which are isolated from the chamber body. The substrate can be supported at a certain voltage by using three supporting rods, which allows one to choose the appropriate conditions for cluster deposition.

2.3.2 Atomic microscopy. When clusters are deposited on a substrate, the atomic microscopy technique allows us to find the size distribution function of deposited solid clusters and the character of the evolution of deposited clusters in the course of growth of the deposited film. The diagnostics of nano-sized particles may be done with a scanning electron microscope with simultaneous energy dispersive X-ray analysis (SEM/EDAX). The transmission electron microscope (TEM) was the first type of electron microscopes and was developed by Max Knoll and Ernst Ruska [38] in Germany in 1932. The first SEM debuted in 1942, with the first commercial instruments appearing around 1965. In particular, such devices are produced now by Netherland Co. FEI. We illustrate in Fig. 5 an example of such a measurement made with the model Quanta 200 FEG for silver cluster deposition on an Si substrate (see also Ref. [39]). This figure shows the character of film growth when solid metal clusters are deposited on a surface. In Fig. 5a clusters are separated particles on the surface, and then (Fig. 5b) some clusters are joined. As a result, a porous film consisting of individual cluster domains is formed.

In addition, atomic force microscopy (AFM) allows us to find the size distribution function for deposited clusters. This technique was invented in 1986 [40] and gives the possibility of analyzing a wide variety of samples, such as conductors, semiconductors, insulators, hard materials (oxides, metals), and soft materials (biological molecules, polymers, clusters, nanoparticles) with a wide range of resolution (100 μm – 1 Å) [41 – 48]. Three methods of AFM diagnostics are available: a contact mode, when the probe has direct physical contact with the sample, a noncontact mode, when the tip is oscillating at a constant height above the sample surface, and a tapping mode, when the oscillating tip touches the sample with a low force.

In an atomic-force microscope (AFM), the superthin needle is held in a cantilever placed above the surface under

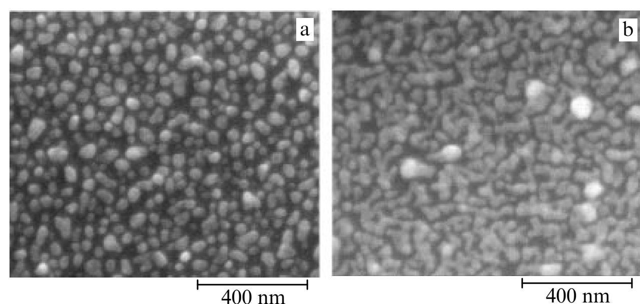

Figure 5. The scanning electron microscope and energy dispersive X-ray analysis (SEM/EDAX) for a film formed from silver clusters deposited on an Si substrate [35].

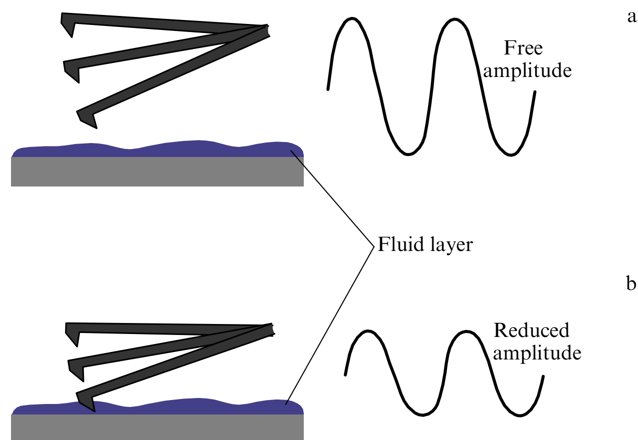

Figure 6. Methods using atomic force microscopy (AFM): (a) a noncontact mode with a probe tip located at a constant height above the sample surface; (b) a tapping mode, when an oscillating tip touches the sample with a low force [6].

study (see Fig. 6). The force interaction comes about between the noncharged needle and the surface, so that the main contribution to it is made by the repulsion forces caused by a mechanical contact of the cantilever tip and the sample, the van der Waals forces, as well as capillary forces due to the presence of an adsorption (water) film at the sample's surface. Upon scanning the surface, the balance of interaction forces between the probe and the sample results in elastic cantilever bending whose magnitude is usually measured by a fiber-optic Fabry – Perot interferometer. The elastic cantilever with a needle is subjected to bends retracing a surface relief for the sample. Tip displacements are monitored through variations of the spacing between interferometer reflectors — that is, the cantilever surface and the interferometer sensor end.

The last two methods are illustrated in Fig. 6. A piezoelectric tripod scanner is used to provide sub-angström motion measurements with one stationary pivot point and three discrete piezoelectric mounted orthogonal for individual X, Y, Z control that provides a large scanning area. X and Y piezo scan across the sample surface, while vertical motion is done by Z piezo, where the probe tip is mounted on a cantilever (Fig. 6). Usually, the cantilever tip is made from silicon nitride and the elastic constant of the cantilever is less than the interatomic bond strength. The probe motion sensor senses the spacing between the probe and the cantilever and provides a correction signal to the piezo scanner to keep the height constant. The optic lever system consists of a diode laser and a position-sensitive photodetector. Figure 6 represents a schematic operation of the position-sensitive photodetector. In the contact mode of AFM, the tip touches the sample while a scanning, and constant force is applied to the sample. The interatomic force between the tip and the sample is repulsive. The deflection varies as the tip scans the sample and this deflection is measured by laser beam shift and fed back to the scanner. The scanner readjusts its height to keep the distance constant. But in this measurement mode capillary forces arise if thin water layers are present on a sample surface. Therefore, a large class of samples can obtain an electrostatic charge that screens charges causing additional pull and creating frictional forces which may damage the sample.

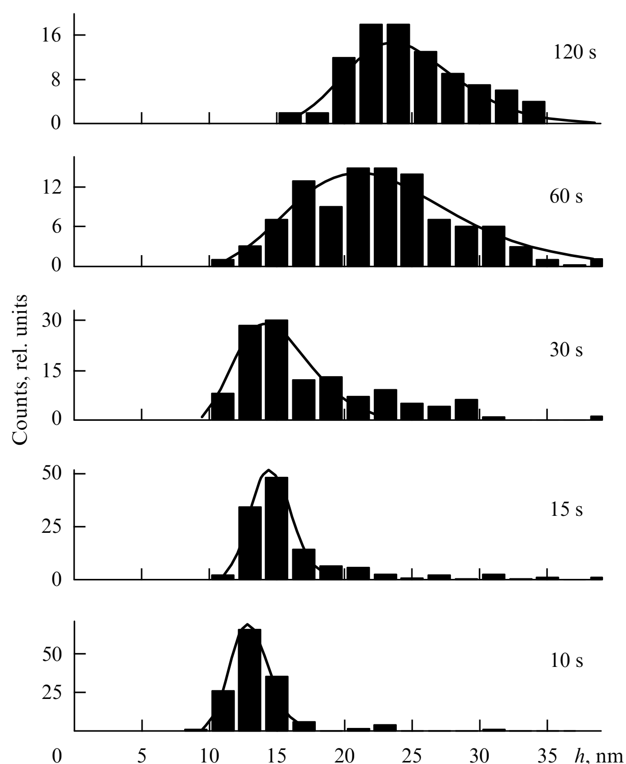

Figure 7. The height analysis for a titanium film when titanium clusters are deposited onto a silicon substrate [35].

In the noncontact mode of AFM, the tip is held above the sample. Then interatomic forces between the tip and sample are attractive and the distance between the tip and surface is kept constant. The cantilever oscillates at the resonant frequency, oscillation amplitude and phase are measured by a laser detection system, and this information is transferred to a scanner. The oscillation amplitude varies due to the van der Waals interaction, and the scanner adjusts height to keep a constant amplitude. This mode of AFM is characterized by a low resolution because the fluid contaminant layer is thicker than the range of van der Waals forces. This mode is used mainly for imaging the magnetic sample surfaces.

In a tapping regime, forced oscillations of a console are excited at a resonant frequency far from the sample surface. The approach of the probe to the sample causes an additional gradient of forces that leads to a shift in the resonant frequency, resulting in a partial exit from the resonance and a decrease in the oscillation amplitude. Scanning in the resonant regime maintains the oscillation amplitude at a given level. Because of a strong dependence of the oscillation amplitude on the distance between the probe and surface this method allows one to measure the surface topology with a high accuracy. This method is applied to the analysis of large samples with remarkable variations in the sample's topology and is used for obtaining high-resolution topological images of samples that are loosely held to the substrate. Also, this method overcomes the problems associated with friction, adhesion, and electrostatic forces. Thus, the tapping mode is suitable for soft samples like biomolecules, polymers, and hard samples such as a silicon wafer. Figure 7 gives an example of the height analysis of a typical tapping mode for Ti clusters deposited on an Si(100) wafer. The measurements are made by AFM in the tapping regime.

The AFM tapping mode image leads to an error in measuring the width of nonspherical clusters as a result of the tip interaction with a nonspherical (flattened) structure on the surface. Then, the width measured W_{meas} is given by

$$W_{\text{meas}} = W + 2d\,, \tag{2.6}$$

where W is the actual width, and the distance d depends on the radius of the tip used. The width obtained in this case reflects a convoluted geometry between the tip geometry and the cluster geometry. In order to solve this problem, the calibration measurements are made with spherical nanoparticles of a known radius and Au colloidal particles of 4 – 5 nm for determining the deconvolution factor.

2.3.3 X-ray methods for characterization of thin films. X-ray photoelectron spectroscopy (XPS), which is also known as electron spectroscopy for chemical analysis (ESCA), was developed in the 1960s by Kai Siegbahn and his research group [49] and is the basis for a powerful and valuable method of surface analysis. Surface analysis by X-ray photoelectron spectroscopy (XPS) is accomplished by irradiating a sample with monoenergetic soft X-rays and analyzing the energy of the emitted electrons. The X-ray line Mg$K\alpha$ (1253.6 eV) or Al $K\alpha$ (1486.6 eV) is usually used (Table 1). The X-ray photons interact with the surface atoms causing the emission of electrons. These emitted electrons are guided to the detector behind a hemispherical mirror system, where the energy of the electrons is measured. A typical result of the XPS-method is given in Fig. 8, where XPS spectra are displayed for titanium clusters deposited on a silicon surface. As can be seen, after 30 min a deposited film changes its chemical composition.

Table 1. Energy and line width of Mg and Al X-ray sources.

X-ray line	Energy, eV	Line width, eV
Mg $K\alpha$	1253.6	0.70
Al $K\alpha$	1486.6	0.85

Because each element has a unique set of binding energies, XPS can be applied to identify and determine chemical compositions and the concentration of elements on the sample surface. Variations in the elemental binding energies or chemical shifts result from differences in the chemical potential and polarizability of compounds. These chemical shifts can be used to identify the chemical state of the materials being analyzed.

An ideal photon source must be sufficiently powerful in order to resolve core levels, its intensity must be high enough to produce a detectable electron flux, which is characterized by a narrow line width, and it must be simple for using and maintaining. Listed in Table 1 are the parameter of Mg and Al sources together with their energies and line widths. The full-width-half-maximum (FWHM) of an XPS peak depends on several factors, but the major contribution comes from the line width of the X-ray line.

In surface studies, the origin of the energy scale is taken as the Fermi level (E_{F}) of the solid. The sample is electrically connected with the spectrometer, so that their Fermi energies are at the same level. Accordingly, the kinetic energy of an emitted photoelectron is given by the relationship

$$E_{\text{kin}} = h\nu - E_{\text{b}} - \Phi_{\text{sp}}\,, \tag{2.7}$$

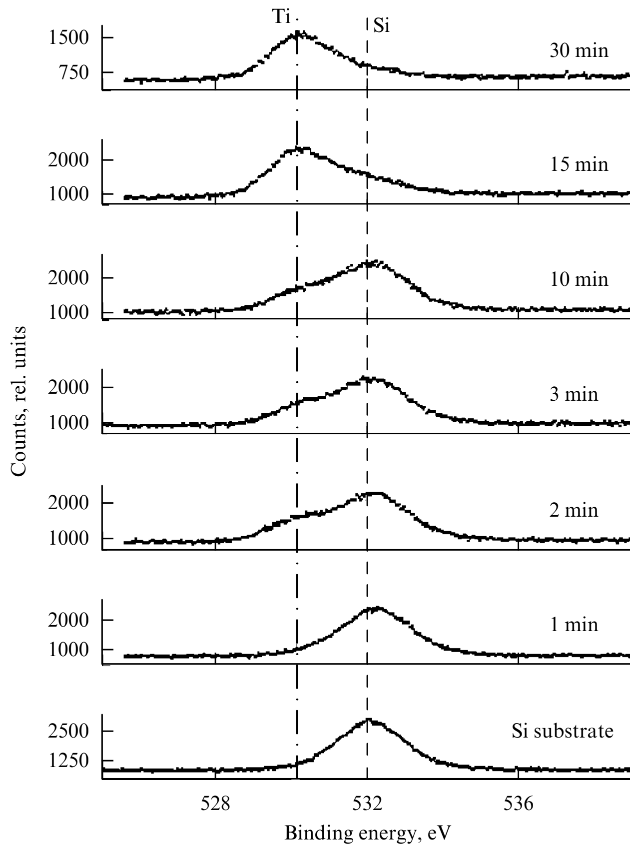

Figure 8. The X-ray photoelectron spectra (XPS) for titanium clusters deposited on a silicon surface at different deposition times.

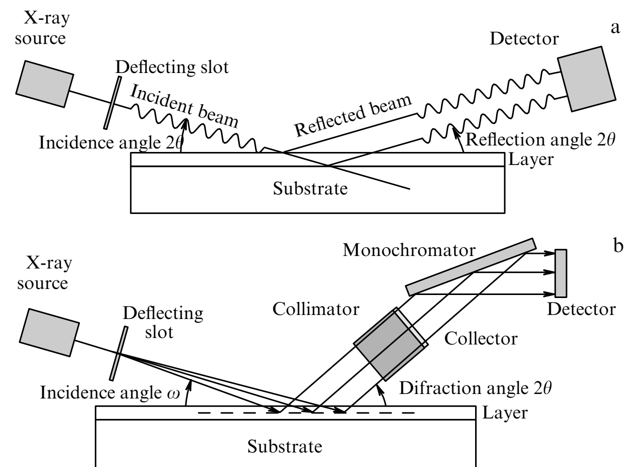

Figure 9. A scheme of the grazing incidence X-ray reflectometry (GIXR) method (a) and a scheme of the grazing incidence X-ray diffractometry (GIXD) method (b) [6].

where $h\nu$ is the photon energy, $E_{\rm b}$ is the binding energy of a released electron, and $\Phi_{\rm sp}$ is the spectrometer work function. The binding energy is the energy difference between the initial and final states after a photoelectron leaves the atom. Because there is a variety of possible final states of ions for each atom, there is a corresponding variety of kinetic energies of the emitted electrons.

Measurement of the X-ray reflectivity around the critical angle for total reflection allows one to accurately determine the film thickness, mass density of the surface, and interface roughness irrespective of the crystalline structure [50 – 55]. The grazing incidence X-ray reflectometry (GIXR) method [56 – 59] is equally well applicable to crystalline, polycrystalline, and amorphous materials; it only requires a sufficient sample flatness. The basic principle of such measurements is illustrated in Fig. 9a. If a thin film is located on a substrate, a constructional interference occurs between the beam reflected from the surface and the beams reflected from the interfaces. Constructional interference results in intensity maxima (Kiessig fringes), whose angular distribution is a characteristic of the layer thickness.

We now consider the GIXR setup that is employed at the Institute of Physics of Greifswald University (Germany) [6] — a Seifert XRD3003TT with a Cu anode (wavelength $\lambda = 1.54$ Å). In reflectivity experiments, the deviation $\delta = n - 1$ of the index of refraction n from unity depends linearly on a material constant which is directly connected with the constituting molecules. For X-rays, this material constant is the electron density (ρ):

$$\delta = \rho r_0 \frac{\lambda^2}{2\pi}\,, \tag{2.8}$$

where r_0 is the Thomson radius. According to this formula, a typical deviation for the refraction coefficient n is on the order of 10^{-5} in reality. This allows introducing an approximation when possible and the measured reflectivity R is described by the Fresnel reflectivity $R_{\rm F}$ of an infinitely sharp interface, modulated by interference effects from the thin surface layer. Then, two critical angles for the total external reflection $\alpha_{\rm cr} = \sqrt{2\delta}$ can be found from the kinematic approximation to the reflectivity:

$$\frac{R}{R_{\rm F}} = \left| \frac{1}{\rho_{\rm sub}} \int \rho'(z) \exp(-\mathrm{i} Q_z z)\, \mathrm{d}z \right|^2 . \tag{2.9}$$

Here, $\rho_{\rm sub}$ is the electron density of the substrate, $\rho'(z)$ is the gradient of the electron density, Q_z is the transfer wave vector, and z is the direction along the surface normal. The electron density profiles may be calculated by an indirect Fourier transform of the master formula (2.9) [60, 61]. Then, the exact matrix formalism may be used to quantify the molecular parameters.

In the treatment of experimental data it is convenient to divide the surface layer into many homogeneous layers. Within the framework of this model, measurements allow one to determine the thickness distribution for the electron density [62]. In any case, the simulated reflectivity is connected with the angular divergence of the spectrometer. The electron density profiles obtained in this manner coincide within the accuracy of the analysis with the profiles obtained by indirect Fourier transformation. Correlation analysis can give more perfect information for the electron distribution in the surface layer. Usually, the relaxation processes change this distribution, because the duration of these processes is roughly 30 min, whereas reflectivity measurements typically take eight hours.

At the same time, the method of grazing incidence X-ray diffractometry (GIXD) [63 – 67] allows one to obtain information about the chemical state of the surface. Therefore, X-ray diffraction is a versatile, nondestructive technique that provides detailed information about the chemical composition and crystallographic structure of natural and manufactured materials [68 – 79]. A crystal lattice constitutes a regular three-dimensional distribution (cubic, rhombic, etc.) of atoms

in space. Atoms are arranged in such a manner that they form a series of parallel planes separated from one another by a distance d that follows from the nature of the material. For any crystal, planes exist in a number of different orientations, each with its own specific d-spacing.

When a monochromatic X-ray beam with wavelength λ is projected onto a crystalline material at an angle θ, diffraction occurs only when the distance travelled by the rays reflected from successive planes differs by a complete number n of wavelengths. By varying the angle θ, Bragg's law conditions are satisfied by different d-spacing in polycrystalline materials. Plotting the angular positions and intensities of the resultant diffracted peaks of radiation produces a pattern, which is a characteristic of the sample. In the case of a mixture of different phases, the resultant diffractogram is formed by the addition of the individual patterns. The general character of such measurements is illustrated in Fig. 9b.

X-rays interact primarily with electrons inside the atoms. Therefore, in diffraction experiments elastically scattered X-rays are detected, and the scattered X-rays carry information about the electron distribution in the materials. Diffracted waves from different atoms can interfere with each other and the resultant intensity distribution is strongly modulated by this interaction. If the atoms are arranged in a periodic fashion as in crystals, the diffracted waves will consist of sharp interference maxima (peaks) with the same symmetry as in the distribution of atoms. Measuring the diffraction pattern therefore allows one to deduce the distribution of atoms in a material.

The peaks in an X-ray diffraction pattern are directly related to the interatomic distances. Let us consider an incident X-ray beam interacting with atoms arranged in a periodic manner. Atoms modelled by hard spheres can be viewed as forming different sets of planes in the crystal. For a given set of lattice planes with an interplanar distance d, the condition for a diffraction peak can be simplified to the form of Bragg's law:

$$2d\sin\theta = n\lambda\,. \tag{2.10}$$

Here, λ is the X-ray wavelength, θ is the scattering angle, and n is an integer representing the order of the diffraction peak. Bragg's law is of importance for the treatment of the X-ray diffraction data.

Observation of X-ray diffraction from very thin films is often hampered by weak diffraction intensities due to the smallness of the diffraction volume. Thin polycrystalline films can be studied advantageously in a highly asymmetric Bragg case. In this technique, the diffraction volume can be increased by decreasing the angle of incidence [80]. One can perform GIXD measurements on a Siemens D5000 diffractometer equipped with a thin-film attachment. The angle range measured was $0.4^\circ/2\theta$ to $3.0^\circ/2\theta$ with a step width of $0.01^\circ/2\theta$ and a time of 30 s for each step. Another diffractometer, an XRD3000 (Seifert), is equipped with special parallel beam optics for grazing incidence measurements of small-angle scattering. An integrated high-temperature chamber (Bühler HDK2.4) enables *in situ* diffractometry measurements at temperatures up to 1000 °C.

Interplanar distances may be determined from peak positions, and the cluster size follows from the integral peak width. There is more detailed information about the methods under consideration and comparisons with each other in Ref. [80].

2.3.4 Visible, UV, and IR spectroscopy. Various standard spectroscopy methods [81–84] are utilized in cluster and cluster plasma experiments. Absorbtion spectroscopy is based on the absorption of monochromatic (laser) radiation. If the intensity of incident monochromatic radiation is I_0 and this radiation passes through a sample of thickness l, the intensity of radiation after passing through the sample is given by

$$I = I_0 \exp(-kl)\,, \tag{2.11}$$

where k is the absorption coefficient of the sample material.

The absorption spectrum of molecules exhibits a number of absorption bands corresponding to structural groups within the molecule. For example, absorption in the UV-spectrum range for the carbonyl group of acetone is similar to absorption for the carbonyl group in diethyl ketone. In studies by the Institute of Physics of Greifswald University, at which we are based, a UV-vis Lambda 900 (Perkin-Elmer) spectrometer is used for UV–visible absorption experiments. The imaginary part of the refraction index is measured, which gives the absorption spectrum of an atomic system. In this method, a light beam from a visible and/or UV light source is decomposed into its component wavelengths by a prism or diffraction grating. Each monochromatic (single-wavelength) beam in turn is split into two equal-intensity beams by a half-mirrored device. One beam, the sample beam, passes through the sample to be analyzed. The other beam, the reference beam, passes through a reference material. The intensities of these light beams are then measured by electronic detectors and are compared. The spectrometer automatically scans all the component wavelengths in the range used. Usually, the ultraviolet (UV) range of the wavelengths is concentrated from 200 to 400 nm, and the visible range varies from 400 to 800 nm. In particular, a typical absorption spectrum of Ag colloidal nanoparticles of an average size of 15 nm (nanoparticles adsorbed on quartz substrate from Ag colloidal solution) has a maximum corresponding approximately to 400 nm, which is typical for Ag nanoparticles resided on the substrates.

TDLAS, an acronym for tunable diode laser absorption spectroscopy, is a technique for measuring the concentration of certain species, such as methane and water vapor, in a gaseous mixture. Moreover, TDLAS is being used in wide spectral region, for example, in the IR range between 3 and 20 μm for measuring the concentrations of free radicals, transient molecules, and stable products in their electronic ground states. TDLAS can also be applied to measure neutral gas temperatures [85] and to investigate dissociation processes in molecular low-temperature plasmas [85–91]. The advantage of TDLAS over other techniques for concentration measurement is its ability to achieve very low detection limits (of the order of ppbv). Along with the concentration, the absorption method allows one to determine the temperature, pressure, molecular velocity, and mass flux of the gas under observation. Sometimes TDLAS may refer to tunable diode laser atomic absorption spectroscopy, a technique that is used in plasma diagnostics. Here, the TDLAS technique is used for measuring metastable atom densities or neutral atom temperature and for identifying small amounts of impurities in plasmas. It is also possible to correlate the metastable atomic densities with the partial pressure of a basic gas in various gases or plasmas. The main advantage of this method compared to optical emission methods is the possibility of

obtaining strong spectral lines with small widths compared to the Doppler width — their width has the same order of magnitude as the natural width of spectral lines (about 1 MHz).

A basic TDLAS setup consists of a tunable diode laser as a light source, transmitting (i.e., beam shaping) optics, an optically accessible absorbing medium, receiving optics, and a detector. The emission wavelength of the tunable diode laser is tuned to the characteristic absorption lines of a species in the gas. This causes a reduction in the measured signal intensity that can be detected by a photodiode, and then allows one to determine the gas concentration and other properties as described later.

Different diode lasers are employed as radiation sources, depending on the sphere of applications and the required range of tuning. In particular, a heterostructure InGaAsP/InP laser provides a wavelength range 0.9 – 1.6 μm, while InGaAsP/InAsP allows one to work in a range from 1.6 to 2.2 μm, etc. These lasers can be tuned by either adjusting their temperature or by changing injection current density into the gain medium. While temperature changes allow tuning over a range of ~ 100 cm^{-1}, it is limited by slow tuning rates of around a few Hz due to the thermal inertia of the system. On the other hand, adjusting the injection current can provide tuning at rates as high as ~ 10 GHz, but it is restricted to a smaller range ($\sim 1-2$ cm^{-1}) over which the tuning can be performed. The typical laser linewidth is on the order of 10^{-3} cm^{-1} or less.

The basic principle behind the TDLAS technique is simple. The focus here is on a single absorption line in the absorption spectrum of a particular species of interest. The wavelength of a diode laser is tuned over a particular absorption line of interest and the intensity of the transmitted radiation is measured. This intensity can be related to the concentration of the species according to the Beer – Lambert law (2.11) which connects the intensity of transmitted radiation $I(\nu)$ for a given frequency ν with the passing path L by the relation

$$I(\nu) = I(\nu_0)\exp\left[-\alpha(\nu)L\right], \qquad (2.12)$$

where the frequency ν_0 corresponds to the line center, $I(\nu_0)$ is the intensity of the incident radiation, $\alpha(\nu) = \sigma(\nu)N = S(T)\phi(\nu-\nu_0)$ is the absorbance of the medium, $\sigma(\nu)$ is the absorption cross section of the absorbing species, N is the number density of the absorbing species, $S(T)$ is the line strength (i.e., the total number of absorptions per molecule) of the absorbing species at the temperature T, and $\phi(\nu-\nu_0)$ is the frequency distribution function for the particular absorption line.

There are various ways to measure the temperature T of an absorbed component simultaneously with other parameters under the assumption that the line strength $S(T)$ is a temperature function only. Two different absorption lines for the same species are probed while sweeping the laser across the absorption spectrum. Evidently, the ratio of the integrated absorbtion intensities is then a temperature function only and is given by

$$R = \left(\frac{S_1}{S_2}\right)_T = \left(\frac{S_1}{S_2}\right)_{T_0}\exp\left[-hc(E_1-E_2)\left(\frac{1}{T}-\frac{1}{T_0}\right)\right], \qquad (2.13)$$

where T_0 is some reference temperature at which the line strengths are known, and $\Delta E = E_1 - E_2$ is the difference in the lower energy levels involved in the transitions for the lines under consideration.

Another way to measure the temperature is based on measurements of the Doppler line width of the species at a given temperature that is defined by the following expression:

$$\mathrm{FWHM}\,(\Delta\nu_D) = \nu_0\sqrt{\frac{8T\ln 2}{mc^2}} = 7.1623\times10^{-7}\nu_0\sqrt{\frac{T}{M}}, \qquad (2.14)$$

where m is the molecular mass of the species, and M is the molecular weight taken in g mol^{-1} if the temperature T is measured in kelvins. This method is valid at low gas pressures (on the order of a few mbar), which holds true for a magnetron plasma. At higher pressures ($\sim$ dozens of mbar or more) broadening of spectral lines is determined by collision processes and this approximation is not valid. One can find all the characteristics of absorbtion spectroscopy methods which are in use for plasma diagnostics in Ref. [92].

2.3.5 Diagnostics of electrons and ions in a plasma. A magnetron plasma is rarefied enough and it allows one to use a standard Langmuir probe in order to measure the number density of electrons, their temperature, and the electric potential (voltage) of the plasma. The Langmuir probe constitutes a small conductive electrode whose dimensions are small compared to the mean free path of electrons in a buffer gas. The Langmuir probe allows one to diagnose the electron energy distribution functions in a plasma by measuring the probe current as a function of its voltage.

The measurements with electric probes belong to the oldest, as well as to the most often employed procedures of diagnostics of rarefied low-temperature plasma. Originally developed in the 1920s by Langmuir and his co-workers [93], the method has been the subject of many extensions and further developments in order to widen its applicability to more general conditions [94 – 96].

Among various methods of plasma detection, the Langmuir probe diagnostics is probably the simplest one, since it consists in sticking a wire into the plasma and measuring the current to it at various applied voltages. However, the wire must be carefully designed in order to not perturb the plasma or not be destroyed by it. Unfortunately, the interpretation of the current – voltage ($I-V$) curves may be ambiguous and requires a special analysis. Nevertheless, various versions of probe diagnostics are used, including emissive probes, double probes, capacitive probes, oscillation probes, probes in flowing or high-pressure plasmas, and probes in a magnetic field. On the other hand, the most widespread use of Langmuir probes at present is in the semiconductor industry, where radio-frequency (rf) or direct current (DC) sources are used to produce plasmas for etching and film deposition. These partially ionized plasmas require special techniques in probe construction and theory. Figure 10 [151] presents an example of probe measurements and gives the electron number density and the average electron energy as functions of the magnetron power for an aluminium magnetron plasma far from the cathode where the magnetic field is absent.

In various technological applications of a low-temperature plasma, like magnetron sputtering, a magnetic field is applied to confine the plasma and to increase the growth or etching rate. The magnetic field in these systems can be either inhomogeneous, usually created by permanent magnets and taking place in a planar unbalanced magnetron discharge, or

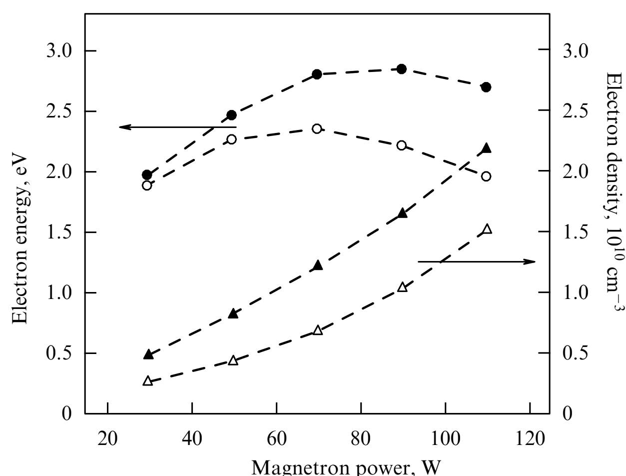

Figure 10. The electron number density and the mean electron energy depending on the magnetron discharge power for a titanium magnetron plasma at a distance 8.8 cm from the cathode and at an argon pressure of 0.7 Pa. Open symbols — balanced MD regime, full symbols — unbalanced MD regime [151].

almost homogeneous, being created by coils with a magnetic field whose strength is not very high. In using the Langmuir probe as a diagnostic tool in these systems, the question arises as to what the limiting parameter $\beta = H/p$ is for such measurements, where H is the magnetic field strength, and p is the gas pressure. The analysis performed on the Langmuir probe data [96] allows one to consider separately four cases. If $\beta \ll 1$, and H is small, the influence of the magnetic field can be ignored. If $\beta \approx 1$, one can use formulas without the magnetic field and invoke some corrections. In the case $\beta > 1$, a general method of treatment may be employed for the qualitative analysis. If $\beta \gg 1$, i.e., H is very strong, the probe characteristics are no longer interpretable. Nevertheless, the probe characteristics may be treated, taking into account plasma magnetization. The case of a strong magnetic field and a very strong negative voltage of the probe with respect to the plasma is of importance [97, 98]. These problems are the subject of various speculations [99], and the analysis of various aspects of the influence of the magnetic field on the probe measurements [100 – 105] has been carried out. In particular, Langmuir probe measurements for cylindrical magnetron discharge are discussed in Refs [106, 107].

The mass-spectrometric method, consisting in measuring currents for different mass-to-charge ratios of ions, allows one to solve various problems of gas and plasma diagnostics, including the mass distribution of atomic particles in a gaseous mixture, determination of the isotopic composition of one or more elements in a compound, obtaining the number densities of various gaseous components, studying the fundamentals of gas-phase ion chemistry (the chemistry of ions and neutral atomic particles in a vacuum), determining the structure of compounds by observing the fragmentation of the compound, and determining other physical, chemical, or even biological properties of compounds.

A mass spectrometer is a device used for obtaining the mass spectrum of ions in order to determine a sample composition. A typical mass spectrometer contains three main parts: an ion source, a mass analyzer, and a detector. The ion source is the part of the mass spectrometer that ionizes the material, and ions formed are analyzed in the mass analyzer where the ions are transported using magnetic or electrical fields. Techniques for ionization have been the key to determining what types of samples can be analyzed by this mass spectrometer. For example, electron ionization and chemical ionization are utilized for gases and vapors. In chemical ionization sources, ionization results from chemical ion-molecular reactions during collisions in the source. Inductively coupled plasma sources are employed primarily for metal analysis on a wide array of sample types. Others include fast atom bombardment (FAB), thermospray, atmospheric pressure chemical ionization (APCI), secondary ion mass spectrometry (SIMS), thermal ionization, and so forth.

Mass analyzers separate the ions according to their mass-to-charge ratio. Operation of all the mass spectrometers is based on the dynamics of charged particles in electric and magnetic fields in a vacuum, where the following relation is applied:

$$\frac{m}{q}\,a = \mathbf{E} + \frac{1}{c}\,[\mathbf{vH}]\,, \tag{2.15}$$

where m is the ion mass, a is the acceleration, q is the ionic charge, $\mathbf{E}$ is the electric field strength, and $[\mathbf{vH}]$ is the vector cross product of the ion velocity and the magnetic field strength. Together with the particles' initial and boundary conditions, equation (2.15) completely determines the particles' motion in space and time and therefore is the basis of the mass-spectrometry theory. It immediately reveals that two particles with the same charge-to-mass ratio behave exactly the same.

There are some modifications of mass analyzers, but they can be divided into two types: static, and dynamic. In the first type of the analyzer, static magnetic and electric fields are used for separating ions with different masses. Dynamic mass analyzers are characterized by a higher accuracy and better resolution, and the mass separation proceeds in them by using a time dependence for electromagnetic field strengths. Various types of dynamic mass spectrometers have been developed [108], for instance, time-of-flight, omegatrons, rf, and quadrupole spectrometers. In spite of the different character of electromagnetic fields used in various types of dynamic mass spectrometers, all of them are operated according to this same law (2.15). We will consider below the quadrupole mass spectrometer that is employed for the analysis of parameters and processes in a low-temperature plasma. The quadrupole mass spectrometer was invented by Paul and Steinwedel in 1953 [108]. Reviews of this diagnostic method were given in several papers in the past [109 – 112]. Note that the wide application of exactly this type of mass spectrometer is connected with its small size, ease of assembly and usability, and comprehensive setup.

In particular, the QMF200 quadrupole mass filter is used to analyze and filter charged clusters. Mechanically, the core of the quadrupole assembly consists of four rods (see Fig. 4b) and a detector plate on which the cluster ion current can be measured. The opposite rods are electrically connected to each other. A positive voltage $U + V\cos 2\pi ft$ having a DC and AC component (of frequency f) is applied to one pair of poles; the negative voltage $(-U - V\cos 2\pi ft)$ is applied to the other pair. The cluster ions enter along the axis of the quadrupole and oscillate due to the electric field. The motion of ions inside the quadrupole is described by the Mathieu equation [113]. Clusters can be selected according to their mass-to-charge ratio by the quadrupole electric field, so that

ions of a definite mass will be transmitted to the ion detector plate. The parameters, which can be varied to allow clusters of a particular mass to pass through the filter, are U, V, and f.

The mass M of the clusters being detected is directly proportional to the amplitude of the AC voltage V (volts) applied to the poles and inversely proportional to the square of the frequency f (kHz) according to the formula [114]

$$M = 7 \times 10^7 \left(\frac{kV}{f^2 d^2}\right), \qquad (2.16)$$

where d is the diameter of the poles, and k is the correction factor. Scanning V, whilst monitoring the ion current from the quadrupole exit, allows the mass spectrum of the cluster beam to be acquired. The ratio of U/V (resolution) must be kept constant throughout. The frequency of voltage applied to the poles determines the mass range over which it is scanned. The ratio U/V defines the width of the cluster mass range transmitted through the filter. This relationship can be proven by solving the Mathieu equation for particle trajectories along a quadrupole axis. The theoretical resolution can be expressed as

$$\frac{\Delta M}{M} = 7.936\left(0.16784 - \frac{U}{V}\right). \qquad (2.17)$$

We now give the parameters of the quadrupole mass spectrometer that is employed at the Institute of Physics of Greifswald University [6]. Grounded entrance and exit apertures shield the cluster beam from the end of the quadrupole rods and also help to restrict the beam. An isolated aperture plate beyond the exit aperture is used to monitor the transmitted cluster ions. This plate can also be biased (+9 or −9 V) to extract more ions from the beam during the measurement of the cluster size. Ion steering plates fitted at the end can be used to separate the ionized mass-selected cluster beam from the neutral cluster beam. The quadrupole rods are 25.4 mm in diameter and have a length of 25 cm. The voltage range is 1 – 250 V, and the frequency ranges between 3 and 100 kHz. These parameters allow particles to be measured and filtered between ~ 30 and $\sim 3 \times 10^6$ a.m.u. The typical usable cluster size resolution reaches $\sim 2\%$. In QMF200 there is one setup mode and two operational modes. In the scan mode, V (and hence the cluster mass) can be scanned, which allows one to monitor the cluster ion current. During this operation, the U/V ratio is kept constant, and U cannot be controlled. In the filter mode, V (mass) can be chosen and the resolution U/V can be adjusted, which allows one to extract the clusters of a given mass.

The mass-spectrometric analysis of clusters allows us to measure the size distribution of charged clusters. This operation may be performed on the basis of AFM, as described above in Section 2.3.2. We compare in Fig. 11 the results obtained by these two methods. In this case, clusters of a certain size where extracted by a filter and then were detected by the quadrupole mass spectrometer and by the AFM analysis of clusters deposited on the substrate.

The final element of the mass spectrometer is a detector. The detector records the charge induced or current produced, when an ion passes by or hits a detector surface. In scanning, the signal produced in the detector in the course of the scan is compared with that of a given ratio m/Z for a calibrated signal. This permits one to determine how many ions with a given m/Z are present in the beam. Typically, various types of

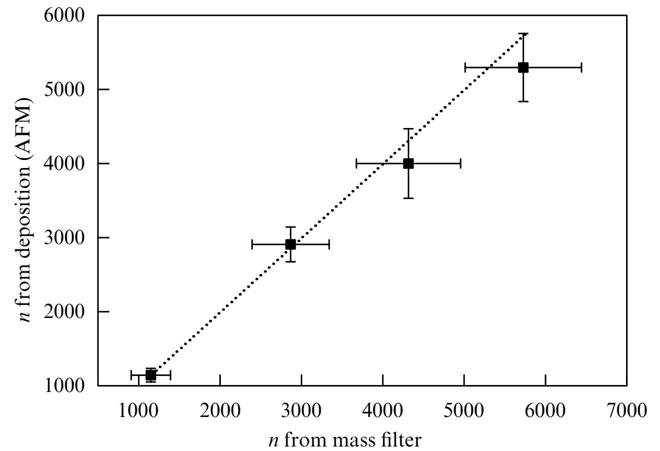

Figure 11. Size of silver clusters obtained by mass-spectrometric and force-atomic-microscopic methods [235].

electron multipliers may be used with other detectors (such as Faraday cups). Because the number of ions leaving the mass analyzer at a particular instant is typically quite small, significant amplification is often necessary to get a signal. Microchannel plate detectors are commonly used in modern commercial instruments. In Fourier transform ion cyclotron resonance, the detector consists of a pair of metal plates within the mass analyzer region which the ions only pass near. No DC current is produced, only a weak AC image current is produced in a circuit between the plates.

3. Processes in a magnetron plasma involving metal atoms

3.1 Emission of fast metal atoms by cathode bombardment with ions

The important peculiarities of magnetron discharge are the generation of fast metal atoms as a result of bombardment of the cathode by discharge ions and the process of formation of secondary electrons and ions that supports a self-sustained discharge. Simultaneously, collisions of ions with the cathode results in a release of cathode atoms. We consider below various aspects of this process. Table 2 gives the probabilities of atom formation per ion (the sputtering yield) according to evaluations on the basis of the SRIM (Stopping and Range of Ions in Matter) code [117, 118] and measurements [115, 116] (in parentheses). In addition, the portion η of energy that is consumed upon formation of sputtered atoms is tabulated. As is seen, the sputtering yield S (the number of sputtering atoms per incident ion) and the average energy E_a of released atoms grows with an increase in the discharge voltage U.

The sputtering yield is on the order of unity and is roughly proportional to the ion energy in the range of typical ion energies between 200 and 600 eV [123]. The sputtering yield depends on the type of incident ion and cathode material [124, 125]. Atoms released are directed mostly from the cathode, and the narrower the range of angles for velocities of releasing atoms with respect to the perpendicular to the cathode, the higher the ion energy. Furthermore, the more the energy of an incident ion, the less the typical angle between a released atom velocity and the perpendicular to the cathode surface. Figure 12 depicts the angle distribution for sputtering atoms at different ion energies [126, 127].

Table 2. Sputtering yield S for bombardment of a metal cathode by argon ions.

Cathode material	S, atoms/ion		E_a, eV		$\eta = S(E_a/E_i)$	
	$U = 300$ V	$U = 500$ V	$U = 300$ V	$U = 500$ V	$U = 300$ V	$U = 500$ V
Al	0.33 (0.65)	0.52	6.6	8.2	0.01	0.01
Ti	0.35 (0.33)	0.51	21	25	0.03	0.03
Fe	0.8 (0.76)	1.24	17	20	0.06	0.07
Cu	1.3 (1.6)	2.0	15	17	0.09	0.09
Co	0.96	1.4	17	20	0.07	0.08
Ni	1.0	1.5	17	19	0.08	0.08
Zn	2.9	4.2	9	9.3	0.12	0.11
Mo	0.59	0.86	26	31	0.07	0.07
Ag	1.4	2.0	15	17	0.11	0.09
Pd	1.3	1.9	18	20	0.12	0.10
Ta	0.52	0.79	23	28	0.07	0.06
W	0.53 (0.4)	0.81	23	28	0.07	0.06
Pt	0.86	1.1	19	22	0.09	0.07
Au	1.2	1.9	15	17	0.08	0.09

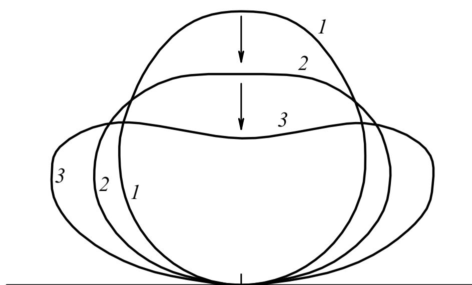

Figure 12. The angular distribution of atoms released at ion energies of 5 keV (*1*), 300 eV (*2*), and 100 eV (*3*) [126, 127].

Since the energy of an incident ion exceeds significantly the binding energy of liberating atoms in solids, one can find the energy distribution function $f(\varepsilon)$ for the atoms released as a result of pair collisions between an incident ion and bound atoms [128]. Within the framework of elastic ion–atom scattering one can use different assumptions which concern the released atom interaction with an environment [124, 125, 128, 129]. It is convenient to employ the following distribution function [129], whose correctness increases with an increase in the ion energy:

$$f(\varepsilon)\,\mathrm{d}\varepsilon = C\left(1-\sqrt{\frac{E_{\mathrm{bn}}+\varepsilon}{\gamma E_{\mathrm{i}}}}\right)\frac{\varepsilon\,\mathrm{d}\varepsilon}{(E_{\mathrm{bn}}+\varepsilon)^3}\,, \quad \gamma = \frac{4m_{\mathrm{i}}m_{\mathrm{a}}}{(m_{\mathrm{i}}+m_{\mathrm{a}})^2}\,.$$

Here, C is the normalization factor, m_i and m_a are the ionic and atomic masses, E_{bn} is the binding energy of a bound atom on the solid surface, and E_i is the average ion energy that is connected with the voltage U of magnetron discharge through the following expression [22]

$$E_{\mathrm{i}} = 0.733\,U\,. \tag{3.1}$$

We used above and will use below the results of calculations on the basis of the SRIM code [117, 118]. This is a group of programs for calculating the ion stopping in matter in a wide range of ion energies (up to 2 GeV/a.m.u.) and for various ions on the basis of the binary collision approximation model, assuming a randomized or structureless target, i.e., each next collision partner can be found by a random selection process, which is why these simulations are sometimes called Monte Carlo programs. Also, a quantum mechanical treatment of ion–atom collisions (assuming a moving atom to be an 'ion' and all target atoms to be 'atoms') is in use. This calculation is made very efficient by employing the statistical algorithms, which allow the ion to make jumps between calculated collisions, and then averaging the collision results over the intervening gap. During the collisions, the ion and atom interact through a screened Coulomb potential, including exchange and correlation interactions between the overlapping electron shells. The ion experiences long-range interactions creating electron excitations and plasmons within the target. These are described by including a description of the target's collective electronic structure and interatomic bond structure, when the calculation is set up (tables of nominal values are supplied). The charge state of the ion within the target is described using the concept of effective charge, which includes a velocity-dependent charge state and long-range screening due to the collective electron sea of the target. This (Monte Carlo) simulation program has various versions and modifications, e.g., TRIM [119], TRIM.SP [120], and TRIDYN [121]. A discussion of the various simulation programs may be found in Ref. [122].

At some distances from the cathode, the flux of sputtered atoms includes fast atoms which reach this point without scattering. The scattering of sputtered atoms in a gas is expressed on the basis of the dependence of atom deposition on a target as a function of the target distance. Indeed, if we assume that deposited atoms have reached the target without collisions, then the flow of these atoms as a function of the distance x from the cathode takes the form

$$j = j_0 \exp\left(-\frac{x}{\lambda}\right), \tag{3.2}$$

where λ is the mean free path for fast atoms. This formula is valid until the contribution of thermalized atoms to deposition is small, i.e., until the distance x is not large. Note that because sputtered atoms are distributed over energies and angles, this mean free path is an averaged quantity.

In reality, this operation is used for applications when a plate is covered by a cathode metal [115, 116, 130]. In this case, the covering plate is placed inside the magnetron chamber at some distance from the cathode. This distance is on the order of λ. Indeed, if this distance is large, fast atoms do not reach the target and return to the cathode, i.e., the probability of using a sputtering atom is small. On the contrary, if this distance is small, fast sputtering atoms bombard the plate, which can lead to breaking the covering

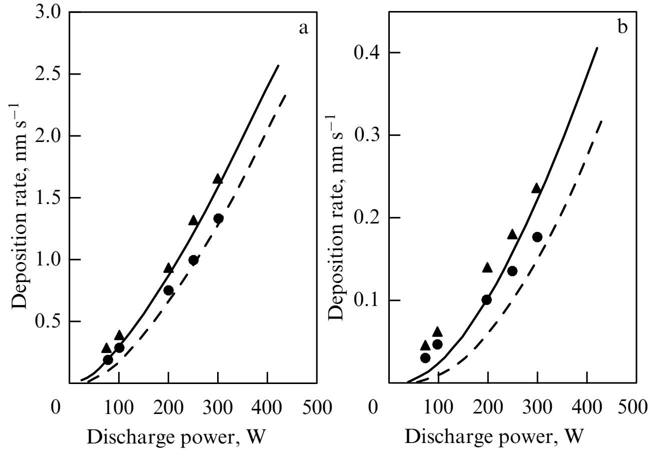

Figure 13. Experimental (symbols) and calculated (curves) results for the deposition rate of Al at an argon pressure of 5 mTorr (triangles, solid line) and 10 mTorr (circles, dashed line) for the cathode – substrate distances of 10.8 cm (a) and 22 cm (b) [127].

and reduces its quality. Figure 13 presents such an example where the rate of covering growth is represented at different discharge powers and distances of the object covered from the cathode.

We now connect the mean free path λ of a fast atom in a buffer gas with the cross section of scattering of colliding atoms. Let us take the mean free path as a distance where the vector of the average atomic momentum is zero. We start from the kinetic equation for the velocity distribution function $f(\mathbf{v})$ for fast metal atoms, which has the form

$$\frac{\partial f(\mathbf{v})}{\partial t} = \int \left[f(\mathbf{v}')\,\varphi(\mathbf{v}_1') - f(\mathbf{v})\,\varphi(\mathbf{v}_1) \right] \mathrm{d}\sigma\, \mathrm{d}\mathbf{v}_1 \,. \tag{3.3}$$

Here, $\varphi(\mathbf{v}_1)$ is the velocity distribution function for buffer gas atoms, $\mathbf{v}$, $\mathbf{v}_1$ are the velocities of metal and buffer gas atoms before collision, $\mathbf{v}'$, $\mathbf{v}_1'$ are these velocities after collision, and $\mathrm{d}\sigma$ is the differential cross section of elastic scattering for the collision of a fast metal atom with a buffer gas atom.

Multiplying this equation by the momentum $m\mathbf{v}$ of fast atoms, where m is the mass of a metal atom, and integrating over the atomic velocities, we obtain the equation for the average atomic momentum P_x:

$$N\,\frac{\mathrm{d}P_x}{\mathrm{d}t} = \int m(v_x' - v_x) g\, \mathrm{d}\sigma\, f(\mathbf{v})\,\varphi(\mathbf{v}_1)\,\mathrm{d}\mathbf{v}\,\mathrm{d}\mathbf{v}_1 \,,$$

$$P_x = \int m v_x f(\mathbf{v})\,\mathrm{d}\mathbf{v} \,,$$

where x is the initial direction of the atom velocity, N is the number density of metal atoms, and the distribution functions are normalized to the number densities of corresponding atoms. We used above the principle of detailed balance, which assures the equation invariance under time reversal and gives

$$\int \mathbf{v} f(\mathbf{v}')\,\varphi(\mathbf{v}_1')\,\mathrm{d}\sigma\,\mathrm{d}\mathbf{v}\,\mathrm{d}\mathbf{v}_1 = \int \mathbf{v}' f(\mathbf{v})\,\varphi(\mathbf{v}_1)\,\mathrm{d}\sigma\,\mathrm{d}\mathbf{v}\,\mathrm{d}\mathbf{v}_1 \,.$$

We now express the metal atom velocity before ($\mathbf{v}$) and after ($\mathbf{v}'$) collision in terms of the relative velocity of colliding atoms $\mathbf{g}$ and the center-of-mass velocity $\mathbf{V}$ through the relationship

$$\mathbf{v} = \mathbf{g} + \frac{m\mathbf{V}}{m+M} \quad \text{and} \quad \mathbf{v}' = \mathbf{g}' + \frac{m\mathbf{V}}{m+M} \,,$$

where M is the mass of a buffer gas atom. This gives $m(\mathbf{v} - \mathbf{v}') = \mu(\mathbf{g} - \mathbf{g}')$, where $\mu = mM/(m+M)$ is the reduced mass of colliding atoms. The relative velocity of atoms after collision can be represented in the form $\mathbf{g}' = \mathbf{g}\cos\vartheta + \mathbf{k} g \sin\vartheta$, where ϑ is the scattering angle, and $\mathbf{k}$ is a unit vector directed perpendicular to $\mathbf{g}$. Because of the random character of scattering, the second term disappears after averaging over scattering angles, i.e., the integration over scattering angles gives

$$\int (\mathbf{g} - \mathbf{g}')\,\mathrm{d}\sigma = \mathbf{g}\sigma^*(g) \,,$$

where

$$\sigma^*(g) = \int (1 - \cos\vartheta)\,\mathrm{d}\sigma$$

is the transport cross section for atomic scattering. Thus, we obtain the following equation for the rate of variation of the directed velocity of a metal atom:

$$\frac{\mathrm{d}P_x}{\mathrm{d}t} = -\int \mu g_x g \sigma^*(g) f(\mathbf{v})\,\varphi(\mathbf{v}_1)\,\mathrm{d}\mathbf{v}\,\mathrm{d}\mathbf{v}_1 \,. \tag{3.4}$$

We now use peculiarities of the relaxation process under consideration. The metal atom velocity is large compared to a thermal velocity of buffer gas atoms, so that we have $\varphi(\mathbf{v}_1) = N_{\mathrm{a}}\delta(\mathbf{v}_1)$, where N_{a} is the number density of buffer gas atoms, and $\mathbf{g} = \mathbf{v}$. Assuming that the kinetic energy of a metal atom does not vary remarkably during relaxation, we take $f(\mathbf{v}) = N\delta(\mathbf{v} - \mathbf{v}_0)$, where $\mathbf{v}_0$ is the initial velocity of a released metal atom. As a result, the relaxation equation (3.4) takes the form

$$\frac{\mathrm{d}v_x}{\mathrm{d}t} = -\frac{v_x}{\tau_{\mathrm{P}}} \,, \qquad \tau_{\mathrm{P}} = \frac{M+m}{M}\,\frac{1}{N_{\mathrm{a}} v \sigma^*(v)} \,. \tag{3.5}$$

Here, v_x is the component of the mean velocity of a released atom in the direction of the initial velocity, and during the relaxation time τ_{P} a released metal atom loses its initial direction of motion. The latter happens after one or two collisions with buffer gas atoms. Note that thermalization of released atoms proceeds after many such collisions.

Comparing formulas (3.2) and (3.5), one can connect the mean free path λ of metal atoms with the transport cross section $\sigma^*(v)$ for their collisions with buffer gas atoms through the formula

$$\lambda = \frac{M+m}{M}\,\frac{1}{N_{\mathrm{a}}\sigma^*(v)} \,. \tag{3.6}$$

This formula was used in the treatment of the experimental data collected in Table 2. Correspondingly, formula (3.2) can be represented in the form

$$j = j_0 \exp\left(-N_{\mathrm{a}}\sigma^*(v) x\,\frac{M}{M+m}\right) , \tag{3.7}$$

where $\sigma^*(v)$ is the transport cross section of colliding atoms at an indicated relative velocity, and this transport cross section is given in Table 3.

Table 3. Transport cross sections σ^* for atoms sputtered in argon and some other parameters characterizing sputtering by ion bombardment of various cathode materials.

Element	P, W	U, V	σ^*, Å^2	σ^*/σ_0	E_i, eV	S, atom/ion	E_a, eV/atom
Al	50	280	22	6.7	205	0.30	6.5
Cr	500	480	0.65	12	350	1.1	19
Cr	50	340	1.3	60	250	0.83	17
Cu	500	470	2.4	29	350	1.9	17
Ge	500	440	2.9	23	320	0.99	23
Ge	300	490	3.1	22	360	1.1	24
Mo	50	260	2.0	34	190	0.52	26
Mo	20	280	2.5	27	205	0.55	26
Si	300	530	10	12	390	0.39	10
Si	100	620	12	9.7	450	0.45	11
W	100	270	0.41	150	200	0.48	23
W	20	240	2.2	30	180	0.43	21

Note. The transport cross sections σ^* were restored from experimental data [131, 132]. σ^*/σ_0 is the ratio of sputtered atoms scattered by argon atoms to total atomic cross sections of colliding atoms according to Ref. [133]. $\sigma_0 = \pi(r + r_{Ar})^2$, where r is an effective radius of a released atom, and r_{Ar} is the argon atom radius. These data relate to a given voltage U of a DC magnetron discharge and discharge power P; E_i is the ion energy according to formula (3.1). Sputtering yield (S) is evaluated on the basis of the SRIM code, in the same way as E_a, which is an average energy of released atoms.

Table 4. The diffusion cross sections σ^* for a collision of two identical inert gas atoms and gas-kinetic cross sections σ_{gas} at room temperatures, expressed in 10^{-15} cm^2. The indicated energy E is the energy of a fast atom in the laboratory frame of reference.

Element	σ^* ($E = 10$ eV)	σ^* ($E = 1$ eV)	σ_{gas}
Ne	0.43	0.97	1.8
Ar	0.66	1.6	3.8
Kr	0.71	2.0	4.8
Xe	1.3	2.7	6.6

Comparing the generation of free metal atoms in a buffer gas from the cathode in magnetron discharge and that from a heated metal surface, one can find the principal difference in these processes, because in the first case fast atoms are released, and therefore they move far from the cathode, so that the probability for their return to the cathode may be small. In the second case, the probability of an evaporating atom attaching to the heated surface is close to unity, while the probability of this atom being removed from the surface is small compared to unity. In the first case, it is of importance that the cross section for scattering of metal atoms in collisions with atoms of a buffer gas be less than that for thermal metal atoms, so that the mean free path of fast metal atoms is large compared to that of thermal atoms. To demonstrate this, we compare in Table 4 the cross section of the collision of a fast inert gas atom with an atom of thermal velocity, as well as gas-kinetic cross sections for such collisions, i.e., the diffusion cross sections for the collisions of thermal atoms. The interaction potentials for two identical inert gas atoms at interaction energies of several eV are taken from Ref. [134]. Table 4 exhibits the significance of a high energy of released metal atoms in magnetron discharge for the conservation and utilization of these atoms in a buffer gas.

3.2 Nucleation processes in a buffer gas involving metal atoms

Bombardment of the cathode by plasma ions leads to the emission of metal atoms from the cathode. As a result, the number density of metal atoms in the buffer gas exceeds the saturation vapor density, causing nucleation of the vapor. The growing clusters are located in a restricted aggregation region where they capture free metal atoms. The clusters leave the aggregation region as a result of diffusion or flowing of the buffer gas and trend to spread uniformly over all the space inside the magnetron chamber.

Ultimately, some clusters depart from the magnetron chamber through an orifice and are deposited on a substrate. The cluster flux onto the substrate surface, as well as the cluster size, is restored from the measurement of the cluster area density on the surface for a given deposition time. This allows one to estimate the cluster number density in the magnetron chamber. Below, we analyze the character of the generation and transport of metal atoms on the basis of the above experimental results.

The formation and growth of metallic clusters start from the formation of free metal atoms. We use the following scheme of the processes of cluster growth in the magnetron chamber where free metallic atoms are located [135–137, 139]:

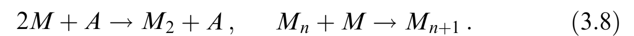

$$2M + A \to M_2 + A\,, \qquad M_n + M \to M_{n+1}\,. \tag{3.8}$$

Here, A is the buffer gas atom, M is the metallic atoms, and the nucleation starts from the three-body process of formation of a diatomic molecule, and then it is a nuclei of condensation in pair processes of atomic attachment to a cluster. The rate constant of the three-body process lies in the range $K \sim 10^{-33} - 10^{-32}$ cm^6 s^{-1} [135, 140], and the values of K for some processes are given in Table 5. The first process in Table 5 proceeds at room temperature, while in the second and third cases the plasma temperature is approximately 200 K, but these processes take place in a hotter region and the temperature is higher, though the thermal energy of the joining atoms is significantly lower than the dissociation energy of the forming molecule. Note that this character of cluster formation and growth from an atomic vapor corresponds to a general concept of this process.

Table 5. The rate constant K (in 10^{-33} cm^6 s^{-1}) of a three-body process $2M + \mathrm{Ar} \to M_2 + \mathrm{Ar}$.

M	K	References
Cu	3.0	[141]
Ti	2.5	[142]
Ag	5.5	[143]

The rate constant of atomic attachment to the cluster surface within the framework of the liquid drop model for a cluster consisting of n atoms has the form [135, 137, 139]

$$k_n = k_0 n^{2/3}\,, \qquad k_0 = \sqrt{\frac{8T}{\pi m}}\,\pi r_W^2\,. \tag{3.9}$$

Here, T is the temperature, m is the atomic mass, and r_W is the Wigner–Seitz radius for a forming cluster that is assumed to be equal to the Wigner–Seitz radius of a bulk metal. Table 6 contains the values of the Wigner–Seitz radius and the specific rate constant k_0 of attachment for some metals [137, 139, 144, 145]. Statistical averaging of these values for the data of Table 6 gives $r_W = (1.6 \pm 0.1)$ Å, $k_0 = (2.2 \pm 0.7) \times 10^{-11}$ cm^3 s^{-1} at $T = 1000$ K.

The character of the nucleation process (3.8) is determined by the value of the dimensionless parameter [139,

Table 6. Parameters of large clusters.

Element	T_b, K	r_W, Å	k_0, 10^{-11} cm^3 s^{-1}	ε_0, eV
Al	2730	1.65	4.3	3.09
Ti	3560	1.67	3.3	4.89
V	3680	1.55	2.7	5.1
Cr	2944	1.41	2.2	3.79
Fe	3023	1.47	2.4	3.83
Co	5017	1.45	2.2	4.10
Ni	3100	1.44	2.2	4.13
Cu	2835	1.47	2.3	3.40
Zn	1180	1.58	2.5	1.22
Zr	4650	1.85	2.9	6.12
Mo	4912	1.60	2.1	6.30
Pd	3236	1.58	2.0	3.67
Ag	2435	1.66	2.2	2.87
Ta	5731	1.68	1.7	8.1
W	5830	1.60	1.5	8.59
Re	5880	1.58	1.5	7.62
Os	5300	1.55	1.4	7.94
Ir	4700	1.58	1.5	6.5
Pt	4098	1.60	1.5	5.4
Au	3129	1.65	1.6	3.65
U	4091	1.77	1.7	4.95

Note. T_b is the boiling point, i.e., the temperature at which the saturated vapor pressure over a plane surface is 1 atm, r_W is the Wigner – Seitz radius, k_0 is the reduced rate constant of atomic attachment to a cluster at a temperature of 1000 K [in accordance with formula (3.9)], and ε_0 is the atomic binding energy in a bulk metal at the melting point.

142, 145 – 147]

$$G = \frac{k_0}{KN_a} . \tag{3.10}$$

Usually, $G \gg 1$, so that the first nucleation stage with the formation of diatomic molecules lasts long compared with the attachment of subsequent atoms to molecules and clusters. This leads to large average cluster sizes at any instant of time.

We now consider the character of the transformation of metal atoms into clusters in a buffer gas if at the beginning these atoms are free and in the end they are bound in clusters. Denoting by N the number density of free metal atoms, by N_{cl} the number density of clusters, by N_b the number density of atoms bound in clusters, and by N_a the number density of atoms in the buffer gas, we obtain on the basis of the scheme of processes (3.8) the following set of balance equations for these number densities and for a cluster size n (the number of atoms per cluster) [137, 139, 142, 146]:

$$\frac{dN_b}{dt} = -\frac{dN}{dt} = \int Nk_0 n^{2/3} f_n \, dn + KN^2 N_a , \qquad \frac{dN_{cl}}{dt} = KN^2 N_a . \tag{3.11}$$

Here, f_n is the size distribution function of the clusters, i.e., the number density of clusters consisting of n atoms, and the normalization conditions for this distribution function are given by

$$N_{cl} = \int f_n \, dn , \qquad N_b = \int n f_n \, dn .$$

Note that in the above balance equations (3.11) we ignored cluster evaporation processes. This corresponds to a relatively small temperature or large current cluster size compared to the critical one.

We consider cluster growth under the condition $G \gg 1$, when the three-body process of scheme (3.8) is slow and delays the overall process. Then, forming diatomic molecules are the condensation nuclei, and this is taken into account in the above balance equations (3.11). Next, the second term on the right-hand side of the first balance equation (3.11) is small compared to the first one. Indeed, the ratio between the first and second terms on the right-hand side of the first balance equation is on the order of $Gn^{2/3}$, and since $G \gg 1$ and the current cluster size $n \gg 1$, one can neglect the second term in the first balance equation. As a result, we arrive at the balance equation in the form

$$\frac{dN_b}{dt} = Nk_0 \int n^{2/3} f_n \, dn . \tag{3.12}$$

One can solve this balance equation taking for simplicity $N(t) = \text{const}$ until N_b reaches the value N. Then the cluster growth time τ_{cl}, i.e., the time of transformation of a gas of free atoms into a gas of clusters, is defined by

$$N_b(\tau_{cl}) = N . \tag{3.13}$$

Let us determine the size distribution function f_n of clusters, considering an individual cluster whose size $n(t)$ satisfies the equation

$$\frac{dn}{dt} = k_0 n^{2/3} N , \tag{3.14}$$

where t is the time after the formation of a dimer which is a condensation nucleus for a given cluster. After the lapse of time t the cluster size becomes equal to

$$n = \left(\frac{Nk_0 t}{3}\right)^3 .$$

Taking into account that $f_n \, dn$, the number density of clusters with sizes between n and $n + dn$, is proportional to the time interval dt during which diatomic metal molecules are formed, i.e., $f_n \, dn \sim dt$, on the basis of the above formulas we obtain for the cluster size distribution function:

$$f_n = \frac{C}{n^{2/3}} , \qquad n < n_{max} . \tag{3.15}$$

Here, C is a normalization constant, n_{max} is the maximum cluster size at a given instant of time, and $f_n = 0$ for $n > n_{max}$. Formula (3.15) may be obtained directly from the kinetic equation for the distribution function f_n, ignoring the cluster evaporation processes [139]:

$$\frac{\partial f_n}{\partial t} = -\frac{\partial}{\partial n}\left(Nk_0 n^{2/3} f_n\right) ,$$

and formula (3.15) is the solution to this equation.

Let us determine now the parameters describing the kinetics of cluster growth. On the basis of the normalization relations and expression (3.15) for the size distribution function of clusters we have at the end of the nucleation process [142, 146] that

$$C = \frac{4N}{3n_{max}^{4/3}} , \quad N_{cl} = 3Cn_{max}^{1/3} = \frac{4N}{n_{max}} , \quad \overline{n} = \frac{n_{max}}{4} . \tag{3.16}$$

Here, $\overline{n}$ is the average cluster size. The maximum cluster size at the end of the nucleation process is determined from the solution of the balance equation for a size of an individual cluster whose diatomic molecule is formed at $t = 0$ and is equal to

$$n_{\max}(\tau_{\text{cl}}) = \left(\frac{Nk_0\tau_{\text{cl}}}{3}\right)^3 = \left(\frac{\xi}{3}\right)^3, \tag{3.17}$$

with $\xi = Nk_0\tau_{\text{cl}}$. Integrating the balance equations (3.12) over time gives

$$N_{\text{cl}} = KN^2N_{\text{a}}\tau_{\text{cl}} = N\,\frac{\xi}{G}\,, \qquad N_{\text{b}}(\tau_{\text{cl}}) = \int Nk_0Cn_{\max}\,\text{d}t = \frac{1}{4}\,\xi Cn_{\max} = N\,. \tag{3.18}$$

Such a simplified scheme of the nucleation of an atomic vapor allows us to express the cluster parameters at the end of the nucleation process through the parameter (3.10). Indeed, comparing the expressions for N_{cl} from formulas (3.16) and (3.18), we find [142]

$$n_{\max} = \frac{4G}{\xi}\,, \tag{3.19}$$

and on the basis of formula (3.17) we obtain the expression for the reduced nucleation time

$$\xi = 3\left(\frac{4}{3}\,G\right)^{1/4} = 3.2\,G^{1/4}\,, \tag{3.20}$$

which is large, since $G \gg 1$. This also leads to large cluster sizes at the end of nucleation process (3.8) [142, 146, 147]:

$$n_{\max} = 1.2\,G^{3/4}\,, \qquad \overline{n} = 0.31G^{3/4}\,, \qquad N_{\text{cl}} = 3.2\,NG^{-3/4}\,. \tag{3.21}$$

Correspondingly, the total time of nucleation is equal to [142]

$$\tau_{\text{cl}} = \frac{3.2\,G^{1/4}}{Nk_0}\,, \tag{3.22}$$

and N is the initial number density of nucleating atoms which will become bound at the end of the nucleation process.

Thus, within the framework of a simple scheme (3.8) for transformation of an atomic vapor into a gas of clusters we found the dependence of the output parameters for forming clusters on the parameters of this process [142]. Though we set such initial conditions that all the nucleating atoms are free at the beginning, the above results may also be used as estimates in the case when free atoms are added to the nucleating system during a certain time. Note that, under certain conditions, additional processes liable for the dynamics of a gas or the chemistry of gas components may also be added to this scheme. Though we considered the formation of pure metal clusters from their atoms, generation of some compounds of these metals is also possible. For example, a small oxygen admixture can give clusters of metal oxides, or the presence of nitrogen atoms can lead to the formation of clusters of metal nitrides.

3.3 Processes near a cathode involving fast sputtered atoms

Sputtered metal atoms can return to the cathode after multiple scattering from buffer gas atoms, and we now consider processes of the relaxation of fast atoms and their transport in a space. We evaluated above a time of relaxation resulting in isotropization of atomic motion, and the rate of this process was given by formula (3.5). When atomic motion becomes isotropic, its energy does not vary significantly compared to the initial kinetic energy of a sputtered atom, so that in the course of thermalization of metal atoms in collisions with buffer gas atoms, and a thermalization time τ_{T} is large compared to an isotropization time τ_{P}. We now determine the relaxation time τ_{E} in which the kinetic energy of a fast atom varies from E_0 to E due to collisions with thermal buffer gas atoms.

In this consideration we assume $E \gg T$ — that is, the atomic kinetic energy E exceeds significantly the typical thermal energy T. Hence, one can consider a buffer gas atom to be motionless before it collides with a fast metal atom. Expressing the velocity $\mathbf{v}$ of a fast atom through the relative velocity $\mathbf{g}$ of colliding atoms and the center-of-mass velocity $\mathbf{V}$ as

$$\mathbf{v} = \mathbf{V} + \frac{M}{M+m}\,\mathbf{g}\,,$$

we obtain for the energy variation as a result of atomic collisions:

$$\Delta E = \frac{Mm}{M+m}\,\mathbf{V}(\mathbf{g}-\mathbf{g}') = \mu Vg(1-\cos\vartheta) = 2\,\frac{\mu}{M+m}\,E(1-\cos\vartheta)\,.$$

Here, M, m are the masses of buffer gas and metal atoms, respectively, and ϑ is the scattering angle in the center-of-mass system. Hence, the rate of the energy variation for a fast metal atom is given by

$$\frac{\text{d}E}{\text{d}t} = 2\,\frac{\mu}{M+m}\,EvN_{\text{a}}\sigma^*(v)\,, \tag{3.23}$$

where E is the kinetic energy of a test metal atom, and $\sigma^*(v) = \int(1-\cos\vartheta)\,\text{d}\sigma$ is the transport cross section for the scattering of a fast metal atom from a motionless buffer gas atom. From this we obtain a time τ_{E} of energy variation from E_0 to E:

$$\tau_{\text{E}} = \int_E^{E_0}\frac{\text{d}E}{2EvN_{\text{a}}\sigma^*(v)}\,\frac{M+m}{\mu}\,. \tag{3.24}$$

Neglecting the energy dependence for the cross section of atomic collisions, we obtain the following relationship

$$\tau_{\text{E}} = \frac{4(M+m)^2}{Mm}\,\frac{1}{N_{\text{a}}\sigma^*(v)}\left(\frac{1}{v}-\frac{1}{v_0}\right), \tag{3.25}$$

where v_0 is the initial velocity of a fast atom, and v is its final velocity which is assumed to be large compared to the thermal velocity. The ratio of the energy relaxation time (3.25) to the momentum relaxation time (3.5) becomes equal to

$$\frac{\tau_{\text{E}}}{\tau_{\text{P}}} = \frac{4(M+m)}{m}\left(\frac{v_0}{v}-1\right), \tag{3.26}$$

so that thermalization of fast atoms lasts significantly longer than isotropization for fast atom motion.

Let us evaluate a typical time $\tau_{\rm cat}$ of returning sputtered atoms to the cathode as a result of their motion in a buffer gas. We assume the following inequality between an average energy E_0 of sputtered atoms, the binding energy $\varepsilon_{\rm b}$ of metal atoms inside the cathode, and a thermal energy T of thermalized atoms:

$$E_0 \gg \varepsilon_{\rm b} \gg T\,. \qquad (3.27)$$

Note that if a fast atom collides with the cathode, its attachment to the cathode is absent, and hence at the first stage of the thermalization process metal atoms do not attach to the cathode and the occupied region increases. We first find the average distance at which an atom is displaced until its energy does not exceed $\varepsilon_{\rm b}$. This distance is determined from the diffusion equation

$$\frac{\partial P}{\partial t} = D(t)\,\frac{\partial^2 P}{\partial x^2}\,, \qquad (3.28)$$

and from this equation it follows that the average distance at which an atom travels is given by

$$\overline{\Delta x^2} = 2\int D(t)\,{\rm d}t = 2\int D(E)\,\frac{{\rm d}E}{{\rm d}E/{\rm d}t} = \int D(E)\,\frac{(M+m)^2}{mM}\,\frac{\lambda(E)\,{\rm d}E}{E v}\,, \qquad (3.29)$$

with

$$\lambda(E) = \frac{1}{N_{\rm a}\sigma^*(E)}\,,$$

where $N_{\rm a}$ is the number density of buffer gas atoms, and we took into account that the diffusion coefficient of a metal atom in a buffer gas changes with the variation in the atom energy.

In evaluating the diffusion coefficient of fast atoms in a buffer gas, when the motion of metal atoms is isotropic, we use the limiting expressions for the diffusion coefficient [156]. Indeed, in the case $m \ll M$, the diffusion coefficient equals

$$D = \left\langle \frac{v^2}{3\nu} \right\rangle,$$

where the collision rate ν is given by

$$\nu(E) = \frac{v}{\lambda(E)}\,,$$

and the angle brackets mean averaging over the atom velocities. In the other limiting case $m \gg M$, we have

$$D = \frac{\langle v_x^2\rangle}{\langle \nu\rangle}\,.$$

Taking the energy distribution function $f(\varepsilon)$ of fast atoms to be $N\delta(\varepsilon - E)$, we obtain the following expression for the diffusion coefficient of fast metal atoms:

$$D(E) = \frac{v^2}{3\nu(v)} = \frac{v\lambda(E)}{3}\,.$$

This gives for the average distance of fast atom propagation:

$$\overline{\Delta x^2} = \frac{(m+M)^2}{3mM}\int \frac{\lambda^2(E)\,{\rm d}E}{E}\,. \qquad (3.30)$$

Let us take the dependence of the interaction potential $U(R)$ on the distance R between metal and buffer gas atoms in the range $U \sim E$ as $U(R) \sim R^{-k}$; we then have $\sigma^*(E) \sim E^{-2/k}$, $\lambda(E) \sim E^{2/k}$. For the size of the spreading region Δx for fast metal atoms, when their energy varies from the initial value E_0 to the binding energy $\varepsilon_{\rm b}$ for atoms in a bulk metal, this gives

$$\overline{\Delta x^2} = \frac{(M+m)^2}{3mM}\int_{\varepsilon_{\rm b}}^{E_0} \frac{\lambda^2(E)\,{\rm d}E}{E} = \lambda^2(E_0)\,\frac{k}{3}\,\frac{(M+m)^2}{mM}\left[1 - \left(\frac{\varepsilon_{\rm b}}{E_0}\right)^{k/4}\right]. \qquad (3.31)$$

The quantity Δx characterizes the size of the region that is occupied by a sputtered atom until it cannot attach to the cathode, and formula (3.31) includes an uncertain quantity $\varepsilon_{\rm b}$. In order to find the sensitivity to this quantity and, correspondingly, the accuracy of the above formula, we apply it to experimental conditions [143] when silver atoms are sputtered in a buffer argon gas. We take the value $k = 8$, as for the interaction of two argon atoms, and under experimental conditions the average energy of sputtered silver atoms reaches $E_0 = 19$ eV. Taking $\varepsilon_{\rm b} = 2$ eV, we obtain $(\overline{\Delta x^2})^{1/2} = 3.0\,\lambda(E_0)$, and for $\varepsilon_{\rm b} = 4$ eV, we have $(\overline{\Delta x^2})^{1/2} = 2.7\,\lambda(E_0)$. An important conclusion resulting from formula (3.31) is that the expansion of a region occupied by relaxing atoms is independent of the final atomic energy. This means that a sputtered atom attaches to the cathode after thermalization, so that

$$\tau_{\rm cat} > \tau_{\rm E}\,,$$

where the final atomic energy E corresponds to the thermal energy.

Thus, at the stage of thermalization, a sputtered atom propagates through a distance $\overline{\Delta x} = (\overline{\Delta x^2})^{1/2}$:

$$\overline{\Delta x} = \lambda(E_0)\sqrt{\frac{k}{3}\,\frac{(M+m)^2}{mM}}\,, \qquad (3.32)$$

and then a thermal metal atom is spread over the space where it can reach the cathode. A typical time of atom attachment to the cathode in the absence of nucleation processes equals

$$\tau_{\rm cat} = \frac{\overline{\Delta x^2}}{2D_{\rm T}}\,, \qquad (3.33)$$

where $D_{\rm T}$ is the diffusion coefficient of thermal metal atoms in a buffer gas. Note that the diffusion cross section of scattering of a thermal metal atom from a buffer gas atom depends on the sort of metal for a given buffer gas. Then, based on experimental data [138] for diffusion coefficients of metal atoms in a buffer gas, one can find this quantity for various metal atoms. In particular, we obtain from Ref. [138] the average gas-kinetic cross section $\sigma_{\rm gas} = (4.8 \pm 0.5)\times 10^{-15}$ cm^2 for metal atoms in argon. From this we find the diffusion coefficient of a titanium atom in argon: $D_{\rm T} = 0.14 \pm 0.01$ cm^2 s^{-1} at temperature $T = 300$ K, and also find the same value for silver atoms in argon: $D_{\rm T} = 0.12 \pm 0.01$ cm^2 s^{-1}. These values are reduced to

the normal number density of buffer gas atoms $N_a = 2.69 \times 10^{19}$ cm^{-3}. For a reduced time of attachment of a titanium atom to the cathode in argon under experimental conditions according to formula (3.33) we get $N\tau_{cat} = 1.6 \times 10^{12}$ cm^{-3} s, and for silver atoms this value is $N\tau_{cat} = 2.0 \times 10^{12}$ cm^{-3} s, if the silver atoms are formed in magnetron discharge under the above experimental conditions [143]. Next, under experimental conditions [35] for titanium atoms the dimension of the region where sputtered titanium atoms are spread in argon is $\Delta x \sim 0.8$ cm.

One can compare the attachment time τ_{cat} with the relaxation time τ_T of a sputtered metal atom up to thermal energies, which is given by formula (3.25) in the limit $E_0 \gg T$:

$$\tau_T = \frac{4(M+m)^2}{mM(1+4/k)} \frac{1}{N_a \sigma_{gas}(E_0)} \sqrt{\frac{\pi m}{8T}}, \tag{3.34}$$

where the transport cross section σ_{gas} is taken at the initial energy of a sputtered atom, and the parameter of an atomic interaction potential is taken to be $k = 8$. From this we obtain under experimental conditions [35] for the relaxation of titanium atoms in argon: $N\tau_T = 2.0 \times 10^{11}$ cm^{-3} s, and for silver atoms in argon one finds $N\tau_{cat} = 1.7 \times 10^{11}$ cm^{-3} s. As is seen, under these conditions the thermalization time of sputtered atoms is by one order of magnitude less than the typical time of atom attachment to the cathode.

Note that since $\overline{\Delta x} \sim \lambda \sim 1/N_a$ and $D_T \sim 1/N_a$, from formula (3.33) it follows that the typical time of atom attachment to the cathode τ_{cat} is inversely proportional to the number density N_a of buffer gas atoms. Therefore, if a region near the cathode is heated due to relaxation processes involving fast metal atoms, the attachment rate of metal atoms to the cathode increases at a constant pressure in the magnetron chamber.

3.4 Cluster generation in a magnetron plasma

When a sputtered metal atom is thermalized in a buffer gas at a large distance from the cathode compared to the mean free path of a thermal atom, it can attach to forming clusters or return to the cathode and attach to it. In order to find the probability of each event, it is necessary to compare the rates of these processes. Formula (3.33) gives a typical time τ_{cat} of attachment of a sputtered atom to the cathode, and the typical time of nucleation τ_{cl} is defined by formula (3.22). Though the above model of nucleation relates to a way of insertion of free metal atoms in the nucleation region that does not take place in reality, this model gives a correct estimate for nucleation parameters, and we will rely on it. Correspondingly, the criterion for a sputtered atom not to return to the cathode, but be a constituent of a cluster, has the form

$$\tau_{cl} \ll \tau_{cat}. \tag{3.35}$$

Based on formula (3.22) for the time of cluster growth, one can rewrite this criterion in the following form for the number density of nucleating atoms N in a region where the cluster growth proceeds:

$$N \gg \frac{3.2G^{1/4}}{k_0 \tau_{cat}}. \tag{3.36}$$

As follows from the above criteria, the process of cluster formation has a threshold character and can be realized at not a small number density of braking sputtered atoms and, correspondingly, for the specific power of magnetron discharge. Since a typical time τ_{cat} of return of a sputtered atom to the cathode according to formula (3.33) is $\tau_{cat} \sim 1/N_a$, this criterion (3.36) requires that the concentration N/N_a of free metal atoms near the cathode exceed a certain critical value.

The character of equilibrium in this case is similar to that considered above for applications where a plate is inserted into a magnetron discharge at some distance from the cathode [115, 116, 130], so that sputtered atoms can deposit on this target. Then the final state of sputtered atoms can lead to their attachment to the cathode or plate, depending on the distance between the plate and cathode. In the case of generation of clusters, we also have two channels for the final state of sputtered atoms, so that they can return to the cathode or attach to clusters, and then clusters leave the nucleation region with a buffer gas flow. We considered above the character of absorption of sputtered atoms by the cathode that included the stage of thermalization of fast metal atoms in a buffer gas, and after this the stage of diffusion motion of thermal metal atoms to the cathode. As a result, thermal atoms can attach to the cathode. The other channel of evolution of metal atoms relates to their attachment to clusters. The formation and growth of clusters from metal atoms proceeds according to scheme (3.8), as earlier, but we now use other boundary conditions and find for them the size distribution function of clusters.

We will take into account that new free atoms are added to the system continuously, and the clusters being formed are carried away by a buffer gas flow. This character of cluster growth is similar to the case where metal clusters are formed from a metal compound that, in the form of molecules, is inserted into a buffer gas and thermal metal molecules decay in collisions with buffer gas atoms. Like this case, metal atoms are added to the system continuously, and the number density of free metal atoms is the problem parameter. We now represent the space distribution $N(x)$ of free metal atoms in the form

$$N(x) = N_0 \exp\left(-\frac{x}{\lambda}\right),$$

where x is a distance from the cathode, and the parameter λ follows from the balance equations. According to scheme (3.8) of the nucleation process, its long stage is the formation of metal diatomic molecules which are nuclei of condensation, and, correspondingly, the distribution function $f_n(x)$ of clusters consisting of n atoms and located at a distance x from the cathode is uniquely determined by the number density of diatomic metal molecules formed at a distance x' from the cathode. Therefore, from the second balance equation (3.11) we have for the size distribution function:

$$f_n\, dn = KN_a N^2\, dt = N_{cl} \exp\left(-2\,\frac{x'}{\lambda}\right) dx', \tag{3.37}$$

and the total number density of clusters N_{cl} at large distances from the cathode is given by

$$N_{cl} = \int f_n\, dn = \frac{KN_a N_0^2 \lambda}{2u}, \tag{3.38}$$

where u is the velocity of the buffer gas flow.

The size of clusters at a point x from the cathode that are formed at point x' follows from the balance equation (3.14)

that gives

$$n^{1/3}(x,x') = \frac{k_0 N_0}{3}\int_{x'}^{x} \exp\left(-\frac{x}{\lambda}\right) dt = \frac{k_0 N_0 \lambda}{3u}\left[\exp\left(-\frac{x'}{\lambda}\right) - \exp\left(-\frac{x}{\lambda}\right)\right].$$

From this we find

$$n(x,x') = n_{\max}\left[\exp\left(-\frac{x'}{\lambda}\right) - \exp\left(-\frac{x}{\lambda}\right)\right]^3, \qquad (3.39)$$

where the maximum cluster size $n_{\max}$ is given by

$$n_{\max} = \left(\frac{k_0 N_0 \lambda}{3u}\right)^3. \qquad (3.40)$$

The size distribution function (3.37) and the size of the clusters (3.39) depend on the point of cluster formation, and observation gives the perfect information about the size distribution of clusters at each distance from the cathode. In particular, from this it follows that far from the cathode the average cluster size equals

$$\overline{n} = \frac{1}{N_{\text{cl}}}\int_0^{n_{\max}} f_n n \, dn = \frac{2}{5} n_{\max}, \qquad (3.41)$$

and the rate ν of atom attachment to clusters in accordance with the second process in Eqn (3.8) is given by

$$\nu = \int k_0 n^{2/3} f_n \, dn = \frac{k_0 N_{\text{cl}} n_{\max}^{2/3}}{2}\left[1 - \exp\left(-\frac{x}{\lambda}\right)\right]^3\left[1 - \frac{1}{3}\exp\left(-\frac{x}{\lambda}\right)\right]^3.$$

Far from the cathode, this gives

$$\nu = \frac{5}{4}\frac{N_{\text{b}} k_0}{n_{\max}^{1/3}} = 0.92\,\frac{N_{\text{b}} k_0}{\overline{n}^{1/3}}, \qquad (3.42)$$

where the number density of bound atoms is $N_{\text{b}} = N_{\text{cl}}\overline{n}$.

Let us analyze the experimental results [35] from the standpoint of the possibility of cluster formation. In this experiment, titanium clusters were formed in argon as a buffer gas under a pressure of 0.1 mbar and a temperature of 200 K that corresponds to the atomic number density $N_{\text{a}} = 4 \times 10^{15}$ cm^{-3}. At this temperature, we have for the rate constants of processes involving titanium clusters: $k_0 = 2.6 \times 10^{-11}$ cm^3 s^{-1}, $K = 2.5 \times 10^{-33}$ cm^6 s^{-1}, which gives $G = 3 \times 10^6$ and $G^{1/4} = 40$. According to formula (3.21) we have for the average cluster size at the end of the nucleation process: $\overline{n} = 2 \times 10^4$, which corresponds to experimental data under conditions when the subsequent coagulation of clusters is absent. This size corresponds to the diffusion coefficient $D_n = 5$ cm^2 s^{-1} of clusters in argon, and because the drift velocity of argon is $u = 15$ cm s^{-1}, a typical dimension of the nucleation region, if it is established due to the motion of clusters, amounts to $l \sim D_n/u \sim 0.3$ cm. The typical dwell time of clusters in this region is $\tau \sim D_n/u^2 \sim 0.02$ s. Since $l \ll \Delta x \sim 0.8$ cm, the size of the nucleation region is determined by a travel of free metal atoms in the space, rather than the cluster diffusion.

We can use other typical parameters of the experiment [35] under consideration. The voltage is 225 V, the current is 0.5 A, the cathode radius is 5 cm, the sputtering region occupies 30% of the cathode surface (Fig. 2c), and the metal atom yield is $\zeta = 0.37$ [115, 116]. From this we obtain the value of the flux of metal atoms from the cathode: $j = 6 \times 10^{16}$ cm^{-2} s^{-1}. We assume for simplicity that under these conditions one-half of the thermal metal atoms returns to the cathode and the other half of the metal atoms is transformed into clusters. Then the flux of bound atoms under these conditions is $j_{\text{b}} = 3 \times 10^{16}$ cm^{-2} s^{-1}, which gives for the number density of bound atoms $N_{\text{b}} = j_{\text{b}}/u = 2 \times 10^{15}$ cm^{-3}. From above values using formula (3.42) one can find the typical time of attachment for metal atoms to clusters in a nucleation region:

$$\tau_{\text{cl}} = \frac{1}{\nu} \sim 6 \times 10^{-4} \text{ s},$$

which is comparable to the time of an atom returning to the cathode. Note that these evaluations are based on the assumption that the temperature of the nucleation region coincides with the cathode temperature, whereas a buffer gas is heated in this region due to relaxation and nucleation processes. Hence, the above evaluations may be considered to be estimations.

If a remarkable part of free metal atoms is transformed into clusters, the depth λ of penetration of metal atoms into the region occupied by the clusters is comparable to the distance Δx that fast atoms travel from the cathode, i.e., $\lambda \sim \Delta x$. This takes place when the typical time τ_{cl} of atom attachment to clusters exceeds or is comparable to the typical time τ_{cat} of an atom travelling to the cathode. Next, under experimental conditions [35] the number density of free metal atoms near the cathode is estimated as

$$N \sim \frac{j}{\Delta x}\left(\frac{1}{\tau_{\text{cl}}} + \frac{1}{\tau_{\text{cat}}}\right) \sim 2 \times 10^{13} \text{ cm}^{-3}.$$

As is seen, the number density of bound metal atoms under experimental conditions, $N_{\text{b}} \sim 2 \times 10^{15}$ cm^{-3}, is comparable to the number density of buffer gas atoms, $N_{\text{a}} = 4 \times 10^{15}$ cm^{-3}, and exceeds significantly the number density of free metal atoms, $N \sim 2 \times 10^{13}$ cm^{-3}, in the cathode region, whose concentration in the cathode region is approximately 2% of N_{b}. Note that according to data in Fig. 14 [21] the number density of free atoms far from the

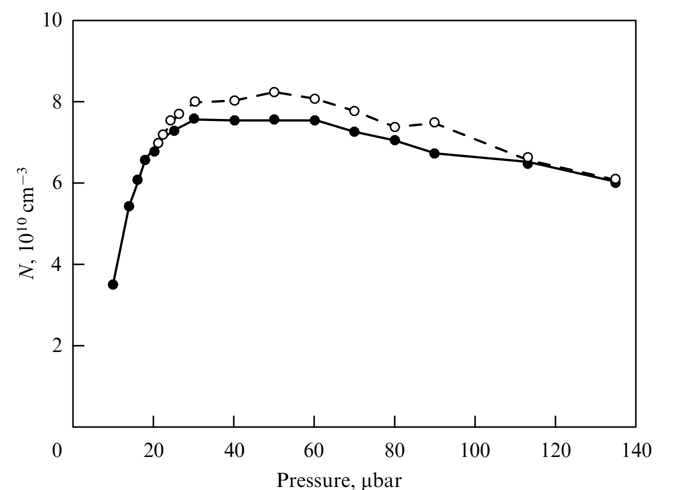

Figure 14. The number density of Al atoms as a function of argon pressure for two flow velocities: (●) 15 and (○) 40 stand. cm^3 min^{-1} (stand. cm^3 min^{-1} = 4.5×10^{18} s^{-1}). The magnetron discharge power is 100 W, and the distance from the cathode is 5.5 cm.

cathode is several orders of magnitude less than that near the cathode. Moreover, within the framework of this scheme, free atoms are absent far from the cathode. Evidently, they are formed there in collisions with electrons, and a typical electron energy (see Fig. 10) allows detachment of atoms from a cluster in such collisions.

This analysis of experimental conditions allows us to describe the general character of cluster formation in a magnetron plasma. Sputtered atoms move a large distance $\overline{\Delta x}$ from the cathode in comparison with the mean free path λ_T of thermalized atoms in a buffer gas under a given pressure and flow velocity. Sputtered atoms are thermalized at large distances from the cathode and then can return to the cathode or form clusters, so that these probabilities depend on the number density N of free metal atoms. Let us denote by N_0 such a number density of free atoms in the thermalization region at which the probabilities of a given atom attaching to clusters and returning to the cathode are equal. Then, if the number density N of forming free metal atoms satisfies the condition $N \gg N_0$, most of the forming atoms attach to clusters; in the opposite limiting case, free forming metal atoms return to the cathode. Evidently, the number density of forming free atoms is proportional to the discharge power and also increases as the discharge voltage increases. Therefore, the cluster regime of the evolution of the magnetron plasma is realized at high powers and voltages of magnetron discharge.

Let us analyze the character of nucleation for $N < N_0$ in terms of the typical times τ_{cl} of an atom attaching to clusters and its returning to the cathode, τ_{cat}. In accordance with the above analysis, the number of forming clusters is proportional to τ_{cat}/τ_{cl}, and the typical cluster size is proportional to $(\tau_{cat}/\tau_{cl})^3$, i.e., the number density N_b of bound atoms is proportional to $(\tau_{cat}/\tau_{cl})^4$ in this case. If $\tau_{cat}/\tau_{cl} = N/N_0$, we get the portion of bound atoms decreasing in the case of small power of magnetron discharge as $(N/N_0)^4$. From this it follows that the formation of clusters in a magnetron plasma has a threshold character with respect to the discharge power.

As a demonstration of an example when clusters are not formed in a magnetron plasma, we give the aluminium case that was analyzed in the experiment [21]. At the discharge power in a range 10–100 W, the number density of aluminium atoms reaches $\sim 10^{11}$ cm^3 far from the cathode. If we suppose that the destruction of aluminium atoms in this region results from their travelling to the walls by diffusion in a buffer gas and the distance to the cathode from the thermalization region is one order of magnitude larger than that for the walls, we obtain the maximum number density of free metal atoms in the thermalization region, $N \sim 10^{13}$ cm^{-3}. Thus, the cluster regime of a magnetron discharge with a buffer gas flow requires specific conditions. Note that free metal atoms are absent far from the cathode in the cluster regime of the magnetron discharge, and observation of free atoms with a remarkable number density in this case testifies to the absence of clusters.

Thus, the fate of sputtered atoms in the cathode region depends on the flux of these atoms, and they either attach to clusters or return to the cathode. In the above analysis, we kept the experimental conditions from Ref. [35]. But in reality, the kinetic and transport parameters of metal atoms, such as the reduced constant k_0 of attachment to clusters, the gas-kinetic cross section σ_{gas} for a given buffer gas, and the diffusion coefficient of thermal metal atoms in this gas do not depend strongly on the sort of metal. Therefore, accounting for the roughness of the above estimates, one can disseminate them for other sorts of metal atoms. In particular, from this it follows that the parameter $N_0 \sim 2 \times 10^{13}$ cm^{-3}.

3.5 Heat processes in a magnetron plasma

Analyzing the kinetic and transport properties of the magnetron plasma, we took implicitly the temperature of a buffer gas in the cathode region to be equal to the cathode temperature. Indeed, the cathode is cooled by flowing water, and the magnetron chamber is cooled by liquid nitrogen. Nevertheless, though the main power of magnetron discharge is consumed at the cathode due to fast ions, a part of this power is consumed in the plasma in collisions of fast metal atoms with buffer gas atoms and as a result of their nucleation. Below, we will estimate the heating of a buffer gas near the cathode as a result of the thermalization and nucleation of sputtered atoms.

Let us consider the experimental conditions [35] for a titanium magnetron plasma if the discharge current of 0.5 A occupies 30% of the area of the cathode whose radius is 5 cm. We take the metal atom yield as a result of bombardment of the cathode by argon ions to be $\zeta = 0.37$ [115, 116], and the average energy of sputtered atoms to be 20 eV. This corresponds to the specific power that is scattered in a buffer gas near the cathode of approximately 0.3 W cm^{-2}, which is equal to the heat flux that is given by

$$q \approx \kappa \, \frac{\Delta T}{\Delta x} \, ,$$

where κ is the thermal conductivity coefficient of the buffer gas, ΔT is the temperature increase in the cathode region due to sputtered atoms, and Δx is the cathode region dimension. Taking $\kappa \sim 2 \times 10^{-4}$ W cm^{-2} K^{-1}, and $\Delta x \sim 0.8$ cm, we obtain $\Delta T \sim 10^3$ K. This is small compared to the binding energy of metal atoms in clusters and, therefore, such a heating will not affect nucleation processes. Nevertheless, heating of the cathode region may influence the parameters of the cathode processes and change the yield parameters, including the probability of a sputtered atom attaching to clusters or returning to the cathode.

Along with the heating of a buffer gas, clusters are also heated as a result of the nucleation process and in collisions with buffer gas atoms and plasma electrons. In considering the heat balance of clusters, we note that the temperature of clusters in the magnetron chamber is significantly higher than the gas temperature T_a and lower than the electron temperature T_e (we assume $T_e \gg T_a$), if the cluster temperature T_{cl} results from cluster collisions with atoms and electrons. Let us find the cluster temperature within the framework of a simple model of the heat balance [137, 149], assuming that the exchange of energy between colliding particles proceeds only upon their contact, and a scattered electron or atom has an average energy $3T_{cl}/2$. This means that an atom obtains the energy $3/2(T_{cl} - T_a)$ from the cluster on average, and an electron transfers to the cluster the energy $3/2(T_e - T_{cl})$ on average after each collision. Then, the power which a cluster takes from electrons is $3/2(T_e - T_{cl})v_e N_e \sigma_e$, where v_e is the average electron velocity, N_e is the number density of electrons, and σ_e is the cross section of electron–cluster collisions. The power which atoms obtain from the cluster is evaluated as $3/2(T_{cl} - T)v_a N_a \sigma_a$, where v_a is the average velocity of atoms, N_a is the number density of atoms, and σ_a is the cross section of atomic collisions with the clusters. For a neutral cluster we have within the framework of the liquid

drop model for a cluster: $\sigma_e = \sigma_a = \pi r^2$, where r is the cluster radius. The balance of electron – cluster and atom – cluster collisions for the cluster temperature [137, 149] gives

$$T_{cl} = \frac{T_a + \zeta T_e}{1 + \zeta}, \quad \zeta = \sqrt{\frac{T_e M}{T_a m_e}} \frac{N_e}{N_a}, \quad (3.43)$$

where m_e and M are the electron and atom masses, respectively. If a cluster is charged and its charge equals Z, the parameter ζ in formula (3.43) is given by [137, 149]

$$\zeta = \sqrt{\frac{T_e M}{T_a m_e}} \left(1 + \frac{Ze^2}{rT_e}\right) \frac{N_e}{N_a}. \quad (3.44)$$

These formulas also give the temperature of a negatively charged cluster and correspond to a large mean free path λ of atoms in comparison with the cluster radius r.

We now consider the heat balance of clusters, which takes place in the nucleation region of magnetron discharge. A released energy results from the attachment of free metal atoms to clusters, and subsequently this energy is transferred to buffer gas atoms. Correspondingly, the heat balance equation takes the following form in this case [35]:

$$\frac{3}{2}(T_{cl} - T_a)N_a = \Delta\varepsilon N, \quad (3.45)$$

where $\Delta\varepsilon$ is the binding energy of a metal atom in the cluster, and N is the number density of free metal atoms. Under typical experimental conditions, we obtain from this in the cluster regime of magnetron discharge a cluster heating $(T_{cl} - T_a)$ of a few hundred degrees.† We then assume that cluster heating proceeds due to the aggregation process and its cooling results from collisions with argon atoms. Supposing the change in the energy of a buffer gas atom results from collisions with the cluster surface, we obtain the heat balance equation

$$\frac{3}{2}(T - T_a)N_a = \Delta\varepsilon N, \quad (3.46)$$

where T is the cluster temperature, T_a is the gas temperature, and $\Delta\varepsilon$ is the average binding energy of a metal atom in the cluster. From this we get $\Delta T = T - T_a$ being several hundred degrees kelvin under typical conditions. Hence, a decrease in the buffer gas temperature by a hundred degrees on the basis of its cooling by liquid nitrogen does not influence, in principle, the cluster temperature or the nucleation process.

4. Transport of clusters in a gas flow

4.1 Flow of a buffer gas through the magnetron chamber

The gas pressure at the entry and exit from the magnetron chamber is different, which creates a buffer gas flow through the magnetron chamber. From the standpoint of the flow of a buffer gas with clusters, one can divide the flow regions into three parts. The first one is located near the cathode, where clusters are formed and are mixed with the flow. The second region corresponds to a quiet flow with a small velocity compared to the speed of sound. The third region is located near the chamber exit, where the flow is accelerated and its cross section decreases. Near the orifice, the flow velocity is of the order of the speed of sound. Below, we consider these regions separately and the flow as a whole.

† Three sentences that follow were added by the authors in proof reading. (*Editor's note.*)

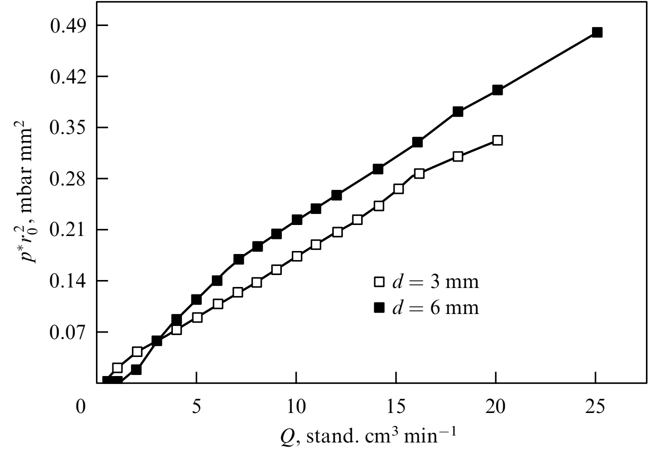

Figure 15. The reduced argon pressure inside the magnetron chamber as a function of the argon rate Q at two orifice diameters [35, 142].

The measurable quantities characterizing a buffer gas flow through a chamber are the flow rate Q and the gas pressure p inside the chamber. For a round orifice of radius r_0 for the gas exit, one can connect the parameters of the flow by the relation

$$Q = \pi r_0^2 N u. \quad (4.1)$$

Here, r_0 is the orifice radius, N is the number density of atoms inside the chamber, which is connected with the gas pressure p as $N = p/T$ (T is the gas temperature), and the flow velocity u near the orifice is on the order of the speed of sound u_0. Figure 15 gives the reduced pressure of a buffer gas, which determines the velocity ratio u/u_0 that does not practically depend on other parameters for the stationary regime of a gas flow. Statistical averaging gives for all measurements: $u/u_0 = 0.91 \pm 0.06$ for an orifice diameter $d = 3$ mm, $u/u_0 = 0.76 \pm 0.06$ for an orifice diameter $d = 6$ mm, and $u/u_0 = 0.84 \pm 0.10$ if we account for all the measurements. From this we take

$$u = 0.8\, u_0, \quad (4.2)$$

and the accuracy of this approximation is better than 15%.

We note a weak friction of the buffer gas with the walls at a laminar flow. Indeed, in considering the gas flow through the magnetron chamber to be a motion inside a cylinder tube, we obtain for the pressure gradient along the flow due to wall friction that is given by Poiselle's formula [148, 152]

$$\frac{dp}{dx} = \frac{8\nu Q}{\pi R^4}. \quad (4.3)$$

In particular, under the experimental conditions [35] by which we are guided, when argon of a temperature $T = 200$ K is moving with a velocity of 15 cm s^{-1} through a magnetron chamber of radius $R = 5$ cm, the dynamic viscosity of the flowing gas is $\nu = 600$ cm^2 s^{-1}, and the pressure variation in the magnetron chamber ($L = 15$ cm) amounts to 1×10^{-8} bar, so that the pressure variation in the magnetron chamber is negligibly small, since $\Delta p/p \sim 10^{-4}$.

4.2 Equilibrium of a buffer gas flow and cluster drift

When clusters are located in a buffer gas, and this buffer gas flows through a tube of a constant cross section, i.e., it is

moving with a constant drift velocity, then under equilibrium the drift velocity of clusters becomes equal to the drift velocity of the buffer gas flow after some time. But in the case of a varied cross section of a tube through which a buffer gas is flowing, the drift velocity of a buffer gas varies along the tube. Correspondingly, the drift velocity of clusters tends to the drift velocity of the buffer gas, but if the rate of variation in the buffer gas drift velocity is not small, the cluster drift velocity does not have time to follow the buffer gas drift velocity, and the equilibrium between the buffer gas flow and the cluster drift velocity is violated. Below, we analyze the character of the establishment of this equilibrium.

Let us consider the character of the establishment of equilibrium for clusters moving in a flow of a buffer gas if the drift velocity $u(z)$ of the buffer gas varies along the tube z-axis. We assume a small cluster concentration when they do not influence the flow and do not interact with each other. For determining the cluster drift velocity u, we use the Boltzmann kinetic equation for clusters in a buffer gas flow, which accounts for elastic collisions between the atoms of a buffer gas and clusters. This equation (3.3) takes the form

$$\frac{\partial f(\mathbf{v})}{\partial t} = \int \left[f(\mathbf{v}')\, \varphi(\mathbf{v}_1') - f(\mathbf{v})\, \varphi(\mathbf{v}_1) \right] \mathrm{d}\sigma\, \mathrm{d}\mathbf{v}_1 \,.$$

Here, $f(\mathbf{v})$ is the velocity distribution function for the clusters, $\varphi(\mathbf{v}_1)$ is the velocity distribution function for the atoms, $\mathbf{v}$, $\mathbf{v}_1$ are the velocities of clusters and atoms before a collision, $\mathbf{v}'$, $\mathbf{v}_1'$ are the velocities of clusters and atoms after a collision, and $d\sigma$ is the differential cross section of an elastic atom–cluster collision that leads to a given variation in velocities.

Multiplying this equation by the cluster momentum $M\mathbf{v}$, where M is the cluster mass, and integrating over the cluster velocities, we obtain the equation for the average cluster momentum $\mathbf{P} = \int M\mathbf{v} f(\mathbf{v})\, \mathrm{d}\mathbf{v}/N_{\mathrm{cl}}$:

$$N_{\mathrm{cl}} \frac{\mathrm{d}\mathbf{P}}{\mathrm{d}t} = \int \mu \mathbf{g} f(\mathbf{v})\, \varphi(\mathbf{v}_1)\, \sigma^*(g)\, \mathrm{d}\mathbf{v}\, \mathrm{d}\mathbf{v}_1 \,. \tag{4.4}$$

Here, N_{cl} is the number density of clusters (the distribution functions are normalized to the number densities of corresponding particles), $\mu = Mm/(M+m)$ is the reduced atom–cluster mass (m is the atomic mass), $\mathbf{g} = \mathbf{v}_1 - \mathbf{v}$ is the relative velocity of atom–cluster collisions, and $\sigma^*(g) = \int (1 - \cos\vartheta)\, \mathrm{d}\sigma$ is the transport cross section for elastic atom–cluster scattering. Assuming the cluster to be large, we take this cross section to be $\sigma^*(g) = \pi r_0^2$, where r_0 is the cluster radius.

We now take into account that the cluster mass is relatively large ($M \gg m$), i.e., $\mu = m$, and, correspondingly, the cluster distribution function is relatively narrow, which allows us to use a simple expression for the cluster velocity distribution function [154, 155]

$$f(\mathbf{v}) = N_{\mathrm{cl}} \delta(\mathbf{v} - \mathbf{w}) \,,$$

where $\mathbf{w}$ is the cluster drift velocity.

This simplifies the analysis, and equation (4.4) then takes the form

$$\frac{\mathrm{d}\mathbf{w}}{\mathrm{d}t} = \frac{m}{M} N \bar{v} \sigma (\mathbf{u} - \mathbf{w}) \,. \tag{4.5}$$

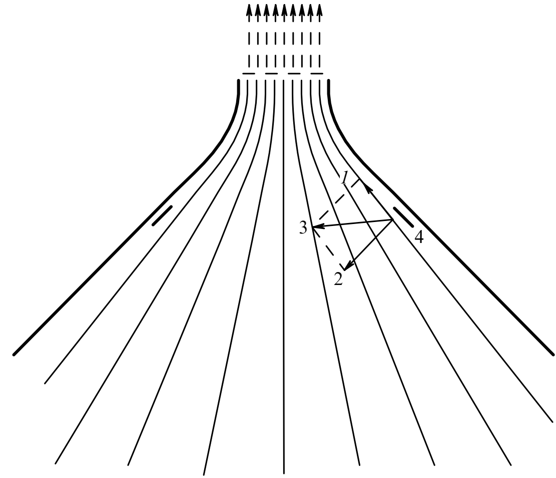

Figure 16. The current lines for a buffer gas flow inside a conic chamber near an orifice, when the flow passes the orifice: *1* — the force acting on a cluster from a buffer gas flow; *2* — the force from an electric field; *3* — the total force acting on the cluster, and *4* — a ring electrode.

Here, N is the number density of atoms, $\bar{v} = \sqrt{8T/(\pi m)}$ is the average atom velocity, $\sigma = \pi r_0^2$ is the cluster cross section, and $\mathbf{u}$ is the flow velocity (the drift velocity of atoms) at a given point.

In the case $\mathbf{u} = \mathrm{const}$, the solution of equation (4.5) gives

$$\mathbf{w} = \mathbf{w}_0 + (\mathbf{u} - \mathbf{w}_0) \exp\left(-\frac{m}{M} N \bar{v} \sigma t \right),$$

where $\mathbf{w}_0$ is the cluster drift velocity at the beginning. Thus, an equilibrium drift velocity of clusters is established after $\sim M/m$ collisions with buffer gas atoms. Correspondingly, equation (4.5) for the drift velocity of clusters $w(t)$, which tends to the velocity $u(t)$ of the buffer gas flow, takes the form

$$\frac{\mathrm{d}w}{\mathrm{d}t} + \nu w = \nu u \,, \tag{4.6}$$

where $\nu = N \bar{v} \sigma m / M$.

As a matter of fact, this equation describes the evolution of the cluster drift velocity for a varying drift velocity of a buffer gas in which the clusters are located. From this equation it follows that violation of the equilibrium with respect to the drift velocity of a buffer gas flow and clusters proceeds in a region with the maximum rate of variation in flow velocity. This takes place near the exit of the tube where the buffer gas flows, and therefore below we analyze the cluster–buffer gas equilibrium near the magnetron chamber exit where it is established. For definiteness, we take the conic shape of the magnetron chamber near the orifice, and Fig. 16 gives the current lines for a gas in this case. Because the total flux of atoms is conserved in each cross section of the cone chamber near the orifice, atoms move, on average, along the straight current lines.

Because of the conservation of the total rate of buffer gas flow in each chamber cross section, the drift velocity of buffer gas atoms increases towards the orifice and creates a force that acts on the clusters, compelling them to increase the drift velocity up to the gas drift velocity. But the establishment of an identical drift velocity for the clusters and the gas flow

requires a long time compared to the typical collision time because of a large cluster mass, and these drift velocities are different near the orifice. As a consequence of the conservation of the total rate of the cluster flow, the number density of the clusters increases near the orifice, which accelerates cluster coagulation processes if the clusters are neutral. We will also assume the clusters to be charged and the wall surface to have an electric potential. This electric potential can be created due to electrodes located on the walls and leads to repulsion of the clusters from the electrodes. In this way, focusing occurs for clusters when they approach the exit orifice. We will analyze this process in detail below, being guided by experimental conditions.

Let us consider the character of the flow of a pure buffer gas in a conical chamber that terminates at an orifice. We denote the axis of this chamber by z, with $z = 0$ at the orifice of a radius R_0. The straight current lines form a certain angle with the cone axis (see Fig. 16), and its maximum value relates to the chamber walls. We denote the angle between the conical walls near the orifice and the tube axis by α and, assuming the number density of a buffer gas to be constant inside the drift chamber, we have for the drift velocity of a flow at a distance z from the orifice:

$$u(z) = \frac{u_0 R_0^2}{(R_0 + z\tan\alpha)^2}\,, \tag{4.7}$$

where u_0 is the drift velocity of the flow at the orifice inside the drift chamber. Introducing the parameter

$$\xi = 1 + \frac{z}{R_0 \tan\alpha}\,,$$

and representing relation (4.7) as the equation

$$u(z) = -\frac{\mathrm{d}z}{\mathrm{d}t} = \frac{u_0}{\xi^2}\,,$$

we obtain the solution to this equation in the form ($\mathrm{d}z = R_0 \tan\alpha\,\mathrm{d}\xi$)

$$\xi^3 = \frac{t_0 - t}{\tau_0}\,, \qquad \tau_0 = \frac{R_0}{3u_0\tan\alpha}\,. \tag{4.8}$$

Here, t varies from zero at $\xi = \xi_0$ up to $t_0 - \tau_0$, when $\xi = 1$. In particular, taking the parameters of the argon flow as $\alpha = 45^\circ$, $R_0 = 3$ mm, and $u_0 = 2.6 \times 10^4$ cm s^{-1}, we obtain the typical time of variation of the flow velocity: $\tau_0 = 4.5 \times 10^{-6}$ s.

Furthermore, let us use experimental parameters for a silver magnetron plasma [143, 235], where silver clusters of an average size of $n = 7{,}000$ are resided in argon at a pressure of $p = 0.12$ mbar and temperature $T = 200$ K ($N = 5 \times 10^{15}$ cm^{-3}), so that the parameter ν is found to be 2.5×10^3 s^{-1}. At the beginning, the cluster drift velocity coincides with the drift velocity of the buffer gas flow, namely

$$w(0) = u(0) = \frac{u_0 \tau_0^{2/3}}{t_0^{2/3}}\,,$$

where τ_0 is determined by formula (4.8), and the time-dependent drift velocity of a buffer gas is given by

$$u(t) = \frac{u_0}{\xi^{2/3}} = \frac{u_0 \tau_0^{2/3}}{(t_0 - t)^{2/3}}\,.$$

Substituting this expression into equation (4.6), we obtain the equation for the cluster drift velocity $w(t)$ in the form

$$\frac{\mathrm{d}}{\mathrm{d}t}\bigl(\exp(\nu t)w\bigr) = \nu u \exp(\nu t) = \frac{\nu u_0 \tau_0^{2/3}}{(t_0 - t)^{2/3}}\exp(\nu t)\,.$$

The solution of this equation is written as

$$w(t) = \nu u_0 \tau_0^{2/3}\exp(-\nu t)\int_0^t \frac{\exp(\nu t')}{(t_0 - t')^{2/3}}\,\mathrm{d}t'\,. \tag{4.9}$$

If $\nu\tau_0 \ll 1$, we find the following expression for the drift velocity of clusters at an orifice:

$$w = u_0(\nu\tau_0)^{2/3}\Gamma\left(\frac{1}{3}\right) = 2.68 u_0 (\nu\tau_0)^{2/3}\,. \tag{4.10}$$

Thus, the equilibrium between the drift velocities of clusters and buffer gas atoms is violated in this limit, and the drift velocity of clusters near the orifice is less than the flow velocity. Formula (4.9) allows us to find the cluster drift velocity. In particular, under the above experimental parameters formula (4.10) gives $w/u_0 = 0.13$, and $w = 3 \times 10^3$ cm s^{-1} is one order of magnitude lower than the drift velocity of argon gas as it leaves the chamber. Note that by virtue of the criterion $\nu\tau_0 \ll 1$ the drift velocity of clusters near the orifice depends on the cluster size as

$$w \sim \sigma^{-2/3} \sim n^{-4/9}\,,$$

and the number density of clusters near the orifice is inversely proportional to the cluster velocity, so that the size distribution function f_n of clusters near the orifice is expressed through the size distribution function $f_n^{(0)}$ far from the orifice as

$$f_n = n^{4/9} f_n^{(0)}\,.$$

This means that the size distribution function (3.15) $f_n \sim n^{-2/3}$ in the basic part of cluster sizes is transformed due to the effect under consideration into $f_n \sim n^{-2/9}$.

4.3 Attachment of clusters to walls

We now analyze the character of attachment of clusters of a charge Ze to the walls of the drift chamber. If a voltage is applied to the walls and the charges of the walls and the clusters are equal in sign, the charged walls repulse the cluster when it is located near the walls, and this prevents attachment of the cluster to walls. In other words, a force occurs from the walls that acts on the clusters and is directed to the axis of the conical chamber near the exit. As a result, the cluster moves with a drift velocity w to the chamber axis. The diffusion coefficient of a cluster of size n in a gas is denoted by D_n, and the diffusion motion of clusters leads to their attachment to the walls, if the cluster is located long enough inside the drift chamber. We will characterize this process by the probability $P(x_0, t)$ of the cluster attachment to the walls if at the beginning it is located at a distance x_0 from the walls. For simplicity, we take this distance x_0 to be small compared to the radius of the wall curvature r, which allows us to consider the wall as a plane and to study cluster attachment to the walls within the framework of a one-dimensional problem.

Taking the initial condition $P(x, 0) = \delta(x - x_0)$ and the boundary condition $P(0, t) = 0$, where $P(x, t)$ is the prob-

ability of a cluster being located at a distance x from the walls at time t, one can present this probability on the basis of formula (3.28) [25, 145, 148] introducing into it the cluster drift motion:

$$P(x,t)=\frac{1}{\sqrt{4\pi D_n t}}\left\{\exp\left[-\frac{(x-x_0-wt)^2}{4D_n t}\right]-\exp\left[-\frac{(x+x_0+wt)^2}{4D_n t}\right]\right\}. \qquad (4.11)$$

For the cluster flux to the boundary this gives

$$j=-D_n\,\frac{\partial P(x,t)}{\partial x}=\frac{x_0+wt}{\sqrt{4\pi D_n}\,t^{3/2}}\exp\left[-\frac{(x_0+wt)^2}{4D_n t}\right], \qquad (4.12)$$

and the probability W of a cluster attachment to the walls (we assume the attachment takes place if the cluster coordinate reaches the value $x=0$) equals

$$W=\int_0^\infty\frac{x_0+wt}{\sqrt{4\pi D_n}}\,\frac{\mathrm{d}t}{t^{3/2}}\exp\left[-\frac{(x_0+wt)^2}{4D_n t}\right]. \qquad (4.13)$$

Introducing the dimensionless parameter $\eta=x_0w/(4D_n)$ and the dimensionless variable $\tau=wt/x_0$, we represent this expression in the form

$$W(\eta)=\sqrt{\frac{\eta}{\pi}}\int_0^\infty\frac{(1+\tau)\,\mathrm{d}\tau}{\tau^{3/2}}\exp\left[-\frac{\eta(1+\tau)^2}{\tau}\right]. \qquad (4.14)$$

This integral is approximated by the formula

$$W(\eta)=\exp(-4\eta)=\exp\left(-\frac{x_0w}{D_n}\right). \qquad (4.15)$$

From this it follows that the probability of cluster attachment to the walls is unity in the absence of external radial fields if this cluster is located long enough inside the drift tube and moves as a result of diffusion. Next, assuming the electric field strength E to be relatively small, we have for the cluster drift velocity near a charged wall: $w=eE|Z|K$, where Z is the cluster charge, and because the cluster mobility K is connected with its diffusion coefficient D_n by the Einstein relation $K=eD_n/T$, formula (4.15) may be represented as

$$W=\exp\left(-\frac{eE|Z|x_0w}{T}\right). \qquad (4.16)$$

Let us make an estimate on the basis of this formula. We assume that the voltage is created by charged rings inside the drift chamber. The voltage of an isolated ring is given by

$$\varphi=\frac{\pi qeR}{\ln(8R/a)},$$

where R is the ring radius, a is the rod radius, qe is the total charge on the ring, and the electric field strength near the ring at a distance $x\ll R$ is equal to

$$eEx=ex\,\frac{qe}{2\pi Rx}=\frac{\varphi}{4\pi\ln(8R/a)}.$$

Under the experimental conditions $T=200$ K, $\varphi\sim100$ V, $R/a\sim100$, and $|Z|\sim1$ we find for the parameters of formula (4.16):

$$\frac{eE|Z|x_0w}{T}\sim50,$$

and the attachment of clusters to the walls is practically absent under these conditions when the electric potential near the walls is determined by their voltage, and the role of the cluster charge may be ignored.

4.4 Charging and evolution of charged clusters in a secondary plasma

The analysis made in Section 4.3 shows that by charging clusters and applying a voltage to walls, one can prevent clusters from attaching to the walls. In order to realize this situation, it is necessary to create a plasma of a low density [150], which can be a secondary plasma of a magnetron discharge. In considering a secondary plasma that is of importance for cluster charging, we will be guided by experiment [151] where electron and ion parameters were measured for a titanium magnetron plasma. This plasma is similar to a gas-discharge plasma of a positive column of glow discharge [20, 25] that is supported by an external electric field. We use the fact that a typical electron number density is $N_e\sim10^{10}$ cm^{-3} and the average electron energy is 2–3 eV according to experiment [21] for a secondary plasma.

In the case where a quasineutral plasma of a low density is located in the magnetron chamber far from the magnetron discharge region, clusters move in the flow of a weakly ionized buffer gas and can acquire a charge as a result of the attachment of electrons and ions. This charge is negative because of the higher mobility of electrons, and below we determine this charge and the typical time of its acquisition taking the Maxwell distribution function of electrons. We assume that a weakly ionized plasma is quasineutral and each contact of an electron and ion with the cluster surface leads to transferring their charge to the cluster. We have the following expression for the rate of electron attachment to the cluster surface of a radius $r_0\ll\lambda$ (λ is the mean free path of gas atoms, and under typical conditions $\lambda=0.4$ cm) [139, 144–146]:

$$j_e=\frac{2}{\sqrt{\pi}}\int_{z_0}^\infty x^{1/2}\exp(-x)\,\mathrm{d}x\sqrt{\frac{2\varepsilon}{m_e}}\,\pi r_0^2=(1+z_0)\exp(-z_0)\sqrt{\frac{8T_e}{\pi m_e}}\,N_e\pi r_0^2.$$

Here, ε is the electron energy, T_e is the electron temperature, N_e is the number density of electrons, m_e is the electron mass, $x=\varepsilon/T_e$, $z_0=|Z|e^2/(r_0T_e)$, and Z is the negative cluster charge. We consider that the electron attachment to the cluster surface is possible if the electron energy ε exceeds the repulsion energy $|Z|e^2/r_0$ of charge interaction. The cross section of the ion contact with the surface of a charged cluster is equal to [153]

$$\sigma=\pi r_0^2\left(1+\frac{|Z|e^2}{r_0\varepsilon}\right),$$

and the ion current to the cluster surface amounts to

$$j_i=(1+z_0)\sqrt{\frac{8T_i}{\pi m_i}}\,N_i\pi r_0^2,$$

where N_i is the ion number density, T_i is the ion temperature, and m_i is the ion mass. Equalizing the electron and ion

currents received by the surface of a charged cluster and assuming the plasma to be quasineutral, $N_{\rm e} = N_{\rm i}$, we find for the cluster charge [139]:

$$|Z| = \frac{r_0 T_{\rm e}}{2e^2} \ln \frac{m_{\rm i} T_{\rm e}}{m_{\rm e} T_{\rm i}} \, ;$$

we assume $|Z| \gg 1$, i.e., the attachment of one electron or ion does not change the interaction between a charged cluster and electrons or ions.

Under experimental conditions for a titanium magnetron plasma [35] we take the cluster size $n = 2 \times 10^4$, which corresponds to the cluster radius $r_0 = r_{\rm W} n^{1/3} = 4.5$ nm ($\pi r_0^2 = 6.4 \times 10^{-13}$ cm^2). Taking $T_{\rm e} = 2$ eV [148] and $T_{\rm i} = 400$ K [21], we obtain from this the values of $z_0 = 3.6$, and $Z = -22$. We may also examine experimental conditions for silver clusters [35] with $n = 7 \times 10^3$, i.e., $r_0 = 3.1$ nm ($\pi r_0^2 = 3.2 \times 10^{-13}$ cm^2). We then obtain $z_0 = 4.6$, and $Z = -18$.

Let us analyze the typical time for the establishment of the charge equilibrium that results from the attachment of electrons and ions to the cluster surface. The attachment rate constants of electrons ($k_{\rm e}$) and ions ($k_{\rm i}$) to the surface of a neutral cluster are equal, respectively, in the case of titanium magnetron plasma ($T_{\rm e} = 2$ eV, $T_{\rm i} = 400$ K):

$$k_{\rm e} = \sqrt{\frac{8T_{\rm e}}{\pi m_{\rm e}}}\, \pi r_0^2 \approx 6.0 \times 10^{-5}\ {\rm cm^3\ s^{-1}} \, ,$$
$$k_{\rm i} = \sqrt{\frac{8T_{\rm i}}{\pi m_{\rm i}}}\, \pi r_0^2 \approx 5.2 \times 10^{-8}\ {\rm cm^3\ s^{-1}} \, . \qquad (4.17)$$

Correspondingly, the typical times of electron ($\tau_{\rm e}$) and ion ($\tau_{\rm i}$) attachment to a neutral cluster are given by

$$\tau_{\rm e} = (k_{\rm e} N_{\rm e})^{-1} \, , \qquad \tau_{\rm i} = (k_{\rm i} N_{\rm i})^{-1} \, ,$$

where $N_{\rm e}$, $N_{\rm i}$ are the electron and ion number densities. Taking according to Ref. [151] $N_{\rm e} \sim 2 \times 10^{10}$ cm^{-3}, we find the typical time of cluster charging, $\tau_{\rm e} \sim 10^{-6}$ s, and the typical time for establishing the cluster charge equilibrium in the case of a titanium magnetron plasma: $\tau_{\rm i}/|Z| \sim 5 \times 10^{-5}$ s. It is useful to compare these times with the drift time of cluster ions in a secondary plasma. Considering clusters to be moving in a buffer gas flow in a conical tube, we find the drift time

$$\tau_{\rm dr} = \int_R^{r_0} \frac{{\rm d}z R^2}{u_0 r_0^2} = \frac{R^3}{3 \tan \alpha \, u_0 r_0^2} \, . \qquad (4.18)$$

Taking advantage of the experimental conditions $R = 5$ cm, $\alpha = 45°$, $r_0 = 3$ mm, $u_0 = 2.2 \times 10^4$ cm s^{-1}, we obtain $\tau_{\rm dr} = 0.02$ s. Thus, under experimental conditions, the drift time of clusters exceeds significantly the typical time for establishing a charge equilibrium, i.e., the equilibrium cluster charge is established in the course of buffer gas drift at the end of the magnetron chamber.

In these estimations we considered charging of an individual cluster assuming that this process does not violate the charge equilibrium of a magnetron plasma. One can reveal that it is not fulfilled for the real example of a titanium magnetron plasma [35] with the number density of bound atoms in clusters being $N_{\rm b} \sim 10^{15}$ cm^{-3}, and the average cluster size $n = 2 \times 10^4$. If we use the above estimate for the negative cluster charge $Z \approx -20$, we find that the number density of the negative charge due to clusters is $\sim 10^{12}$ cm^{-3}, which exceeds the number density of electrons $N_{\rm e} \sim 10^{10}$ cm^{-3} [151] in a magnetron plasma far from the cathode.

Note that the cluster regime of magnetron discharge is realized at high discharge powers. This means that the number density of bound atoms in the clusters must be large in this regime, and hence saturation of the plasma is typical for such a plasma. We demonstrate it by the example of a titanium magnetron plasma as analyzed in experiment [151], with the electron number density varying in a range $(0.3-1.5) \times 10^{10}$ cm^{-3} for a discharge power 30 – 110 W. Correspondingly, the ion current to the walls varies within the range $(2-5) \times 10^{17}$ cm^{-2} s^{-1} for this power range. Simultaneously, the voltage near the walls that was considered to be a plasma potential and equalized the electron and ion currents to the walls ranged from 0.4 to 0.6 eV for these discharge powers. This corresponds to a number density of ions $N_{\rm i} \sim 10^{12}$ cm^{-3}, which is two orders of magnitude higher than that for electrons. Such a magnetron plasma cannot be unipolar because of the high plasma voltage in this case. Hence, one can expect that the excess of the negative charge is taken up by the clusters.

Thus, we conclude that in the secondary cluster plasma of magnetron discharge the negative charge is transferred to clusters in the course of plasma decay. We now analyze this in detail for a titanium magnetron plasma taking its electron and ion parameters on the basis of experiment [151], and cluster parameters on the basis of experiment [35]. In considering a magnetron discharge for a titanium cathode, we restrict ourselves first to a power of 100 W and argon pressure of 0.7 Pa, which corresponds to the number density $N_{\rm a} = 1.7 \times 10^{14}$ cm^{-3} of argon atoms at a temperature of 300 K. Under these conditions, the electron temperature is $T_{\rm e} = 2\varepsilon_{\rm e}/3 = 2$ eV, and the ion temperature is $T_{\rm i} = 2\varepsilon_{\rm i}/3 = 0.6$ eV [151]. Next, the number density of electrons is $N_{\rm e} = 1.2 \times 10^{10}$ cm^{-3}, and the ion current density to the walls is $j_{\rm i} = 3.3 \times 10^{17}$ cm^{-2} s^{-1}, which corresponds to a number density of ions $N_{\rm i} = 4 \times 10^{12}$ cm^{-3}. The potential jump φ near the walls that equalizes the electron and ion currents to the walls is equal to $\varphi = 0.7$ eV. Note that the cross section of resonant charge exchange $\rm Ar^+ - Ar$ is equal to $\sigma_{\rm res} = 6.0 \times 10^{-15}$ cm^2 [158] at the above ion energy, which corresponds to a transport cross section $\sigma^* = 2\sigma_{\rm res} = 1.2 \times 10^{-14}$ cm^2, and the ion mean free path $\lambda = 0.5$ cm. For argon atoms, a mean free path is approximately two times more.

We now apply these data to the titanium cluster plasma examined in experiment [35]. By analogy with formulas (4.17), we have now for the rates of electron and ion attachment to a titanium cluster of an average size ($n = 2 \times 10^4$):

$$k_{\rm e} = \sqrt{\frac{8T_{\rm e}}{\pi m_{\rm e}}}\, \pi r_0^2 = 6.0 \times 10^{-5}\ {\rm cm^3\ s^{-1}} \, ,$$
$$k_{\rm i} = \sqrt{\frac{8T_{\rm i}}{\pi m_{\rm i}}}\, \pi r_0^2 = 3.0 \times 10^{-7}\ {\rm cm^3\ s^{-1}} \, .$$

Let us examine the following processes of cluster charging [146, 159]:

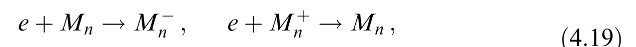

$$e + M_n \to M_n^- \, , \qquad e + M_n^+ \to M_n \, , \qquad (4.19)$$

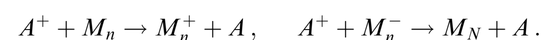

$$A^+ + M_n \to M_n^+ + A \, , \qquad A^+ + M_n^- \to M_N + A \, .$$

This scheme leads to the following set of balance equations for the number densities of neutral clusters (N_0), singly charged negative (N_-) and positive (N_+) cluster ions:

$$\frac{\mathrm{d}N_0}{\mathrm{d}t} = -k_\mathrm{e} N_\mathrm{e} N_0 - k_\mathrm{i} N_\mathrm{i} N_0 + k_\mathrm{i}\left(1 + \frac{e^2}{r_0 T_\mathrm{i}}\right) N_\mathrm{i} N_- + k_\mathrm{e}\left(1 + \frac{e^2}{r_0 T_\mathrm{e}}\right) N_\mathrm{e} N_\mathrm{e}\,,$$

$$\frac{\mathrm{d}N_+}{\mathrm{d}t} = k_\mathrm{i} N_\mathrm{i} N_0 - k_\mathrm{e}\left(1 + \frac{e^2}{r_0 T_\mathrm{e}}\right) N_\mathrm{e} N_\mathrm{e}\,,$$

$$\frac{\mathrm{d}N_-}{\mathrm{d}t} = k_\mathrm{e} N_\mathrm{e} N_0 - k_\mathrm{i}\left(1 + \frac{e^2}{r_0 T_\mathrm{i}}\right) N_\mathrm{i} N_-\,.$$

We restrict ourselves for simplicity to singly charged ions only. The factors accounting for the Coulomb interaction of colliding particles in these formulas are equal under the above parameters to

$$\frac{e^2}{r_0 T_\mathrm{e}} = 0.15\,, \qquad \frac{e^2}{r_0 T_\mathrm{i}} = 0.6\,.$$

Note that the charge equilibrium is established over several microseconds under these conditions. The ratios of the equilibrium number densities of clusters are defined as

$$\frac{N_-}{N_0} = \frac{k_\mathrm{e} N_\mathrm{e}}{k_\mathrm{i} N_\mathrm{i}(1 + e^2/r_0 T_\mathrm{i})}\,, \qquad \frac{N_+}{N_0} = \frac{k_\mathrm{i} N_\mathrm{i}}{k_\mathrm{e} N_\mathrm{e}(1 + e^2/r_0 T_\mathrm{e})}\,.$$

From this follows the expression for the number density ratio of positively and negatively charged clusters:

$$\frac{N_+}{N_-} = \left(\frac{k_\mathrm{e} N_\mathrm{e}}{k_\mathrm{i} N_\mathrm{i}}\right)^2 \frac{1 + e^2/r_0 T_\mathrm{e}}{1 + e^2/r_0 T_\mathrm{i}}\,.$$

If we apply the electron and ion parameters of the titanium magnetron plasma of experiment [151] to the titanium magnetron plasma of experiment [35], we find from the above formulas that 40% of the clusters are neutral, 36% of the clusters are positively charged, and 24% of the clusters are negatively charged (the ratio of the number densities for positively and negatively charged clusters equals 1.5).

We now analyze from this standpoint experiment [143] with a silver magnetron plasma where the ratio of the fluxes for positively and negatively charged clusters was 3/2. If we use the electron and ion parameters of a titanium magnetron plasma, we find that this regime can be realized at the ratio of the electron to ion number densities equal to $N_\mathrm{e}/N_\mathrm{i} = 2.4 \times 10^{-3}$, instead of $N_\mathrm{e}/N_\mathrm{i} = 3.0 \times 10^{-3}$ for a titanium magnetron plasma. It should be noted that in this analysis we have fixed the total number density of clusters in accordance with the experiment [151]. The charge equilibrium for clusters varies as electrons and ions attach to the chamber walls.

One can add that the cluster growth can continue due to the slowing of cluster drift when it moves towards the exit orifice. Indeed, in this region the number density of clusters increases and the drift velocity decreases, which increases the rate of the coagulation process. The coagulation processes [160] proceed according to the scheme

$$M_n + M_k \rightarrow M_{k+n}\,. \tag{4.20}$$

Within the framework of the liquid drop model for cluster collisions and for the size distribution function $f_n \sim \exp(-n/\overline{n})$ (n, k is the number of cluster atoms, $\overline{n}$ is its average value), the following balance equation is valid for the average cluster size [161, 162]:

$$\frac{\mathrm{d}\overline{n}}{\mathrm{d}t} = 3.4\, k_0 N_\mathrm{b} \overline{n}^{\,1/6}\,. \tag{4.21}$$

Let us make an estimation for a titanium magnetron plasma when $\overline{n} = 2 \times 10^4$, $N_\mathrm{b} = 1 \times 10^{15}$ cm^{-3}, and $T = 200$ K. Taking the above estimates for the cluster drift time near the orifice $\tau_\mathrm{dr} \sim 0.02$ s, we find that the cluster size variation near the exit orifice due to coagulation is $\Delta n \sim 10^4$, which is comparable to the typical cluster size.

This shows that the coagulation processes near the exit orifice, where these processes are intensified due to violation of the equilibrium between drift of a buffer gas and clusters, can be of importance for establishing the final cluster size. The peculiarities of the coagulation process should be noted. First, this process is stronger for large clusters and hence it widens the size distribution function of the clusters. Second, because solid clusters participate in this process, coagulation leads to formation of porous structures, rather than compact ones. Third, because the clusters are charged, coagulation leads to recombination of charges, and this process is more effective for joining clusters of opposite charges.

In conclusion of the analysis of processes involving charged clusters in a magnetron plasma, we note that processes of cluster growth, cluster transport, and cluster charging in a magnetron plasma lead to a certain hierarchy of times for these processes, which determines the character of cluster evolution.

4.5 Passing a gas flow with clusters through an orifice

An important stage of cluster evolution in a magnetron plasma is the passing of a buffer gas flow with clusters through an orifice out from the magnetron chamber. Below, we assume the orifice radius to be large compared to the mean free path of buffer gas atoms, i.e., the outflow of a buffer gas has a hydrodynamic character. As was already noticed above, the clusters are charged due to collisions with electrons and ions of the secondary plasma, and there are neutral clusters along with positively and negatively charged clusters. Because the electrons of a secondary plasma attach to walls, the relative portion of negatively charged clusters increases at the output. When these clusters approach the orifice to which a certain voltage is applied with respect to the plasma, neutral and positively charged clusters attach to the walls, and only negatively charged clusters remain in the flow. Hence, the best method to conserve clusters in a flow is to give them a charge, so that they are repulsed from the walls.

This is possible under certain conditions if the flowing time is large compared to the time of electron attachment to the walls. Below, we assume that all the clusters are negatively single-charged and positively charged ions go to the walls and hence do not destroy their charge. But then we obtain a unipolar plasma, and its charge creates an electric field that compels the clusters to move to the walls. Let us determine the voltage of the walls near the orifice, which will prevent attachment of charged clusters to the walls. Evidently, it must exceed the electric potential U of this unipolar plasma. Below, we determine this potential for the titanium magnetron plasma of experiment [35].

We use the parameters of this plasma where titanium clusters have an average size $n = 2 \times 10^4$, and the number density of bound atoms in the clusters is $N_b = 1 \times 10^{15}$ cm^{-3}. Assuming these clusters are singly charged, we obtain the number density of charged clusters, $N_{ch} = 5 \times 10^{10}$ cm^{-3}, when they are located far from the orifice. When the clusters approach the orifice, we assume for definiteness that their number density increases by 10 times, i.e., the number density of charged clusters becomes $N_{ch} = 5 \times 10^{11}$ cm^{-3} near the orifice. Take the orifice radius in accordance with the experiment to be $r = 3$ mm and find the electric potential φ of a unipolar plasma that is determined by the Poisson equation for the plasma potential φ:

$$\Delta\varphi = \frac{1}{\rho}\frac{\mathrm{d}}{\mathrm{d}\rho}\left(\rho\,\frac{\mathrm{d}\varphi}{\mathrm{d}\rho}\right) = -4\pi e N_{ch}\,,$$

where N_{ch} is the number density of charged clusters, and ρ is the distance from the axis. Assuming the number density of the clusters to be constant over the plasma cross section, we find the electric potential of this unipolar plasma:

$$\varphi_0 = \pi e N_{ch} r^2 = 20\ \mathrm{kV}\,. \tag{4.22}$$

Evidently, this plasma is steady in the field of the orifice, i.e., the charged clusters do not move to the walls, if the inequality

$$\varphi_0 > V_0$$

is fulfilled, where V_0 is the orifice voltage with respect to the plasma potential.

One can see that the obtained value V_0 is the minimum voltage which prevents charged clusters from attachment to the walls, but it is not attainable for this experimental technique. Note that this voltage is proportional to $N_{ch}r^2$, which in turn is proportional to $N_b r^2 w$, i.e., the amount of metal that is transported through the orifice. Because this amount is determined by the power of magnetron discharge, from this it follows that the electric capacity of a round orifice and, correspondingly, its carrying capacity is not sufficient to transport the metal that is sputtered under typical discharge powers. Hence, a round orifice is not suitable for this goal. It is necessary to use an oblong orifice or a gap, and then this problem will be overcome.

In conclusion of the analysis of cluster transport in a flow of a buffer gas, we note that metal clusters are generated effectively under the action of magnetron discharge with a large efficiency of formation of metal atoms. But because of a low gas density, metal atoms and clusters can attach to walls of the drift chamber. In order to escape this, it is convenient to use an external electric field that is created by rod rings to which a suitable voltage is applied. In addition, magnetron discharge must be organized in such a way that a weak secondary plasma exists far from the magnets. Due to this plasma, the clusters are charged, and by applying a voltage to the chamber walls one can prevent the attachment of the clusters to the walls. But charged clusters create an additional voltage in the flow that can compensate for the wall voltage, and for large cluster fluxes this effect may be strong for a round orifice through which the flow with clusters passes out from the chamber. Using of an oblong outlet orifice allows one to prevent this problem at a given wall voltage.

It should also be noted that although in this analysis we leaned upon a restricted number of experimental studies, the conclusions have a general character. Indeed, the formation of metal clusters in a magnetron plasma is a threshold process that is realized at a relatively high discharge power, a high density of buffer gas, and a low drift velocity of buffer gas flow. This follows from theoretical models based on experimental results. Next, the basic loss of a sputtered metal as a result of attachment of metal atoms and clusters to walls takes place near the exit of the magnetron chamber. In order to decrease the attachment rate, it is convenient to charge the clusters in the secondary plasma of the magnetron discharge and apply an appropriate voltage to the walls. But even under profitable conditions, the carrying capacity of a round orifice for the charged clusters is restricted due to the space charge of the clusters. This problem may be solved by using an extended exit orifice and a smooth transition from the magnetron chamber to its exit in order to conserve the laminar buffer gas flow. Hence, the geometry of the magnetron chamber and its construction are of importance for the efficiency of the cluster yield.

5. Cluster deposition and cluster structures

5.1 Cluster beams for the fabrication of films and materials

The peculiarity of clusters as a real physical object consists in a high specific surface energy and, correspondingly, high chemical reactivity. Therefore, contact of clusters leads to their joining, and the specific properties of incident clusters are lost in a joined cluster. Accordingly, clusters easily attach to surfaces. Therefore, in contrast to ultradispersive powders, which may be retained for a long time under specific conditions [163], clusters must be used promptly after their generation. Moreover, if clusters are located in a gas or plasma, this system is unstable with respect to their joining. This means that the size distribution function of clusters varies in time. This all shows that under real conditions clusters exist in some times scales that are used in cluster applications where the clusters can be in the form of cluster beams or the flow of a buffer gas with clusters.

There are two branches in cluster applications. In the first, a solid density of clusters, together with their small mass, is utilized, which allows one to excite the cluster matter in the optimal way if we compare this with another nonexplosive excitation methods. Usually, clusters consisting of inert gas atoms are used in such applications. An excited cluster matter is a source of X-rays or neutrons [164–167]. Because of the decay of an excited cluster, the duration of the pulse for cluster excitation is in the femtosecond range. Because of a large atom density in clusters, a high absorption of the laser pulse is attained, and this leads to a high specific excitation of the cluster matter that contains a small mass. In the case of a solid target, the absorbed energy is consumed for a larger mass that leads to a weaker specific excitation of the matter.

Another branch of cluster applications consists in cluster deposition on a target and fabrication in this manner of thin films and new materials. As a matter of fact, the cluster role reduces in this case to material transport from one object to another. In particular, in the magnetron method of cluster generation, which is now the object of our consideration, this method allows one to transport metal atoms from the cathode to the target. But, in spite of the nonprincipal role of clusters in these applications, the formation and transport of clusters is the most difficult part of the total problem, and therefore

this method of film deposition is termed the cluster method. Note that this method allows one to adjust the film thickness and to create multilayer films.

Production of thin films is an important application of cluster beams [168 – 172]. This is one branch of nanotechnology [174 – 177] that consists of manufacturing materials and devices with nano-sized elements [168, 173]. Creation of nanomaterials and nanodevices leads to miniaturization of electronic devices. Simultaneously, a decrease in element sizes leads to a change in their physical properties. In particular, small islands of deposited materials, i.e., nanoparticles located on a substrate, are quantum objects and are considered to be quantum dots [178 – 181]. In addition, nano-sized particles exhibit specific catalytic properties which are lost in related bulk materials [176, 182, 183]. Thus, nanostructures resulting from cluster deposition have specific properties, which is of fundamental importance for contemporary nanotechnology [169, 171, 174 – 177].

There are two areas for the nanostructure applications. The first one is manufacturing of electronic devices with nano-sized elements. For this goal, organized islands are created on a film, and these islands have specific properties which provide operation of such devices. Since these islands are almost quantum objects, they are considered to be quantum dots [178 – 181]. The other area of nanotechnology relates to fabrication of nanostructured films with specific mechanical, optical, and chemical properties. Cluster beams allow one to produce so-called cluster-assembled materials [184 – 187] which have specific properties and constitute nanostructures.

There are two methods of film production by deposition of cluster beams. The ion cluster beam (ICB) method [188] uses a beam of charged clusters which are deposited on a target. According to its nature, this method is similar to the method of film deposition by atomic beams. In comparison with deposition by atomic beams, the ICB method provides higher fluxes of deposited materials and allows one to govern the energy of charged clusters. Construction of a film from individual blocks-clusters also leads to a softer heat regime of film growth. A drawback of the ion cluster beam method consists in a relatively low intensity of beams and a low rate of deposition in comparison, for example, with chemical methods. Therefore, application of the ICB method is of interest for microelectronics, where cluster beams allow one to fabricate thin uniform films of various materials, i.e., metallic, dielectric, semiconductor, and organic films (for examples, see Refs [189 – 202]). The maximum rate of deposition by this method is achieved when clusters are formed by free jet expansion of an evaporated metal, and it is determined by the saturation vapor pressure of the metal at the melting point. A small value of the saturation vapor pressure compared to the atmospheric gas pressure restricts the deposition rates for some metals. The maximum deposition rate related to silver clusters is 74 nm s^{-1} [203, 204], and for the deposition of zinc clusters the deposition rate reaches 100 nm s^{-1} [205, 206]. Deposited clusters in this method are found in the liquid state [207]. Note that the specific heat release in the course of this deposition by cluster beams is as low as $0.1 - 1$ W cm^{-2}. Because of the relatively small intensity, the ion cluster beam method is only applied for the fabrication of small elements of microelectronics.

The other method of application of cluster beams uses the low-energy cluster beam deposition (LECBD) technique and involves a beam of neutral solid clusters of small energy [206 – 210]. In this case, deposition of a cluster beam may be accompanied by the growth of the target. As a result, a forming film consists of a deposited uniform matrix with embedded clusters. In contrast to the ICB method of deposition of fine uniform films, in this case clusters are found in the solid aggregate state. Because magic numbers of cluster atoms are preferable for the formation of solid clusters, a cluster beam consists in this case of solid clusters of almost identical sizes. Thus, this method allows one to create nanometer films deposited from a vapor with embedded clusters of almost identical sizes, deposited from cluster beams. It is impossible to produce such structures by other methods, and clusters of various materials and sizes can be used for this purpose (see, for example, Refs [211 – 214]). These materials are uniform films with embedded clusters of close sizes. Films with embedded clusters can be employed as filters because clusters are absorbers in a certain spectrum range. The spectral characteristics of these filters can be controlled by the sort, size, and density of the embedded clusters. Alongside with filters, films consisting of a transparent matrix with embedded clusters can be utilized as elements of optoelectronics. Some optical transitions in clusters as atomic systems can be saturated, so that these films can be applied as optical locks due to their nonlinear transparency.

Films with embedded clusters of magnetic materials (Fe, Co, Ni) constitute magnetic nanostructures and are like multidomain magnetic systems. In this context, the advantage of such films is as follows. First, the size of individual grains in these films, which coincides with the cluster size, is several times less than for normal magnetic films. This fact reduces the saturated magnetic field for this magnetic material. Second, the close sizes of embedded clusters — magnetic grains — provides an improved precision and selectivity for devices on the basis on such magnetic materials. Third, the possibility of varying the type and size of embedded clusters allows one to operate the parameters of the magnetic films. Therefore, films with embedded clusters as cluster-assembled materials are a new prospective material for precise magnetic devices.

5.2 Cluster deposition on surfaces

The character of cluster deposition on a surface depends on both the cluster state and its energy [215, 217 – 219]. Of course, the type and state of the target, as well as the rate of deposition, also influence the properties of a forming film. Figure 17 exhibits the character of deposition of an individual cluster onto a surface, so that in the end liquid clusters form a compact film on the substrate surface, whereas solid clusters form a porous film. Being guided by a magnetron source of clusters, below we consider briefly the production of metallic films by deposition of solid clusters. Clearly, the forming material is analogous to that produced by the low-energy cluster beam deposition technique and involves a beam of neutral solid clusters of small energy [209, 212 – 214]. The difference with the magnetron method is such that clusters are charged in the optimal way by the cluster passing through the orifice (see Section 4). On the one hand, this allows one to focus and guide the cluster beam but, on the other hand, the intensity of the cluster beam in the magnetron method is significantly higher than that for the low-energy cluster beam deposition method. This can also influence the deposition process.

The processes of the growth of deposited clusters on a surface can be different depending on conditions. Below, we

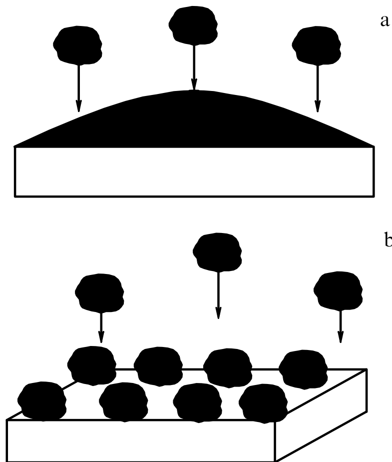

Figure 17. The processes of deposition on a surface for a liquid (a) and solid (b) cluster [6].

restrict ourselves to typical experimental regimes of magnetron cluster production, with a high intensity of the cluster beam and an energy of solid clusters below 1 eV per cluster atom in contrast to the laser method of generation of beams of metal clusters. An example of a forming structure is given in Fig. 5 in the case of deposition of silver clusters onto a silicon target. At the first stage of the process, separate clusters are located on the surface. Subsequently, with film growth neighboring clusters form chemical bonds between each other. Because the collision energy is not small, many cluster atoms make contact with adjoining clusters, and these clusters form a fast bond. As a result, some bridges arise between contiguous clusters (see Fig. 7), and these clusters form a fast structure.

The character of cluster attachment to a surface is similar to that in the case of formation of fractal structures, where solid particles attach to a surface and can move over it. This mechanism of joining solid particles on a surface in accordance with the DLA-model (diffusion limited aggregation) [220 – 223] or DDA-model (deposition diffusion aggregation) [224] accounts for the diffusion motion of particles over the surface. Contact between two particles leads with a certain probability to their joining, and the diffusion coefficient of an aggregate formed on the surface decreases. These models have been developed under various conditions; they have been analyzed in books and reviews [225 – 227] describing experimentally observed structures which result from cluster joining (see, for example, Refs [209, 228 – 230]).

In considering the real character of particle joining, we note that the reconstruction of a joined cluster proceeds slowly after contact, and this reconstruction is concerned with a region near the particle boundary. In contrast to the case of joining the liquid clusters, when they are first joined in a unit drop and finally form a compact film on the surface, in the case of solid particles a porous film is formed. Also, in contrast to the fractal structure of a film at low intensities of the cluster beam [209, 228 – 230], the forming film is not rarefied, and the typical pore size is on the order of the cluster size, whereas at low intensities the typical pore size may exceed the cluster size.

It should be noted that these films resulting from joining the solid clusters may be of interest as a magnetic material. Indeed, in such films clusters partially conserve their individuality, and can create individual domains in magnetic materials. Because the size distribution function of deposited clusters can be narrow, one can obtain in this way magnetic materials with resonant parameters which depend on cluster sizes in a cluster beam. For natural magnetic materials with a wide size distribution function of domains this is impossible.

The character of deposition of solid clusters on a substrate consists in the formation of fast chemical bonds between clusters at the point of their contact. Though these contacts may change in the course of formation of a stable structure, the number of contacts between neighboring clusters is restricted, while each cluster includes a large number of atoms. Hence, deposition of large solid metallic clusters onto a substrate leads to the formation of a porous structure, rather than the compact distribution of atoms that takes place in the case of liquid clusters. Each cluster partially conserves its individuality in a formed porous structure. One can see that films obtained by the deposition of solid clusters from a magnetron cluster source have intermediate properties between compact crystal structures and rarefied fractal structures. In particular, the lattice constants for such structures differ from those of crystal structures [231 – 235]. Along with this, the melting point for these materials is lower than that for bulk crystals. On the other hand, these materials conserve the crystal structure in the limits of individual clusters. In this way, one can change the properties of known crystal structures. This is of importance in processes where selective properties are employed, for example, the absorption spectrum of a crystal structure that exhibits the importance of such new materials. Figure 18 gives an example of the dependences for the parameters of a film resulting from deposition of solid clusters on the cluster size [235].

In creating new materials by the deposition of a solid cluster onto a substrate, one can change the parameters of the metal crystal lattice in the adjusting method, if selective properties of this material, such as the absorption spectrum, are used. This demonstrates the importance of such materials for science and technology.

5.3 Magnetron covering of dust particles with film

Among the various applications of a magnetron plasma, including a cluster magnetron plasma, is the covering of dusty particles by a metal in a magnetron plasma. An interesting property of dusty particles is that, upon being poured out of a container in a specific plasma, they get a charge from the plasma and form steady well-ordered structures, and their stability follows from the interaction with the plasma and fields that support the plasma. These structures were discovered in 1994 [236 – 239] and are the subject of detailed investigations (see, for example, Refs [240 – 246]). The negative charge of dielectric particles can reach a high value of $10^3 - 10^6 e$ [243, 247, 248], where e is the electron charge. This influences both the physical properties of particles in a plasma and its interaction with the environment.

A dusty plasma may be used in various applications. We study below its application due to the interaction with a magnetron plasma, which allows one to cover these particles with a metal layer. In the scheme used in experiments [157, 249, 250], the magnetron chamber is combined with a radiofrequency discharge that holds dielectric particles, compelling them to create stable ordered structures. Then, metal atoms sputtering from the cathode in magnetron discharge propagate toward the particles and cover them. Particle covering

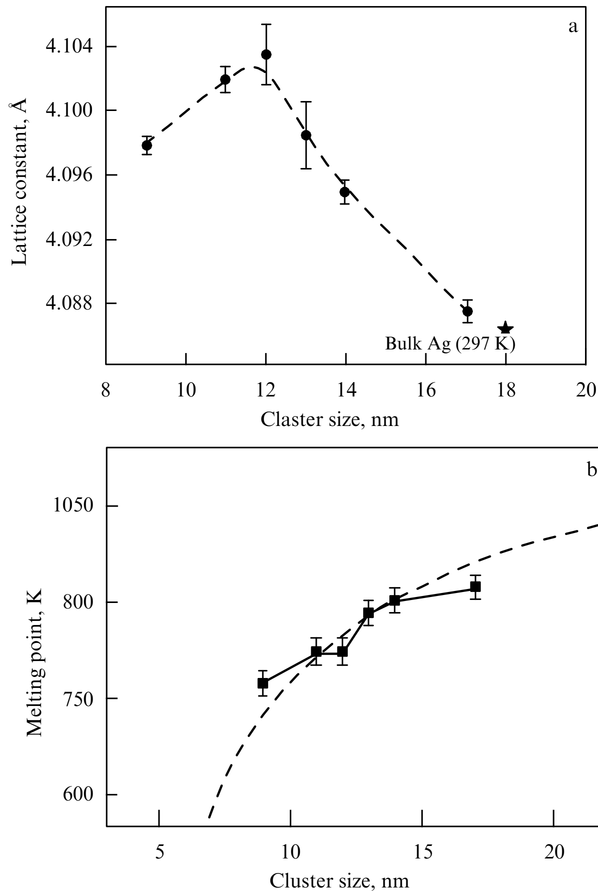

Figure 18. Parameters of a silver film deposited on a silicon substrate depending on the size of deposited clusters: the lattice constant (a) and the melting point (b). Symbols ● and ■ are experimental results, dashed curves are their approximations. The melting point of bulk silver is 1233 K.

depends on the character of interaction between attached atoms and their interaction with the surface, and Fig. 19 gives electron photographs of particles with a covering for various covered metals [157].

Because of the high intensity of cluster beams produced by the magnetron method, direct covering of particles by a metal is possible when particles are pouring out of a container. The scheme is depicted in Fig. 20 [159]. We make estimations when a particle of 1 μm radius is covered by a silver layer of thickness 0.2 μm. Assuming the covering process finishes in the time a particle falls, that is 0.1 s, and each cluster contains 10^4 atoms on average, we find that for the formation of an indicated layer 10^7 clusters must attach to the particle during this time, i.e., the time between neighboring attachment events is 10^{-8} s. Each attaching cluster gives momentum to the particle, i.e., the particle rotates, and a typical rotation frequency under these conditions is on the order of 10^{-9} s^{-1}. This means that clusters encounter the particle surface more or less uniformly. Hence, the structure of particle covering depends on the parameters of the process, and if interaction of clusters with the particle surface is stronger than the interaction between cluster atoms, clusters cover the particle surface more or less uniformly.

If attaching clusters are charged, they impart their charge to the particle. This fact may be used, and charged particles can be filtered out by an external electric field. A particle charge can be adjusted by an additional electron beam. One more peculiarity of this covering process is such that attachment of clusters creates a force acting on the particle. One can equalize the particle weight by this force, which allows one to regulate the time of particle location in the region of cluster action.

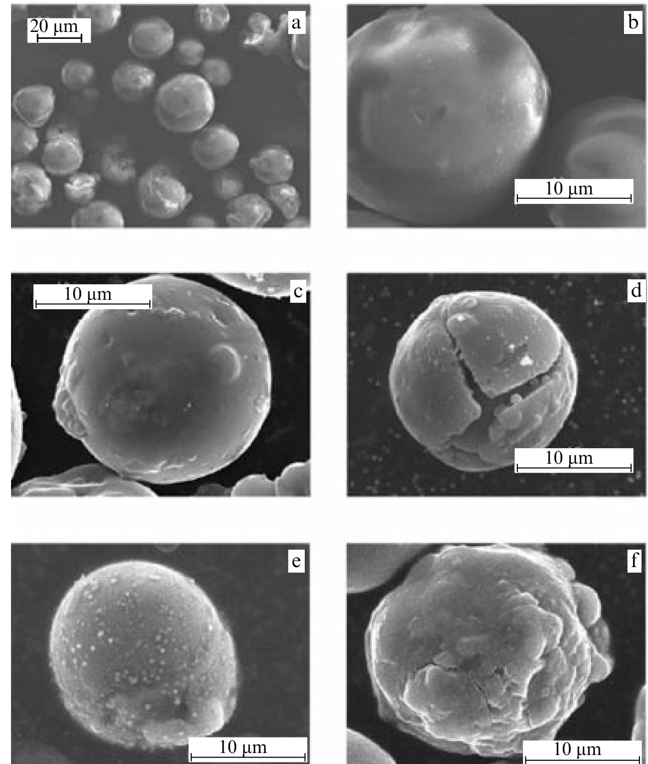

Figure 19. Photographs made by a scanning electron microscope for uncoated particles of silicon oxide (a, b), and those coated by Cu (c, d), Ti (e), and Al (f) [157].

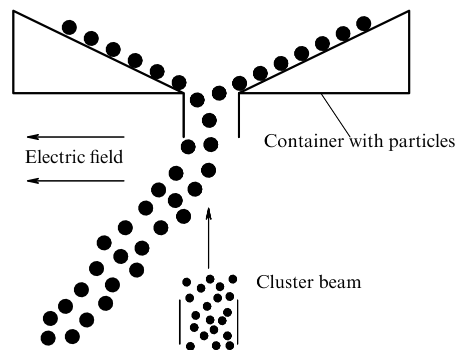

Figure 20. The scheme of the covering of dusty particles by the deposition of clusters.

Note that the jet expansion method of cluster generation that provides the maximum rate of deposition for silver clusters at 74 nm s^{-1} [251–254] is not suitable for this scheme. Indeed, this rate allows one to cover the particle by a silver layer of thickness 7 nm for a time of 0.1 s of particle falling. Additional charging and focusing of this beam allow one to realize particle covering within the framework of the indicated scheme. Note that approximately 3×10^{-11} g of silver is required for covering one particle, i.e., the total amount of deposited silver is restricted.

6. Conclusions

The above analysis shows that a magnetron plasma is a complex physical object whose properties are determined by processes involving electrons, ions, atoms, and clusters. Namely, the complex character of these processes takes place in the regime of a magnetron plasma, when clusters are formed there. Then processes of cluster formation compete with the processes of returning of sputtered metal atoms to the cathode. Therefore, the passage to the cluster regime of magnetron discharge proceeds sharply, and this regime relates to a high discharge power and a relatively high pressure of a buffer gas.

Extraction of forming clusters from the magnetron chamber proceeds through the transport of clusters to an exit orifice, and specific precautions are required to prevent clusters from attaching to chamber walls in spite of the small cluster mobility. This requires a careful analysis of transport processes in a flowing buffer gas and processes of cluster charging in a secondary plasma. In this way, it is necessary to construct a specific magnetron chamber, optimizing the cluster loss in it.

It should be noted that understanding the processes in a magnetron plasma is based for the most part on experimental results, which in turn require contemporary experimental diagnostics. These diagnostics combine a new electron microscopy technique with new methods of X-ray diagnostics and modified mass spectrometry with classical methods of spectroscopy, electron probes, and mass spectrometry. This becomes an arsenal of diagnostics represented in this paper, which complicates experimental studies and raises their costs, but it can be repaid by various applications in nanotechnology that must be based on a deep understanding of this subject.

The authors are grateful to Dr I Shyjumon for the fruitful collaboration. P V Kashtanov and B M Smirnov thank the Russian Foundation for Basic Research (grant 06-02-16146a) for financial support, and R Hippler thanks DFG (Research Center 6047-B6) for partial support.

References

1. Penning F M *Physica* **3** 563 (1936)
2. Kay E *J. Appl. Phys.* **34** 760 (1963)
3. Gill W D, Kay E *Rev. Sci. Instrum.* **36** 277 (1965)
4. Wasa K, Hayakawa S *Rev. Sci. Instrum.* **40** 693 (1969)
5. Mullay J R *Res./Dev.* **22** (2) 40 (1971)
6. Shyjumon I, PhD Thesis (Greifswald: Greifswald Univ., 2005)
7. Thornton J A, Penfold A S, in *Thin Film Processes* (Eds J L Vossen, W Kern) (New York: Academic Press, 1978)
8. Danilin B S, Syrchin V K *Magnetronnye Raspylitel'nye Sistemy* (Magnetron Sputtering Systems) (Moscow: Radio i Svyaz', 1982)
9. Danilin B S *Primenenie Nizkotemperaturnoi Plazmy dlya Naneseniya Tonkikh Plenok* (Low-Temperature Plasma Application to Thin Film Production) (Moscow: Energoatomizdat, 1989)
10. Westwood W D, in *Handbook of Plasma Processing Technology: Fundamentals, Etching, Deposition, and Surface Interactions* (Eds S M Rossnagel, J J Cuomo, W D Westwood) (Park Ridge, NJ: Noyes Publ., 1990)
11. Wasa K, Hayakawa S *Handbook of Sputter Deposition Technology: Principles, Technology and Applications* (Park Ridge, NJ: Noyes Publ., 1992)
12. George J *Preparation of Thin Films* (New York: M. Dekker, 1992)
13. Schiller S et al. *Surf. Coat. Technol.* **61** 331 (1993)
14. Scholl R A, in *36th Annual Technical Conf. Proc.* (*Society of Vacuum Coaters*) (Albuquerque, NM: SVC, 1993) p. 405
15. Frach P et al. *Surf. Coat. Technol.* **59** 177 (1993)
16. Schneider J M, Sproul W D, in *40th Annual Technical Conf. Proc.* (*Society of Vacuum Coaters*) (Albuquerque, NM: SVC, 1997) p. 301
17. Kelly P J, Arnell R D *J. Vac. Sci. Technol. A* **16** 2858 (1998)
18. Kelly P J, Arnell R D *J. Vac. Sci. Technol. A* **17** 945 (1999)
19. Chapman B *Glow Discharge Processes: Sputtering and Plasma Etching* (New York: Wiley, 1980)
20. Raizer Yu P *Fizika Gazovogo Razryada* (Gas Discharge Physics) (Moscow: Nauka, 1987) [Translated into English (Berlin: Springer-Verlag, 1991)]
21. Wolter M et al. *J. Phys. D: Appl. Phys.* **38** 2390 (2005)
22. Goeckner M J, Goree J A, Sheridan T E (Jr) *IEEE. Trans. Plasma Sci.* **PS-19** 301 (1991)
23. Child C D *Phys. Rev.* (Ser. I) **32** 492 (1911)
24. Langmuir I *Phys. Rev.* **2** 450 (1913)
25. Smirnov B M *Physics of Ionized Gases* (New York: John Wiley, 2001)
26. Rossnagel S M, Kaufman H R *J. Vac. Sci. Technol. A* **6** 223 (1988)
27. Haberland H et al. *Phys. Rev. Lett.* **69** 3212 (1992)
28. Haberland H et al. *J. Vac. Sci. Technol. A* **10** 3266 (1992)
29. Haberland H et al. *Mater. Sci. Eng. B* **19** 31 (1993)
30. Haberland H et al. *Z. Phys. D* **26** 8 (1993)
31. Haberland H et al. *J. Vac. Sci. Technol. A* **12** 2925 (1994)
32. Haberland H (Ed.) *Clusters of Atoms and Molecules* (New York: Springer-Verlag, 1994)
33. Haberland H et al., in *Beam Processing Advanced Materials, Proc. of the 2nd Intern. Conf., Cleveland, USA, 1995* (Eds J Singh, J Mazumder, S M Copley) (Materials Park, OH: ASM Intern., 1996) p. 1
34. Haberland H et al. *Surf. Rev. Lett.* **3** 887 (1996)
35. Shyjumon I et al. *Thin Solid Films* **500** 41 (2006)
36. Roth J R *Industrial Plasma Engineering* Vol. 2 *Applications to Nonthermal Plasma Processing* (Bristol: IOP Publ., 2001)
37. Baroch P et al. *Surf. Coat. Technol.* **193** 107 (2005)
38. Knoll M, Ruska E *Z. Phys.* **78** 318 (1932)
39. Palmer R E, Pratontep S, Boyen H G *Nature Mater.* **2** 443 (2004)
40. Binnig C, Quate C F, Gerber Ch *Phys. Rev. Lett.* **56** 930 (1986)
41. Schwartz D K et al. *Phys. Rev. E* **47** 452 (1993)
42. Paillard V et al. *Phys. Rev. Lett.* **71** 4170 (1993)
43. Butt H-J, Franz V *Phys. Rev. E* **66** 031601 (2002)
44. Loi S et al. *Phys. Rev. E* **66** 031602 (2002)
45. Rath S et al. *Phys. Rev. B* **72** 205410 (2005)
46. Jing G Y et al. *Phys. Rev. B* **73** 235409 (2006)
47. Richardson C E, Park Y-B, Atwater H A *Phys. Rev. B* **73** 245328 (2006)
48. Pakarinen O H et al. *Phys. Rev. B* **73** 235428 (2006)
49. Siegbahn K *Alpha-, Beta- and Gamma-Ray Spectroscopy* (Amsterdam: North-Holland, 1965)
50. Jergel M et al. *J. Appl. Cryst.* **30** 642 (1997)
51. de Bernabé A et al. *J. Appl. Phys.* **84** 1881 (1998)
52. Toney M F, Mate C M, Pocker D *IEEE Trans. Magn.* **34** 1774 (1998)
53. Toney M F, Mate C M, Leach K A *Appl. Phys. Lett.* **77** 3296 (2000)
54. Freitag J M, Clemens B M *J. Appl. Phys.* **89** 1101 (2001)
55. Mate C M, Toney M F, Leach K A *IEEE Trans. Magn.* **37** 1821 (2001)
56. Parratt L G *Phys. Rev.* **95** 359 (1954)
57. Bowen D K, Wormington M *Adv. X-Ray Anal.* **36** 171 (1993)
58. Lengeler B, Huppauff M, Fresenius *J. Anal. Chem.* **346** 155 (1993)
59. de Boer D K G, Leenaers A J G, van den Hoogenhof W *X-Ray Spectrom.* **24** (3) 91 (1995)
60. Pedersen J S *J. Appl. Cryst.* **25** 129 (1992)
61. Pedersen J S, Hamley I W *J. Appl. Cryst.* **27** 36 (1994)
62. Ahrens Y et al. *Phys. Rev. E* **60** 4360 (1999)
63. Golovin A L, Imamov R M, Stepanov S A *Acta Cryst. A* **40** 225 (1984)
64. Dosch H, Batterman B W, Wack D C *Phys. Rev. Lett.* **56** 1144 (1986)
65. Bernhard N et al. *Z. Phys. B* **69** 303 (1987)
66. Jach T et al. *Phys. Rev. B* **39** 5739 (1989)
67. Kondrashkina E A et al. *J. Appl. Phys.* **81** 175 (1997)
68. Marra W C, Eisenberger P, Cho A Y *J. Appl. Phys.* **50** 6927 (1979)
69. Golovin A L, Imamov R M *Phys. Status Solidi A* **80** K63 (1983)
70. Golovin A L, Imamov R M, Kondrashkina E A *Phys. Status Solidi A* **88** 505 (1985)
71. Imamov R M et al. *Poverkhnost* (3) 41 (1987)

72. Segmüller A *Thin Solid Films* **154** 33 (1987)
73. Dosch H et al. *Phys. Rev. Lett.* **60** 2382 (1988)
74. Grotehans S et al. *Phys. Rev. B* **39** 8450 (1989)
75. Williams A A et al. *Phys. Rev. B* **43** 5001 (1991)
76. Rugel S et al. *J. Appl. Cryst.* **26** 34 (1993)
77. Pietsch U et al. *J. Appl. Phys.* **74** 2381 (1993)
78. Etgens V H et al. *Phys. Rev. B* **47** 10607 (1993)
79. Stepanov S A et al. *Phys. Rev. B* **54** 8150 (1996)
80. Wulff H, Steffen H, in *Low Temperature Plasma Physics: Fundamental Aspects and Applications* (Eds R Hippler et al.) (Berlin: Wiley-VCH, 2001) p. 253
81. Demtröder W *Laser Spectroscopy: Basic Concepts and Instrumentation* 3rd ed. (Berlin: Springer-Verlag, 2003)
82. Griem H R *Plasma Spectroscopy* (New York: McGraw-Hill, 1964)
83. Svanberg S *Atomic and Molecular Spectroscopy: Basic Aspects and Practical Applications* (Springer Series on Atoms + Plasmas, Vol. 6) (Berlin: Springer-Verlag, 1991)
84. Lochte-Holtgreven W *Plasma Diagnostics* (New York: AIP Press, 1995)
85. Haverlag M et al. *J. Vac. Sci. Technol. A* **14** 380 (1996)
86. Röpcke J et al. *Plasma Chem. Plasma Process.* **19** 395 (1999)
87. Davies P B, Martineau P M *Adv. Mater.* **4** 729 (1992)
88. Haverlag M et al. *J. Vac. Sci. Technol. A* **12** 3102 (1994)
89. Naito S et al. *Jpn. J. Appl. Phys.* **34** 302 (1995)
90. Kotterer M, Conceicao J, Maier J P *Chem. Phys. Lett.* **259** 233 (1996)
91. Campargue A, Romanini D, Sadeghi N *J. Phys. D: Appl. Phys.* **31** 1168 (1998)
92. Röpcke J et al., in *Low Temperature Plasma Physics: Fundamental Aspects and Applications* (Eds R Hippler et al.) (Berlin: Wiley-VCH, 2001) p. 173
93. Langmuir I, Mott-Smith H M *Gen. Elec. Rev.* **26** 731 (1923)
94. Pfau S, Tichý M, in *Low Temperature Plasma Physics: Fundamental Aspects and Applications* (Eds R Hippler et al.) (Berlin: Wiley-VCH, 2001) p. 131
95. Straňák V et al. *Czech. J. Phys. C* **54** 826 (2004)
96. Chung P M, Talbot L, Touryan K J *Electrical Probes in Stationary and Flowing Plasmas: Theory and Application* (Applied Physics and Engineering, Vol. 11) (New York: Springer-Verlag, 1975)
97. Sanmartin J R *Phys. Fluids* **13** 103 (1970)
98. Laframboise J G, Rubinstein J *Phys. Fluids* **19** 1900 (1976)
99. Schmidt M, Foest R, Basner R, in *Low Temperature Plasma Physics: Fundamental Aspects and Applications* (Eds R Hippler et al.) (Berlin: Wiley-VCH, 2001) p. 199
100. Aikawa H *J. Phys. Soc. Jpn.* **40** 1741 (1976)
101. Passoth E et al. *J. Phys. D: Appl. Phys.* **30** 1763 (1997)
102. Kudrna P, Passoth E *Contrib. Plasma Phys.* **37** 417 (1997)
103. Brown I G et al. *Plasma Phys.* **13** 47 (1971)
104. Zakrzewski Z, Kopiczynski T, Lubanski M *Czech. J. Phys. B* **30** 1167 (1980)
105. Arslanbekov R R, Khromov N A, Kudryavtsev A A *Plasma Sources Sci. Technol.* **3** 528 (1994)
106. Behnke J F et al. *Czech. J. Phys. B* **49** 483 (1999)
107. Passoth E et al. *J. Phys. D: Appl. Phys.* **32** 2655 (1999)
108. Blauth E W *Dynamische Massenspektrometer* (Braunschweig: F. Vieweg, 1965) [Translated into English: *Dynamic Mass Spectrometers* (Amsterdam: Elsevier, 1966)]
109. Drawin H W, in *Plasma Diagnostics* (Ed. W Lochte-Holtgreven) (Amsterdam: North-Holland, 1968)
110. Schmidt M, Hinzpeter G *Beitr. Plasmaphys.* **10** 183 (1970)
111. Märk T D, Helm H *Acta Phys. Austr.* **40** 158 (1974)
112. Vasile M J, Dylla H F, in *Plasma Diagnostics* Vol. 1 (Eds O Auciello, D L Flamm) (Boston: Academic Press, 1989) p. 185
113. Scoles G (Ed.) *Atomic and Molecular Beam Methods* Vol. 1 (New York: Oxford Univ. Press, 1988) Ch. 8
114. Quadrupole mass filter — QMF 200, Oxford applied research, service instruction, version 1.1; http://www.oaresearch.co.uk/nc200data.htm
115. Samsonov D, Goree J *J. Vac. Sci. Technol. A* **17** 2835 (1999)
116. Samsonov D, Goree J *Phys. Rev. E* **59** 1047 (1999)
117. The Stopping and Range of Ions in Matter, http://www.srim.org
118. Ziegler J F, Biersack J P, Littmark U *The Stopping and Range of Ions in Solids* (New York: Pergamon Press, 1985)
119. Biersack J P, Haggmark L G *Nucl. Instrum. Methods* **174** 257 (1980)
120. Möller W, Eckstein W *Nucl. Instrum. Methods B* **2** 814 (1984)
121. Biersack J P, Eckstein W *Appl. Phys.* **34** 73 (1984)
122. Eckstein W *Computer Simulation of Ion-Solid Interactions* (Springer Series in Materials Science, Vol. 10) (Heidelberg: Springer-Verlag, 1991)
123. Thornton J A, Green J E, in *Handbook of Deposition Technologies for Films and Coatings: Science, Technology, and Applications* 2nd ed. (Ed. R F Bunshah) (Park Ridge, NJ: Noyes Publ., 1994) p. 249
124. Westwood W D *Prog. Surf. Sci.* **7** 711 (1976)
125. Feldman L C, Mayer J W *Fundamentals of Surface and Thin Film Analysis* (New York: North-Holland, 1986)
126. Stepanova M, Dew S K *J. Vac. Sci. Technol. A* **19** 2805 (2001)
127. Ekpe S D, Dew S K *J. Vac. Sci. Technol. A* **21** 476 (2003)
128. Thompson M W *Philos. Mag.* **18** 377 (1968)
129. Vidal M A, Asomoza R *J. Appl. Phys.* **67** 477 (1990)
130. Jena P et al. *Mater. Res. Soc. Symp. Proc.* **206** 3 (1991)
131. Drüsedau T P, Löhmann M, Garke B *J. Vac. Sci. Technol. A* **16** 2728 (1998)
132. Webb J B *J. Appl. Phys.* **53** 9043 (1982)
133. Emsley J *The Elements* 3rd ed. (New York: Oxford Univ. Press, 1997)
134. Leonas V B *Usp. Fiz. Nauk* **107** 29 (1972) [*Sov. Phys. Usp.* **15** 266 (1972)]
135. Smirnov B M *Usp. Fiz. Nauk* **164** 665 (1994) [*Phys. Usp.* **37** 621 (1994)]
136. Smirnov B M, Strizhev A Ju *Phys. Scripta* **49** 615 (1994)
137. Smirnov B M *Usp. Fiz. Nauk* **167** 1169 (1997) [*Phys. Usp.* **40** 1117 (1997)]
138. Egorov V S et al. *Spravochnik Konstant Elementarnykh Protsessov s Uchastiem Atomov, Ionov, Elektronov, Fotonov* (Reference Book for Elementary Processes Involving Atoms, Ions, Electrons and Photons) (Ed. A G Zhiglinskii) (St.-Petersburg: Izd. SPbGU, 1994)
139. Smirnov B M *Clusters and Small Particles: in Gases and Plasmas* (New York: Springer, 2000)
140. Kondratiev V N *Konstanty Skorosti Gazofaznykh Reaktsii* Spravochnik (Rate Constants of Gas Phase Reactions; Reference Book) (Moscow: Nauka, 1970) [Translated into English (Washington, DC: Office of Standard References Data, National Bureau of Standards, 1972)]
141. Becker A, Langel W, Knözinger E *Z. Phys. Chem.* **188** 17 (1995)
142. Smirnov B M, Shyjumon I, Hippler R *Phys. Scripta* **73** 288 (2006)
143. Smirnov B M, Shyjumon I, Hippler R *Phys. Rev. E* **75** 066402 (2007)
144. Smirnov B M *Usp. Fiz. Nauk* **170** 495 (2000) [*Phys. Usp.* **43** 453 (2000)]
145. Smirnov B M *Statistical Physics and Physical Kinetics of Atomic Systems* (Moscow: IVTRAN, 2001)
146. Smirnov B M *Usp. Fiz. Nauk* **173** 609 (2003) [*Phys. Usp.* **46** 589 (2003)]
147. Smirnov B M *Contrib. Plasma Phys.* **44** 558 (2004)
148. Landau L D, Lifshitz E M *Gidrodinamika* (Fluid Mechanics) (Moscow: Nauka, 1986) [Translated into English (Oxford: Pergamon Press, 1987)]
149. Smirnov B M *Phys. Scripta* **51** 380 (1995)
150. Vlasov M A, Zharinov A V, Kovalenko Yu A *Zh. Tekh. Fiz.* **71** (12) 34 (2001) [*Tech. Phys.* **46** 1522 (2001)]
151. Hippler R et al. *Contrib. Plasma Phys.* **45** 348 (2005)
152. Lamb H *Hydrodynamics* (New York: Dover Publ., 1945) [Translated into Russian (Moscow – Leningrad: Gostekhizdat, 1947)]
153. Landau L D, Lifshitz E M *Mekhanika* (Mechanics) (Moscow: Nauka, 1988) [Translated into English (Oxford: Pergamon Press, 1980)]
154. Wannier G H *Bell Syst. Tech. J.* **32** 170 (1953)
155. Smirnov B M *Dokl. Akad. Nauk SSSR* **168** 322 (1966) [*Sov. Phys. Dokl.* **11** 429 (1966)]
156. Smirnov B M *Fizika Slaboionizovannogo Gaza v Zadachakh s Resheniyami* (Physics of Weakly Ionized Gases) 3rd ed. (Moscow: Nauka, 1985) [Translated into English (Moscow: Mir Publ., 1981)
157. Kersten H et al. *New J. Phys.* **5** 93 (2003)
158. Smirnov B M *Phys. Scripta* **62** 111 (2000); *Usp. Fiz. Nauk* **171** 233 (2001) [*Phys. Usp.* **44** 221 (2001)]
159. Smirnov B M, in *Entsiklopediya Nizkotemperaturnoi Plazmy* (Encyclopedia of Low Temperature Plasma) Vol. VIII-1 (Eds

Yu A Lebedev, N A Plate, V E Fortov) (Moscow: Yanus-K, 2005) p. 50
160. Voloshchuk V M *Kineticheskaya Teoriya Koagulyatsii* (Kinetic Theory of Coagulation) (Leningrad: Gidrometeoizdat, 1984)
161. Rao B K, Smirnov B M *Phys. Scripta* **56** 439 (1997)
162. Rao B K, Smirnov B M *Mater. Phys. Mech.* **5** 1 (2002)
163. Morokhov I D, Trusov L I, Lapovok V N *Fizicheskie Yavleniya v Ul'tradispersnykh Sredakh* (Physical Phenomena in Ultradispersive Media) (Moscow: Energoatomizdat, 1984)
164. Krainov V P, Smirnov M B *Usp. Fiz. Nauk* **170** 969 (2000) [*Phys. Usp.* **43** 901 (2000)]
165. Krainov V P, Smirnov M B *Phys. Rep.* **370** 237 (2002)
166. Rühl E *Int. J. Mass Spectrom.* **229** 117 (2003)
167. Saalmann U, Siedschlag Ch, Rost J M *J. Phys. B: At. Mol. Opt. Phys.* **39** R39 (2006)
168. Korvink J G, Greiner A *Semiconductors for Micro- and Nanotechnology* (Weinheim: Wiley-VCH, 2002)
169. Poole Ch P, Owens F J *Introduction to Nanotechnology* (Hoboken, NJ: J. Wiley, 2003)
170. Wolf E L *Nanophysics and Nanotechnology: An Introduction to Modern Concepts in Nanoscience* (Weinheim: Wiley-VCH, 2004)
171. Köhler M, Fritzsche W *Nanotechnology: An Introduction to Nanostructuring Techniques* (Weinheim: Wiley-VCH, 2004)
172. Borisenko V E, Ossicini S *What is What in the Nanoscience* (Weinheim: Wiley-VCH, 2004)
173. Kelsall R W, Hamley I W, Geoghegan M (Eds) *Nanoscale Science and Technology* (Chichester: John Wiley, 2005)
174. Gleiter H *Nanostruct. Mater.* **1** 1 (1992)
175. Gleiter H *Nanostruct. Mater.* **6** 3 (1995)
176. Edelstein A S, Cammarata R C (Eds) *Nanomaterials: Synthesis, Properties, and Applications* (Bristol: IOP, 1996)
177. Jena P, Khanna S N *Mater. Sci. Eng. A* **217 – 218** 218 (1996)
178. Weisbuch C, Vinter B *Quantum Semiconductor Structures: Fundamentals and Applications* (Boston: Academic Press, 1991)
179. Banyai L, Koch S W *Semiconductor Quantum Dots* (Singapore: World Scientific, 1993)
180. Weisbuch C, Vinter B *The Quantum Dot* (New York: Freeman, 1995)
181. Alivisatos A P *Science* **271** 933 (1996)
182. Che M, Bennett C O *Adv. Catal.* **36** 55 (1989)
183. Henry C R *Surf. Sci. Rep.* **31** 231 (1998)
184. de Heer W A, Milani P, Châtelain A *Phys. Rev. Lett.* **65** 488 (1990)
185. Khanna S N, Linderoth S *Phys. Rev. Lett.* **67** 742 (1991)
186. Khanna S N, Jena P *Phys. Rev. Lett.* **69** 1664 (1992)
187. Weiel R *Z. Phys. D* **27** 89 (1993)
188. Takagi T *Ionized-Cluster Beam Deposition and Epitaxy* (Park Ridge, NJ: Noyes Publ., 1988)
189. Takagi T, Yamada I, Sasaki A *J. Vac. Sci. Technol.* **12** 1128 (1975)
190. Yamada I, Usui H, Takagi T *J. Phys. Chem.* **91** 2463 (1987)
191. Takagi T *J. Vac. Sci. Technol. A* **2** 382 (1984)
192. Yamada I, Inokawa H, Takagi T *J. Appl. Phys.* **56** 2746 (1984)
193. Takagi T et al. *Thin Solid Films* **126** 149 (1985)
194. Takaoka G H, Yamada I, Takagi T *J. Vac. Sci. Technol. A* **3** 2665 (1985)
195. Usui H, Yamada I, Takagi T *J. Vac. Sci. Technol. A* **4** 52 (1986)
196. Yamada I et al. *J. Vac. Sci. Technol. A* **4** 722 (1986)
197. Takagi T *Vacuum* **36** 27 (1986)
198. Takagi T *Pure Appl. Chem.* **60** 781 (1988)
199. Sosnowski M, Yamada I *Nucl. Instrum. Methods B* **46** 397 (1990)
200. Huq S E, McMahon R A, Ahmed H *Semicond. Sci. Technol.* **5** 771 (1990)
201. Takaoka G H, Ishikawa J, Takagi T *J. Vac. Sci. Technol. A* **8** 840 (1990)
202. Sosnowski M, Usui H, Yamada I *J. Vac. Sci. Technol. A* **8** 1470 (1990)
203. Hagena O F *Z. Phys. D* **20** 425 (1991)
204. Hagena O F *Rev. Sci. Instrum.* **63** 2374 (1992)
205. Gspann J *Nucl. Instrum. Methods B* **80 – 81** 1336 (1993)
206. Gspann J *Z. Phys. D* **26** S174 (1993)
207. Gspann J *Z. Phys. D* **3** 143 (1986)
208. Mélinon P et al. *Int. J. Mod. Phys. B* **9** 339 (1995)
209. Perez A et al. *J. Phys. D: Appl. Phys.* **30** 709 (1997)
210. Jensen P *Rev. Mod. Phys.* **71** 1695 (1999)
211. Pellarin M et al. *Chem. Phys. Lett.* **277** 96 (1997)
212. Mélinon P et al. *J. Chem. Phys.* **107** 10278 (1997)
213. Palpant B et al. *Phys. Rev. B* **57** 1963 (1998)
214. Ray C et al. *Phys. Rev. Lett.* **80** 5365 (1998)
215. Meiwes-Broer K-H *Metal Clusters at Surfaces: Structure, Quantum Properties, Physical Chemistry* (Berlin: Springer-Verlag, 2000)
216. Fuchs G et al. *Phys. Rev. B* **44** 3926 (1991)
217. Bréchignac C et al. *Z. Phys. D* **40** 516 (1997)
218. Bréchignac C et al. *Phys. Rev. B* **57** R2084 (1998)
219. Jensen P et al., in *Nanoclusters and Nanocrystals* (Ed. H S Nalwa) (Stevenson Ranch, Calif.: Am. Sci. Publ., 2003)
220. Witten T A (Jr.), Sander L M *Phys. Rev. Lett.* **47** 1400 (1981)
221. Meakin P *Phys. Rev. A* **27** 604 (1983)
222. Meakin P *Phys. Rev. A* **27** 1495 (1983)
223. Sahimi M et al. *Phys. Rev. A* **32** 590 (1985)
224. Jensen P et al. *Phys. Rev. B* **50** 15316 (1994)
225. Jullien R, Botet R *Aggregation and Fractal Aggregates* (Singapore: World Scientific, 1987)
226. Vicsek T *Fractal Growth Phenomena* (Singapore: World Scientific, 1989)
227. Smirnov B M *Phys. Rep.* **188** 1 (1990); *Fizika Fraktal'nykh Klasterov* (Physics of Fractal Clusters) (Moscow: Nauka, 1991)
228. Elam W T et al. *Phys. Rev. Lett.* **54** 701 (1985)
229. Sawada Y, Dougherty A, Golub J P *Phys. Rev. Lett.* **56** 1260 (1986)
230. Grier D et al. *Phys. Rev. Lett.* **56** 1264 (1986)
231. Montano P A et al. *Phys. Rev. B* **30** 672 (1984)
232. Sattler K, in *Handbook of Thin Film Materials* Vol. 5 (Ed. H S Nalwa) (San Diego: Academic Press, 2002) Ch. 2
233. Zuo J M, Li B Q *Phys. Rev. Lett.* **88** 255502 (2002)
234. Zhang F et al. *Appl. Phys. Lett.* **80** 127 (2002)
235. Shyjumon I et al. *Eur. Phys. J. D* **37** 409 (2006)
236. Chu J H, Lin I *Phys. Rev. Lett.* **72** 4009 (1994)
237. Thomas H et al. *Phys. Rev. Lett.* **73** 652 (1994)
238. Hayashi Y, Tachibana K *Jpn. J. Appl. Phys.* **33** L804 (1994)
239. Melzer A, Trottenberg T, Piel A *Phys. Lett. A* **191** 301 (1994)
240. Morfill G E et al. *Phys. Plasmas* **6** 1769 (1999)
241. Trottenberg T, Melzer A, Piel A *Plasma Sources Sci. Technol.* **4** 450 (1995)
242. Morfill G E, Thomas H *J. Vac. Sci. Technol. A* **14** 490 (1996)
243. Nefedov A P, Petrov O F, Fortov V E *Usp. Fiz. Nauk* **167** 1215 (1997) [*Phys. Usp.* **40** 1163 (1997)]
244. Shukla P K, Mamun A A *Introduction to Dusty Plasma Physics* (Bristol: IOP Publ., 2002)
245. Fortov V E et al. *Usp. Fiz. Nauk* **174** 495 (2004) [*Phys. Usp.* **47** 447 (2004)]
246. Fortov V E, Khrapak A G, Yakubov I T *Fizika Neideal'noi Plazmy* (Physics of Non-Ideal Plasma) (Moscow: Fizmatlit, 2004)
247. Fortov V E et al. *Pis'ma Zh. Eksp. Teor. Fiz.* **63** 176 (1996) [*JETP Lett.* **63** 187 (1996)]
248. Fortov V E et al. *Pis'ma Zh. Eksp. Teor. Fiz.* **64** 86 (1996) [*JETP Lett.* **64** 92 (1996)]
249. Kersten H, Schmetz P, Kroesen G M W *Surf. Coat. Tech.* **108 – 109** 507 (1998)
250. Thieme G et al., in *Proc. of the 26th Intern. Conf. on Phenomena in Ionized Gases, Greiswald, Germany, 2003* Vol. 1 (Eds J Meichsner, D Loffhagen, H E Wagner) (Greiswald, 2003) p. 251
251. Hagena O F, Knop G, Ries R *KFK Nachr.* **23** 136 (1991)
252. Hagena O F *Rev. Sci. Instrum.* **63** 2374 (1992)
253. Hagena O F, Knop G, Linker G, in *Physics and Chemistry of Finite Systems: From Clusters to Crystals* Vol. 2 (NATO ASI Series, Ser. C, No. 374, Eds P Jena, S N Khanna, B K Rao) (Dordrecht: Kluwer Acad. Publ., 1992) p. 1233
254. Hagena O F et al. *J. Vac. Sci. Technol. A* **12** 282 (1994)